

Max Gerhards

vom Fachbereich VI  
Raum- und Umweltwissenschaften  
der Universität Trier  
zur Verleihung des akademischen Grades  
Doktor der Naturwissenschaften (Dr. rer. nat.)  
genehmigte Dissertation

# **Advanced Thermal Remote Sensing for Water Stress Detection of Agricultural Crops**

Betreuender:

Univ.-Prof. Dr. Thomas Udelhoven

Berichterstattende:

Univ.-Prof. Dr. Thomas Udelhoven

Univ.-Prof. Dr.-Ing. Markus Casper

Dr. Martin Schlerf

Datum der wissenschaftlichen Aussprache:

08.02.2018

Trier, 2018



## Acknowledgments

Five years ago, I would never have imagined writing this very last part of my Ph.D. thesis. At this time, I was finalizing my Diploma thesis. After one year of troubleshooting and rarely first successes with the “hyperthermal” machine, I was sure to do not continue with Thermal Infrared Remote Sensing. And now...

I would like to greatly thank all the magnificent people accompanying me during the last four years for their help, support and encouragement in all the different situations of life.

First of all, I particularly would like to thank my supervisors: Prof. Dr. Thomas Udelhoven and Dr. Martin Schlerf. I would have never started this work without knowing you as an excellent supervision team. Thomas, I greatly thank you for your scientific support and input, for always giving me the freedom to follow my ideas and the confidence to implement these ideas into my research. Martin, I am deeply grateful to you for pushing my scientific and personal skills. Besides teaching me how to do science and to write excellent scientific manuscripts, I thank you for your open-minded attitude and your high degree of human sensitivity – thank you for always showing me prospects. It was a pleasure for me to be supervised by you!

Furthermore, I would like to express my gratitude to Prof. Dr.-Ing. Markus Casper for examining this dissertation.

My particular thanks go to Dr. Gilles Rock. Thank you for: sharing the time of the Ph.D. journey starting from the unboxing of the *Hyper-Cam LW*, several trips to ITC, Latisana, and elsewhere, designing and concluding experiments, data processing, and fruitful discussions. Thank you for being a constant companion during my TIR times and for being a good friend apart from the academic world.

A special thank goes to my team mates at LIST: Miriam Machwitz, Franz Kai Ronellenfitsch, and Kaniska Mallick. Thank you guys for your support during campaigns, fruitful discussion and for making the everyday life enjoyable!

Kim Fischer, thank you for your support during experiments and data processing. I wish you all the best for your future career and I am looking forward working with you again.

As a “rule of fist”, a Ph.D. thesis requires a lot of chocolate and fellow sufferers. Thank you Anne Schneibel for the never-ending supply of Lindt chocolate and thank you Sandra Dotzler for the mindless, funny discussions. I would also like to thank the team of the “Environmental Remote Sensing & Geoinformatics” department at University of Trier for always warmly welcoming me during my stays and offering a friendly, open working atmosphere. I was always felt to be part of your team without sharing any projects.

A further thank goes to my Ph.D. mates from LIST. Thank you Dario, Mahmood, Hanna, Annelie, Anna, Arturo, Barbara, Marta and all the others I forgot. I wish you all the best for your ongoing Ph.D. theses and/or your future career and hope we will meet some day again!

Thank you Dr. Michele Weber for proofreading the manuscript and for your encouragement to finish my thesis.

I would like to thank the Fonds National de la Recherche (FNR) of Luxembourg for funding the PLANTSENS research project [‘Detection of plant stress using advanced thermal and spectral remote sensing techniques for improved crop management’; AFR reference: C13/SR/5894876]

Life does not only consist of work, thankfully. To my friends for the good times we had and we will have. Thank you Matthias, Christian, Franz, Daniel, Martin, Helena, Tim, Susanne, Buddy & Leni, Sarah, Benni & Johann, and all the others I forgot!

My exceptional gratitude belongs to my parents Monika and Uwe for the never-ending support. Thank you for always being there for me!

Sandra, I thank you for being my best friend, my lover and my partner. Without your selfless support, I would not be where I am today.



## Summary

Water is essential for the growth of plants, their metabolic processes, and their general health. Water-deficit stress, usually shortened to water- or drought stress, is one of the most critical abiotic stressors limiting plant growth, crop yield and quality concerning food production. Today, agriculture consumes about 80 – 90 % of the global freshwater used by humans and about two thirds are used for crop irrigation. An increasing world population and a predicted rise of 1.0 – 2.5°C in the annual mean global temperature as a result of climate change will further increase the demand of water in agriculture. Therefore, one of the most challenging tasks of our generation is to reduce the amount water used per unit yield to satisfy the second UN Sustainable Development Goal and to ensure global food security. Precision agriculture offers new farming methods with the goal to improve the efficiency of crop production by a sustainable use of resources.

Plant responses to water stress are complex and co-occur with other environmental stresses under natural conditions. In general, water stress causes plant physiological and biochemical changes that depend on the severity and the duration of the actual plant water deficit. Stomatal closure is one of the first responses to plant water stress causing a decrease in plant transpiration and thus an increase in plant temperature. Prolonged or severe water stress leads to irreversible damage to the photosynthetic machinery and is associated with decreasing chlorophyll content and leaf structural changes (*e.g.*, leaf rolling). Since a crop can already be irreversibly damaged by only mild water deficit, a pre-visual detection of water stress symptoms is essential to avoid yield loss.

Remote sensing offers a non-destructive and spatio-temporal method for measuring numerous physiological, biochemical and structural crop characteristics at different scales and thus, is one of the key technologies used in precision agriculture. With respect to the detection of plant responses to water stress, the current state-of-the-art hyperspectral remote sensing imaging techniques are based on measurements of thermal infrared emission (TIR; 8 – 14  $\mu\text{m}$ ), visible, near- and shortwave infrared reflectance (VNIR/SWIR; 0.4 – 2.5  $\mu\text{m}$ ), and sun-induced fluorescence (SIF; 0.69 and 0.76  $\mu\text{m}$ ). It is, however, still unclear how sensitive are these techniques with respect to water stress detection.

Therefore, the overall aim of this dissertation was to provide a comparative assessment of remotely sensed measures from the TIR, SIF, and VNIR/SWIR domains for their ability to detect plant responses to water stress at ground- and airborne level. In particular, the objectives of the thesis were to: (i) assess the ability of hyperspectral remote sensing indices (including spectral emissivity, CWSI, PRI, SIF) to detect water stress, (ii) examine the potential of hyperspectral remote sensing indices for water stress detection at airborne level and provide an outlook for future satellite missions, (iii) determine the advantages of hyperspectral TIR instruments in comparison to broadband TIR instruments for the retrieval

of temperature and emissivity, (iv) assess the effect of other factors than stress (*i.e.*, plant species) on spectral emissivity. The research objectives were examined in four experimental studies and are the subject of four peer-reviewed publications.

The main finding of this thesis is that temperature-based indices (*e.g.*, CWSI) were most sensitive for the detection of plant water stress in comparison to reflectance-based VNIR/SWIR indices (*e.g.*, PRI) and SIF, at both ground- and airborne level. Further findings are, first, that even mild effects on plant transpiration could be measured at airborne level using temperature-based indices retrieved by high spatial resolution TIR images. Second, for the first time, spectral emissivity as measured by the new hyperspectral TIR imaging instrument could be used to detect plant water stress at ground level. Third, temperature-based indices were equally sensitive for the detection of plant responses to water stress as retrieved from hyperspectral or broadband TIR images. Finally, different plant species revealed distinct spectral emissivity features in the TIR spectral domain.

Based on these findings it can be stated that hyperspectral TIR remote sensing offers great potential for the detection of plant responses to water stress at ground- and airborne level based on both TIR key variables, surface temperature and spectral emissivity. However, the large-scale application of water stress detection based on hyperspectral TIR measures in precision agriculture will be challenged by several problems: (i) missing thresholds of temperature-based indices (*e.g.*, CWSI) for the application in irrigation scheduling, (ii) profound knowledge about the relationship between the spectral emissivity features and changes in leaf traits under environmental stress conditions is missing, (iii) lack of current TIR satellite missions with suitable spectral and spatial resolution, (iv) lack of appropriate data processing schemes (including atmosphere correction and temperature emissivity separation) for hyperspectral TIR remote sensing at airborne- and satellite level.





## Contents

Acknowledgments.....	i
Summary .....	iv
Contents .....	vii
List of Figures .....	ix
List of Tables .....	xii
List of Abbreviations .....	xiv
<b>Chapter I.....</b>	<b>1</b>
Introduction	
1. Importance of Water Stress Detection .....	2
2. Plant Responses to Water Stress .....	3
3. Remote Sensing of Water Stress .....	5
3.1. Thermal Infrared Domain .....	5
3.1.1. Temperature Approach .....	5
3.1.2. Emissivity Approach .....	8
3.1.3. Hyperspectral TIR Image Pre-Processing.....	9
3.2. Solar-Reflective Domain .....	10
3.3. Sun-Induced Fluorescence (SIF) .....	12
3.4. Multi-Sensor Approach .....	13
4. Objectives.....	14
5. Overview and Structure of the Thesis.....	15
<b>Chapter II.....</b>	<b>19</b>
A Hyperspectral Thermal Infrared Imaging Instrument for Natural Resources Applications	
<b>Chapter III.....</b>	<b>36</b>
Water Stress Detection in Potato Plants using Leaf Temperature, Emissivity, and Reflectance	

<b>Chapter IV .....</b>	<b>61</b>
A Comparative Analysis for Remote Sensing of Plant Water Stress Symptoms Based on Airborne Optical and Thermal Hyperspectral Images	
<b>Chapter V .....</b>	<b>89</b>
Plant Species Discrimination using Emissive Thermal Infrared Imaging Spectroscopy	
<b>Chapter VI.....</b>	<b>111</b>
Synthesis	
1. Main Findings .....	112
2. Conclusion & Outlook .....	116
References.....	120
Curriculum Vitae .....	139

## List of Figures

Fig. I-1: Most important relationships between primary plant stresses, the induced plant responses, and the hyperspectral remote sensing techniques for the detection of environmental stresses (modified after Jones and Vaughan, 2010, p. 272).....	4
Fig. II-1: <i>Hyper-Cam LW</i> Sensor (left) and instrument setup for ground measurements (right).....	24
Fig. II-2: <i>Hyper-Cam LW</i> airborne assembly (top) and acquisition scheme (bottom): The IMC system is servo controlled to ensure the sensor is staring at a fixed scene during the acquisition of the hyperspectral image.....	25
Fig. II-3: Measurement sequence of sample (sandstone), cold blackbody, hot blackbody and downwelling radiation and the derived sample emissivity spectrum. The lines shown represent the mean of 56 single measurements. ....	27
Fig. II-4: Demonstration of repeatability: The red line is an average of 56 single measurements and the grey band indicates the 99.9 % confidence interval of the mean at each wavenumber.....	30
Fig. II-5: Emissivity spectra of the Bunter Sandstone sample derived from the <i>Hyper-Cam LW</i> (red) and from the Bruker (blue).....	31
Fig. II-6: Emissivity spectra of Calcite (top), and Quartz (bottom) derived from <i>Hyper-Cam LW</i> and Bruker spectrometers.....	32
Fig. II-7: Surface of the sandstone sample (top) and derived emissivity values at 1,095 cm <sup>-1</sup> (bottom). White pixels are detector failures which are marked as bad pixels by the Reveal Pro software. ....	33
Fig. III-1: Experimental setup with <i>Hyper-Cam LW</i> on the tripod, Fluke TiR1, Lci leaf porometer, Infragold as well as dry and wet references targets (a), plant breeding and storage of the 60 potato plants under a roof construction (b), plants of the control (c) and treatment (d) group at day 9 after stress initiation.....	44
Fig. III-2: Potato yield of stressed (treatment) and non-stressed (control) plants (left), boxplots and mean values per group as well as corresponding p-value of a t-test (right).....	48
Fig. III-3: Boxplots per day after stress initiation of the meteorological (air temperature, VPD, rel. humidity) and plant physiological measurements (stomatal conductance, transpiration and photosynthetic rate). Asterisks (*) indicating significant differences between control and treatment group at 5 % significance level. ....	49

- Fig. III-4: Correlogram of spearman correlation of observed variables. Relationships which are not significant at 5 % significance level are marked by crosses. Main correlation clusters occur within meteorological variables, comparing the three retrieval approaches of temperature based indices (e.g., CWSI) as well as water content based indices (e.g., WI and MSI). Furthermore, strong individual correlation can be observed, e.g. between  $T_{\text{leaf}}$  and meteorological variables..... 50
- Fig. III-5: Example of visual images (left) and corresponding temperature maps (right) taken with Fluke thermal imager at first and last day of the experiment. At the overlaid temperature maps Infragold reflecting the cold sky (blue coloured) at the bottom image edges can be registered as well as obvious temperature differences between the wet (yellowish green coloured with approx. 295 K) and dry reference targets (red coloured with approx. 310 K). Aluminium sheet was used to reduce the DWR from neighbouring objects. .... 51
- Fig. III-6: Boxplots per day after stress initiation of leaf temperatures ( $T_{\text{mean}}$ ),  $T_{\text{leaf}} - T_{\text{air}}$  and CWSI of the three temperature retrieval approaches (*Hyper-Cam LW* (HC), *Hyper-Cam LW* broadband (HC broadband), Fluke). Asterisks (\*) indicating significant difference between control and treatment group at 5 % significance level. .... 54
- Fig. III-7: Boxplots per day after stress initiation of vegetation indices at leaf scale. Asterisks (\*) indicating significant difference between control and treatment group at 5 % significance level. .... 55
- Fig. III-8: Mean emissivity spectra of potato plants (*Solanum tuberosum L. Cilena*) per day after stress initiation for control (black) and treatment (red) group. Corresponding  $p$ -values of a Mann-Whitney-U-tests at 5 % level of significance per wavenumber are grouped by significance (right-handed and marked with asterisks..... 57
- Fig. IV-1: Overview of the study site with the experimental setup. The study site was located in north eastern Italy near the town of Latisana (a.). (b.) shows the locations of the experimental plots, pool and weather station. A scheme of the experimental design is presented in the legend. .... 67
- Fig. IV-2: Environmental conditions (net radiation ( $R_n$ ), air temperature ( $T_{\text{air}}$ ), surface temperature ( $T_s$ ),  $T_s - T_{\text{air}}$ , vapour pressure deficit (VPD), as well as soil water content (SWC)) for 11<sup>th</sup> and 12<sup>th</sup> of June 2014 over a non-treated grass surface measured by the weather station. .... 73

Fig. IV-3: Diurnal changes in chamber flux measurements for CR (green) and VG (orange) treatments. Solid lines are showing H<sub>2</sub>O fluxes in mmols H<sub>2</sub>O m<sup>-2</sup> s<sup>-1</sup> and GEP is represented in dashed lines measured in μmols CO<sub>2</sub> m<sup>-2</sup> s<sup>-1</sup> (upper left). PAR as measured in μmols m<sup>-2</sup> s<sup>-1</sup> is represented with dotted lines (upper right). Boxplots for H<sub>2</sub>O fluxes (lower left) and H<sub>2</sub>O fluxes normalized by PAR (lower right). ..... 75

Fig. IV-4: Diurnal T<sub>s</sub> [K] and CWSI maps at 11<sup>th</sup> June (top), F<sub>687</sub>, F<sub>760</sub>, PRI, NDVI and LWI maps of the same day (11<sup>th</sup> June, 14:52 CEST) (bottom left), and locations of the treatments (bottom right). ..... 77

Fig. IV-5: Boxplots of the different treatments (CR, KA, VG) at the three overpasses for T<sub>s</sub>, T<sub>s</sub> - T<sub>air</sub> and CWSI. Different letters indicate significant differences (\*p ≤ 0.05). ..... 78

Fig. IV-6: VNIR/SWIR mean reflectance spectra from HyPlant's dual-channel module. .... 79

Fig. IV-7: Boxplots of the different treatments (CR, KA, and VG) at three HyPlant overpasses for VNIR/SWIR based indices and F<sub>687</sub> and F<sub>760</sub>. Different letters indicate significant differences (\*p ≤ 0.05). ..... 79

Fig. V-1: VSWIR spectra for the investigated species. Black: Mean spectra (N = 35), grey: mean +/- 1 standard deviation. .... 99

Fig. V-2: Comparison of Hyper-Cam LW spectra (black line: average of 100 randomly selected pixel, grey: mean +/- 1 sd) with Bruker reference spectra (red line). .... 100

Fig. V-3: Comparison of vector normalized Hyper-Cam LW spectra (grey and black) and Bruker reference spectra (red). .... 101

Fig. V-4: Classification result from native spatial resolution (top), 3 x 3 spatial averaging (middle) and 5 x 5 spatial averaging (bottom). Colour: species, grey: background, black: pixel with non-converging TES. The 5 leaves from one column originate from one plant. The leaves from Ap being much larger than the remaining, it seems that a lot of background pixel were misclassified, which is not the case. .... 104

Fig. V-5: Relative importance of spectral band for RFC (left) and OAA of RFC by increasing number of spectral bands (right). .... 105

## List of Tables

Table II-1: <i>Hyper-Cam LW</i> specifications; NESR = noise equivalent spectral radiance.....	24
Table III-1: Number of observations per day after stress initiation. ....	41
Table III-2: Optical (VNIR/SWIR) narrow-band indices grouped by category: (1) xanthophyll pigments, (2) water content and (3) greenness. R is the reflectance at the ASD Fieldspec 3 wavelength in nm.....	47
Table III-3: p-values (level of statistical significance: *** $p < 0.001$ , ** $p < 0.01$ , * $p < 0.05$ ) of Mann-Whitney-U-test per day after stress initiation. ....	53
Table IV-1: Assumed effects of treatments on spectral domains. ....	66
Table IV-2: Optical (VNIR/SWIR) narrow-band indices grouped by category: (1) xanthophyll pigments, (2) greenness and (3) water content. R is the reflectance center wavelength of <i>HyPlant</i> Dual Chanel in nm.....	71
Table IV-3: Ground ( $T_{ground}$ ) and airborne ( $T_{airborne}$ ) temperatures of a water filled pool and their differences ( $\Delta T$ ) per TIR airborne overpass.....	76
Table IV-4: Observed effects of treatments on spectral domains. ....	844
Table IV-A1: Descriptive statistics: mean ( $\bar{x}$ ) and standard deviation ( $sd$ ) for every index per flight and treatment (Control (CR), Kaolin (KA) and Vapor Gard (VG)).....	86
Table IV-A2: p-values (level of statistical significance: *** $p < 0.001$ , ** $p < 0.01$ , * $p < 0.05$ ) of Tukey's HSD pairwise comparison and mean differences of treatments (CR, KA, VG) for temperature-based indices at all three <i>Hyper-Cam LW</i> overpasses.....	86
Table IV-A3: p-values (level of statistical significance: *** $p < 0.001$ , ** $p < 0.01$ , * $p < 0.05$ ) of Tukey's HSD pairwise comparison and mean differences of treatments (CR, KA, VG) for VNIR/SWIR based indices and $F_{687}$ and $F_{760}$ at three <i>HyPlant</i> overpasses.....	87
Table V-1: The studied plant species with their common name, Latin name, sample size and short code. ....	92
Table V-2: Nash-Sutcliffe-Efficiency Index (NSE) and Pearson's correlation coefficient ( $r$ ) for the different species measured with the <i>Hyper-Cam LW</i> and Bruker Vertex 70.....	101

Table V-3: Classification results (mode +/- 1 sd of 20 classification runs) for the two spectral domains.  
..... 102

Table V-4: Representative error matrix for a single classification run based on TIR spectroscopy data.  
..... 102

Table V-5: Representative error matrix for a single classification run based on VSWIR spectroscopy  
data..... 102

Table V-6: Error matrix from classification result based on native spatial resolution image data. .... 102

Table V-7: Error matrix from classification result based on spatial averaged (3x3) image data. .... 103

Table V-8: Error matrix from classification result based on spatially averaged (5x5) image data. .... 103

## List of Abbreviations

AAC	Autonomous Atmospheric Compensation	ECOSTRESS	Ecosystem Spaceborne Thermal Radiometer
ABA	ABscisic Acid		Experiment on Space Station
AHI	Airborne Hyperspectral Imager	ESA	European Space Agency
AHS	Airborne Hyperspectral Scanner	<i>f</i> APAR	Fraction of APAR
APAR	Absorbed Photosynthetic Active Radiation	FLD	Fraunhofer Line Depth
ARTEMIS	Automatic Retrieval of Temperature and Emissivity using Spectral Smoothness	FLEX	Fluorescence Explorer
ASTER	Advanced Spaceborne Thermal Emission and Reflection Radiometer	FNR	Fonds National de la Recherche
ATLAS	Airborne Thermal and Land Applications Sensor	FOV	Field-Of-View
AVHRR	Advanced Very High Resolution Radiometer	FPA	Focal Plane Array
AVIRIS	Airborne Visible/Infrared Imaging Spectrometer	FTIR	Fourier Transform Infrared
BB	Blackbody	FWHM	Full Width at Half Maximum
CEST	Central Europe Solar Time	GEDI	Global Ecosystem Dynamics Investigation
CWSI	Crop Water Stress Index	GEP	Gross Ecosystem Productivity
DFG	Deutsche Forschungsgemeinschaft	GSD	Ground Sampling Distance
DFT	Discrete-Fourier Transform	HISUI	Hyperspectral Imager Suite
DHR	Directional-Hemispherical Reflectance	HiTeSEM	High-resolution Temperature and Spectral Emissivity Mapping
DPPN	German Plant Phenotyping Network	HysPIRI	Hyperspectral Infrared Imager
DRRI	Downwelling Radiance Residual Index	IMC	Image Motion Compensator
DWR	Down-Welling Radiance	INS	Inertial Navigation System
		IPCC	Intergovernmental Panel on Climate Change
		ISAC	In Scene Atmospheric Compensation
		ISS	International Space Station
		ITC	University of Twente
		LAI	Leaf Area Index
		LDCM	Landsat Data Continuity Mission
		LIDAR	Light Detection And Ranging



LST	Land Surface Temperature	RH	Relative Humidity
LUT	Look Up Table	ROI	Region of Interest
LWI	Leaf Water Index	SDD	Stress Degree Day
MCT	Mercury Cadmium Telluride	SEBASS	Spatially Enhanced Broadband Array Spectrograph System
MDA	Mean Decrease in Accuracy	SIF	Sun-Induced Fluorescence
MODIS	Moderate Resolution Imaging Spectroradiometer	SNR	Signal-to-Noise-Ratio
MODTRAN	MODerate resolution atmospheric TRANsmission	SPOT	Système Probatoire d'Observation de la Terre
MSI	Moisture Stress Index	SR	Simple Ratio
MWIR	Midwave Infrared	STIC	Surface Temperature Initiated Closure
NDVI	Normalized Difference Vegetation Index	SWC	Soil Water Content
NDWI	Normalized Difference Water Index	SWIR	Shortwave Infrared
NEE	Net Ecosystem Exchange	TES	Temperature Emissivity Separation
NESR	Noise Equivalent Spectral Radiance	TIMS	Thermal Infrared Multispectral Scanner
NIR	Near Infrared	TIR	Thermal Infrared
NSE	Nash-Sutcliff-Efficiency index	UN	United Nations
OCO-3	Orbiting Carbon Observatory	VG	Vapor Gard
PAR	Photosynthetic Active Radiation	VI	Vegetation Index
PCA	Principal Component Analysis	VIS	Visual
PRI	Photochemical Reflectance Index	VNIR/SWIR	Visible, Near- and Shortwave Infrared
RDVI	Renormalized Difference Vegetation Index	VPD	Vapour Pressure Deficit
RFC	Random-Forest Classifier	VSWIR	Visible to Shortwave Infrared
		WDI	Water Deficit Index
		WI	Water Index



# **Chapter I**

## **Introduction**

## 1 Importance of Water Stress Detection

Water-deficit stress, usually shortened to water- or drought stress, describes the plant physiological responses induced by lack of available water due to either soil water deficit or high evaporative demand of the atmosphere. Water stress induces dehydration in the plant and prevents plant cells to keep water concentrations at an acceptable and healthy level (Hopkins and Hüner, 2009; Porporato and Laio, 2001). Therefore, water stress is one of the most critical abiotic stressors limiting plant growth, crop yield and quality concerning food production (Chaves *et al.*, 2002; Hsiao *et al.*, 1976).

Since the global population is projected to grow by about 2.3 billion people between 2015 and 2050 and societies are changing from low to medium per capita income, global food demand is expected to double within the same time (Atzberger, 2013; Tilman *et al.*, 2011; United Nations, 2015a). Therefore, one of the most challenging tasks of our generation is to meet the second Sustainable Development Goal as defined in the 2030 agenda for sustainable development by the United Nations: ‘*End hunger, achieve food security and improved nutrition and promote sustainable agriculture.*’ (United Nations, 2015b). In this respect, agricultural processes need to be optimized and innovative farming methods must be developed to guarantee global food supply, as arable land and environmental resources have almost reached the limits of sustainability.

Water is the most valuable resource of our planet. Today, agriculture consumes 80 – 90 % of freshwater used by humans worldwide and about two-thirds of this freshwater is required for crop irrigation (Fereser and Evans, 2006). In the words of Kofi Annan, former UN Secretary General, in 2000: ‘*we need a Blue Revolution in agriculture that focuses on increasing productivity per unit of water*’. The ultimate goal must be a reduction of the amount of water used per unit yield (Morison *et al.*, 2008).

In addition, anthropogenic climate change is predicted to cause an increase of 1.0 – 2.5°C in the annual mean global temperature over the next 50 years with tremendous impact on agriculture (IPCC, 2007). As a consequence, evapotranspiration rates will increase and thus, the demand of water for crop irrigation will further rise. At the same time, extreme weather events such as droughts will appear more frequently and be more severe. These facts add some extra pressure to an increasing global water scarcity and the need for saving water.

Hence, it is desired to reduce the amount of water used per unit yield by reducing yield loss and by reducing the amount of water used for irrigation. To achieve this goal, early detection and monitoring of plant responses to water stress in agricultural crops are mandatory. Remote sensing offers the opportunity to acquire high spatial, spectral and temporal resolution data as input for precision agriculture (Gebbers and Adamchuk, 2010). Precision agriculture promises great potential to close the yield gap by optimising food production using the right management practice at the right place and the right time, while keeping the consumption of resources at an environmentally sustainable level (Mulla, 2013).

## 2 Plant Responses to Water Stress

Plant responses to water stress are numerous and complex (see Chaves *et al.*, 2002; Hsiao, 1973; Mahajan and Tuteja, 2005; Yordanov *et al.*, 2003 for comprehensive reviews). They appear synergistically or antagonistically and are modified by co-occurring plant stresses under field conditions (Fig. I-1) (Chaves *et al.*, 2002; Jones and Schofield, 2008; Schulze, 1986). Therefore, it remains difficult to detect and monitor plant water deficit based on a single plant response (Jones and Vaughan, 2010). In general, water deficit causes physiological and biochemical changes which induce a reduction in photosynthesis and thus plant growth (Yordanov *et al.*, 2003). However, the timing, intensity and duration of water stress are crucial to determine the plant physiological responses and their impact on plant metabolism (Chaves and Oliveira, 2004). For example, under mild water stress conditions, plant regulation of water loss and uptake still allows the plant to maintain relative leaf water content with no or only little change in photosynthetic capacity. In contrast, severe water deficit induces serious physiological and biochemical changes, which lead to effects ranging from inhibition of photosynthesis and growth to leaf wilting and the loss of key pigments like chlorophyll and thus to irreversible damage to the photosynthetic machinery (Jones and Schofield, 2008; Mahajan and Tuteja, 2005; Yordanov *et al.*, 2003). Hence, plants have developed multiple mechanisms to prevent severe damage through water stress (Bray, 1997).

The first plant response to water stress is stomatal closure, which prevents transpirational water loss (*e.g.*, Chaves *et al.*, 2002; Jones and Schofield, 2008; Mahajan and Tuteja, 2005). In particular, stomatal closure is the response to either a deficit in soil water supply or to low-humidity atmosphere with a high evaporative demand. It is commonly assumed that stomatal response is rather linked to soil water content than to leaf water content. This suggests that stomata are most likely triggered by chemical signals, such as the accumulation of abscisic acid (ABA) in dehydrated roots rather than by a reduced cell turgor (Chaves *et al.*, 2002). However, under severe and/or prolonged water stress, cell turgor and leaf water content is also reduced (Mahajan and Tuteja, 2005). As a consequence, the exchange of water vapor between plants and atmosphere is reduced by stomatal closure and thus, the evaporative cooling effect is decreased resulting in an overall increase of plant temperature compared to a plant which does not suffer from water stress (Hsiao, 1973; Jones, 2004a; Schulze, 1986).

However, the stomata not only control plant transpiration but also plant respiration which inhibits CO<sub>2</sub> uptake and fixation. As a result of stomatal closure, the photosynthetic rate is reduced, which causes a reduction in cell division and thus slows down leaf growth and decreases leaf surface area. A persistent water deficit will further damage the photosynthetic machinery through loss of chlorophyll, which finally introduces changes in leaf colour and wilting (Chaves and Oliveira, 2004; Mahajan and Tuteja, 2005; Yordanov *et al.*, 2003). Another plant response to water stress is the change in sun-induced fluorescence (SIF). While the photosynthetic rate is reduced by a decreased CO<sub>2</sub> uptake due to

stomatal closure, irradiance and absorbed photosynthetically active radiation ( $fAPAR$ ) remain constant. In general, energy absorbed by plant pigments (*i.e.*, the chlorophylls and carotenoids) is dissipated by three competitive processes (*i.e.*, photosynthesis, SIF and heat emission). Consequently, a reduction of photosynthesis implies an increase in SIF and/or heat dissipation (Porcar-Castell *et al.*, 2014).

Besides these plant responses to water stress, osmotic adjustment is a further strategy to prevent irreversible damage. Osmotic adjustment describes the process of the accumulation of solutes such as carbohydrates and proteins to maintain the cell turgor at osmotic equilibrium (Bradford and Hsiao, 1982).

In summary, plant responses to water stress can be recognized as a sequence of physiological and biochemical changes depending on the severity and duration of plant water deficit. Hence, the detection of water stress symptoms is a function of time and depends on the plant responses to water deficit and their corresponding physiological changes, which may be sensitive to different remote sensing techniques.

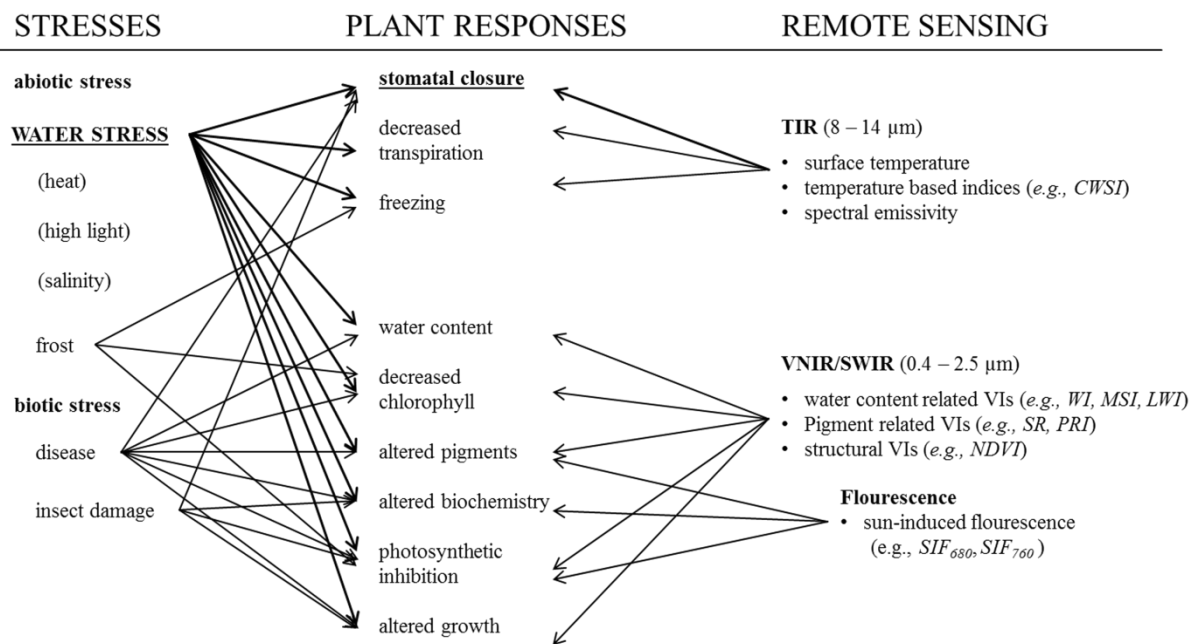


Fig. I-1: Most important relationships between primary plant stresses, the induced plant responses, and the hyperspectral remote sensing techniques for the detection of environmental stresses (modified after Jones and Vaughan, 2010, p. 272).

### 3 Remote Sensing of Water Stress

Remote sensing is one of the key technologies in precision agriculture, which has an enormous demand for geospatial information (Gebbers and Adamchuk, 2010; Mulla, 2013). Besides the information needs for soil properties, crop nutrients, crop biomass and diseases, farmers and decision makers have a major interest in the detection of plant responses to environmental stresses for (Lee *et al.*, 2010). In general, remote sensing provides a fast, cost-efficient, non-destructive and spatio-temporal measure of numerous physiological, biochemical and structural crop characteristics at different scales (ground, airborne, and satellite). Since the plant can already be irreversibly affected once visible symptoms of water stress appear, a pre-symptomatic or pre-visual detection of plant physiological changes can contribute essentially to avoid severe crop damage (Chaerle and Van Der Straeten, 2000). Especially hyperspectral imagery, with its continuous spectral data, has the potential to provide further insights into the relationship between spectral features and associated plant conditions (Pinter Jr. *et al.*, 2003). Focusing on the detection of plant responses to environmental stresses, the main hyperspectral remote sensing techniques are thermal imaging (TIR; 8 – 14  $\mu\text{m}$ ), visible, near- and shortwave infrared reflectance (VNIR/SWIR; 0.4 – 2.5  $\mu\text{m}$ ), and sun-induced fluorescence (SIF; 0.69 and 0.76  $\mu\text{m}$ ).

#### 3.1 Thermal Infrared Domain

Since the 1970's thermal remote sensing (8 – 14  $\mu\text{m}$ ) has been recognized as a potential tool for early plant water stress detection. In general, emitted radiance in the TIR contains two kinds of information: (i) surface temperature of the object of interest and (ii) its spectral emissivity.

##### 3.1.1 Temperature Approach

Measuring leaf or canopy temperature for the detection of plant responses to water deficit stress is based on the idea of Tanner (1963). It is well established from the leaf energy balance equation that leaf temperature varies with (evapo-) transpiration rates of the leaves and hence is a function of stomatal conductance (Fuchs and Tanner, 1966; Jones, 1999a; Tanner, 1963). The transpiration rate is inversely correlated to leaf temperature (Inoue *et al.*, 1990). The underlying principle is that if plant water status decreases, leaf transpiration is reduced as a result of active regulation of stomatal aperture (Chaerle and Van Der Straeten, 2000). Consequently, the inhibited evaporative cooling effect leads to higher leaf and canopy temperatures in comparison to a well-watered plant (see section 2 of this Chapter). Normally, the leaf temperature of a fully transpiring plant is about 2 – 5 K below the ambient air temperature (Jones, 1999b). Thus, leaf or canopy temperature depends highly on stomatal conductance (Jones, 2004a). Accordingly, as stomatal closure is the first plant response to water deficit, thermal remote sensing of leaf and/or canopy temperature has become an established technique to detect pre-visual

water stress detection (*e.g.*, Costa *et al.*, 2013; Idso *et al.*, 1981, 1977a; Jackson *et al.*, 1981; Jones, 2004b; Maes and Steppe, 2012).

The major limitation of this temperature-based approach is that the use of leaf or canopy temperature values alone cannot directly estimate the physiological status of crop plants (Inoue *et al.*, 1990). This is because leaf temperatures measured under natural field conditions are very sensitive to highly fluctuating environmental factors such as air temperature, humidity, vapour pressure deficit (VPD), wind speed and incident radiation. Therefore, a variety of crop water stress index approaches have been developed in the past with the aim of estimating plant water stress more quantitatively by normalizing radiatively measured leaf temperatures to actual environmental conditions. Following, a concise overview of the most important approaches of TIR sensing for water stress detection is given (see Costa *et al.*, 2013; Jones, 2004a; Maes and Steppe, 2012 for comprehensive reviews).

The first development was the normalization of plant temperatures against air temperature formulated in the Stress Degree Day (SDD) by Jackson *et al.* (1977) and Idso *et al.* (1977b). This approach is based on the difference between leaf and air temperature ( $T_{leaf} - T_{air}$ ) measured 1 – 1.5 hours after solar noon. Appearance of water stress is assumed as soon as  $T_{leaf} - T_{air}$  rises above 0 K.

A further improvement of SDD was the commonly established and mostly used index for remotely sensed water stress detection, the Crop Water Stress Index (CWSI, Idso *et al.*, 1981b; Jackson *et al.*, 1981):

$$CWSI = \frac{T_{leaf} - T_{wet}}{T_{dry} - T_{wet}} \quad (I-1),$$

where  $T_{leaf}$  is the measured leaf temperature,  $T_{wet}$  is the lower boundary for canopy temperature, assuming a leaf with stomata fully open and a maximum potential transpiration rate, and  $T_{dry}$  is the upper boundary represented by a non-transpiring leaf with stomata completely closed. The greatest advantage in comparison to the simple approach of SDD is that CWSI considers not only actual air temperature but also other environmental factors (*i.e.*, wind, radiation, VPD, *etc.*) by defining potential boundaries. Therefore, CWSI should be adaptable to any crop under any meteorological condition.

A variety of approaches have been developed to estimate  $T_{wet}$  and  $T_{dry}$  as the input of CWSI calculation. For example, the analytical CWSI is a combination of leaf temperature measurements and actual micro-meteorological data (*e.g.*, wind, air temperature, VPD). Whereas, the empirical approach only accounts for leaf temperature, air temperature, VPD and two empirically determined crop-specific variables (Maes and Steppe, 2012).

However, CWSI works well in dry and hot climates with high VPD, but is limited in humid climates with lower VPD and higher variability in wind speed, cloud cover and thus incident radiation (Jones,



2004a). Therefore, the most powerful approach to overcome these problems is the use of artificial reference surfaces. This approach allows simultaneous measurement of reference and leaf temperature. To simulate  $T_{wet}$ , an artificial surface with the same aerodynamic properties or a natural leaf is sprayed with a thin water layer on one or both sides.  $T_{dry}$  can be created by covering natural leaves with petroleum jelly or by using an untreated artificial reference surface. The main advantage of using reference surfaces is that no additional meteorological measurements are required and all needed values can be measured within the same image (e.g., Jones, 2004a; Maes *et al.*, 2016; Maes and Steppe, 2012). However, the use of artificial reference surfaces presents some problems with regard to the choice of material and its handling in the field. In principle, it should have the same aerodynamic and optical properties as real leaves. Further, its spectral emissivity must be close or similar to the emissivity of the observed leaves to prevent errors in temperature estimation (Jones, 2004a). At airborne and satellite scale the application of artificial reference surfaces seems to be difficult (Jones *et al.*, 2009a) and could be replaced by larger wet references as suggested by Meron *et al.* (2003).

Alternative derivatives of the CWSI are the Water Deficit Index (WDI, Moran, 1994) and the thermal index of relative stomatal conductance ( $I_G$ , Jones, 1999a). WDI takes advantage of an optical VI (e.g., NDVI) to separate vegetation from soil pixels within a field. Based on some rearrangement of the leaf energy balance equation,  $I_G$  has the advantage over CWSI that it is directly linearly related to stomatal conductance (Maes and Steppe, 2012). Since temperature-based indices are only relative measures of plant stress, the physically-based modelling of evapotranspiration could offer an alternative approach not only for the detection of plant responses to water deficit but also to gain further insights into the interaction of plants with the intervening pedosphere and atmosphere under environmental stress conditions. For example, Mallick *et al.* (2015) provide a physically-based model approach to retrieve evapotranspiration from remotely sensed surface temperatures, called Surface Temperature Initiated Closure (STIC). STIC is based on the integration of surface temperature into the Penman-Monteith (PM) equation and offers the opportunity to be conducted on field-, regional- and global scale.

Because of the enormous potential of temperature-based indices for the pre-visual detection of plant responses to water stress, many airborne (e.g., AHS, TIMS, ATLAS) and satellite (e.g., ASTER, AVHRR, MODIS, Landsat series) TIR sensors have been developed and have been applied in agriculture (see Khanal *et al.*, 2017 for review). However, satellite sensors have limitations for applications in precision agriculture because of their low spatial and temporal resolution. For example, the best spatial resolution with 100 m is delivered by Landsat 8, which, for most agricultural cultivation systems, corresponds to a single field per pixel (Mahlein, 2016). Thus, recent developments in TIR remote sensing from airborne and Unmanned Aerial Vehicles (UAVs) have great potential to bridge the gap between low-resolution satellite images and small-scale *in situ* measurements. For example, Berni *et al.* (2009)

demonstrated the ability of quantitative UAV remote sensing for a number of agricultural applications by using thermal and narrowband multispectral optical sensors.

However, for the majority of studies, broadband TIR sensors are used to estimate temperature-based indices for the detection of plant responses to water stress (Grant *et al.*, 2012, 2007, 2006; Jones *et al.*, 2009a; Zarco-Tejada *et al.*, 2013). Broadband TIR imagers (*i.e.*, one spectral band in the wavebands of 7 – 14  $\mu\text{m}$ ) are based on the assumption of a constant emissivity (*e.g.*, 0.97 for vegetation), which does not exist in nature (Ullah *et al.*, 2012b). Thus, neglecting the spectral emissivity of the leaves themselves limits the accuracy of temperature estimation. For example, an error in the assumed emissivity of 1 % results in absolute temperature errors of about 1 K (Jones, 2004a). However, new hyperspectral TIR imagers provide innovative techniques to overcome this limitation by many narrowband measures, which allow precise spectral emissivity retrieval and hence better surface temperature estimation compared to broadband thermal cameras (for more details see section 3.1.3 in this Chapter).

### 3.1.2 Emissivity Approach

Despite a variety of geological applications using TIR spectroscopy (*e.g.*, Hecker *et al.*, 2011; van der Meer *et al.*, 2012), up to now, hyperspectral TIR remote sensing of plant properties has received little attention. The general assumption that vegetation does not provide suitable spectral features in the TIR to study plant physiological traits depends on several issues as summarized by Ribeiro da Luz and Crowley (2007): (i) general lack of hyperspectral instruments for remote sensing (most available setups are based on laboratory equipment), (ii) very low and complex spectral emissivity variations are originating from complex plant physiological and biochemical processes, (iii) low SNR as well as low spatial and spectral resolution of airborne or satellite remote sensing TIR sensors fail to detect minor variations in plants TIR spectral fingerprint, (iv) proper atmospheric correction and advanced temperature emissivity separation (TES) methods are needed to retrieve accurate emissivity spectra.

Only few scientists have studied vegetation spectra in TIR thus far. Salisbury (1986) was the first who recognized detectable spectral variations in fresh leaves of 13 different tree species using Directional Hemispherical Reflectance (DHR) measurements at laboratory level. In 2007, Ribeiro da Luz and Crowley associated vegetation spectral features to leaf chemical compounds such as cellulose, xylan, lignin, cutin and silica. Further, they were the first who carried out suitable field, canopy and airborne measurements of vegetation spectra in the TIR (Ribeiro da Luz and Crowley, 2010). These findings, together with recent advances in sensor technology and the availability of hyperspectral TIR imagers (*e.g.*, Telops *Hyper-Cam LW*, Speciem AisaOWL, Itres TASI-600, SEBASS (Spatially Enhanced Broadband Array Spectrograph System)) facilitate new possibilities to detect environmental stress based on spectral emissivity.

The main underlying advantage of TIR spectral information in comparison to the VNIR/SWIR domain is that TIR spectral features originate from primary absorption bands of biochemical leaf compounds (*e.g.*, cellulose) and should thus exhibit higher spectral contrast as VNIR/SWIR spectra which are mainly dominated by overtones and combination modes of fundamental vibrations originating from the interactions between solar radiation and leaf contents (*e.g.*, leaf pigments). Therefore, changes in the compositions of leaf constituents due to osmotic adjustment induced by water stress should be accompanied with changes in the emissivity spectra. However, only little effort has been directed to the detection of plant responses to environmental stresses based on spectral emissivity. Buitrago *et al.* (2016) showed the ability of spectral emissivity to detect water and cold stress on both European beech (*Fagus sylvatica*) and rhododendron (*Rhododendron cf. catawbiense*) leaves using DHR laboratory measurements. Using spectral emissivity measurements from a field experiment Buddenbaum *et al.* (2015) were able to differentiate stressed from non-stressed European beeches (*Fagus sylvatica*).

The retrieval of spectral emissivity and surface temperature requires an exact pre-processing of hyperspectral TIR images which is detailed in the next section.

### 3.1.3 Hyperspectral TIR Image Pre-Processing

In order to derive both accurate surface temperatures and emissivity spectra from hyperspectral TIR data, two fundamental problems have to be solved (*e.g.*, Kealy and Hook, 1993; Schmugge *et al.*, 2002; Sobrino *et al.*, 2008). First, atmospheric correction is needed, hence, the spectral radiance measured at sensor consists not only of the radiance emitted by the object of interest itself, but also includes thermal radiation emitted by surroundings and reflected from the surface of the object (down-welling radiance, DWR). It is further influenced by the intervening atmosphere in terms of absorption, emission and scattering (upwelling radiance and transmittance ( $\tau$ ) of the atmosphere). Upwelling path and  $\tau$  can be neglected for short distance measurements, but should be corrected for airborne or satellite imagery. Second, a solution of the so-called TES-problem (Temperature Emissivity Separation) is required. The measured spectral radiance is, with regard to Planck's law, a function of the absolute temperature and the spectral emissivity of the observed object. Thus, if the radiance is measured in  $n$  channels, there will be  $n + 1$  unknowns,  $n$  emissivities values, plus the surface temperature. Therefore, to retrieve accurate surface temperatures, the spectral emissivity must be known and vice versa.

While in theory the equation is still underdetermined, hyperspectral data in comparison to multispectral data allows a good fit to Planck's radiance curve for a specific temperature (Vaughan *et al.*, 2003). Nowadays, a variety of algorithms exist which differ in the underlying assumptions and the data basis. A comprehensive review is given by Li *et al.* (2013). In general, it must be distinguished between short (indoor and outdoor measurement with 1 – 3 m) and large (field or air- and space-borne measurements) sensor – target distances. The 'spectral smoothness' method introduced by Horton *et al.* (1998)

is the most accurate TES-approach for short distance field measurements. This is because no *a priori* knowledge - neither the maximum value of the emissivity nor the corresponding wavenumber - are required. The atmospheric emission lines (*i.e.*, H<sub>2</sub>O) are negatively oriented if the sample temperature is overestimated and vice versa. Using this atmospheric characteristic, the target emissivity spectrum can be accurately retrieved by iteratively changing the target temperature. However, this approach is only suitable for outside measurement in the presence of atmospheric water vapour lines. For indoor measurements, the Reference Channel or the Blackbody Fit should be used alternatively (Hecker *et al.*, 2013). Concerning measurements from greater distance (field, airborne or satellite), atmospheric upwelling path and  $\tau$  cannot be neglected. The ‘Automatic Retrieval of Temperature and Emissivity using Spectral Smoothness’ (ARTEMIS) by Borel (2003) is a hybrid approach, combining atmospheric correction and TES. First, the required atmospheric parameters (DWR, upwelling,  $\tau$ ) are determined using a MODTRAN (MODerate resolution atmospheric TRANsmission) look-up-table (LUT). To this end, a pre-selection of potential atmospheric parameters is completed by using the ‘In Scene Atmospheric Compensation’ (ISAC) approach by Young *et al.* (2002). Finally, spectral emissivity is retrieved using a spectral smoothness approach called ISSTES (Iterative Spectrally Smooth Temperature and Emissivity Separation, Borel, 1997). In comparison to other in-scene atmospheric correction approaches, such as ISAC or AAC (Autonomous Atmospheric Compensation, Gu *et al.*, 2000), ARTEMIS does not require any *a priori* knowledge and considers DWR. Therefore, ARTEMIS can be considered the state-of-the-art algorithm for hyperspectral TIR airborne data.

### 3.2 Solar-Reflective Domain

Over the past four decades, remote sensing of vegetation has focused on the solar- or optical-reflective domain of the electromagnetic spectrum (0.4 – 2.5  $\mu\text{m}$ ; VNIR/SWIR) with a large number of available multi- and hyper-spectral sensors at ground- (*e.g.*, ASD FieldSpec, SpectralEvolution PSR+), airborne- (*e.g.*, AVIRIS, HyMap, HySpex, Aisa EAGLE), and spaceborne-level (*e.g.*, Landsat, SPOT, MODIS, IKONOS). Optical-reflective remote sensing is based on the spectral reflectance properties of mainly the leaves, the canopy and the underlying soil. (Peñuelas *et al.*, 1994; Pinter Jr. *et al.*, 2003). The visible spectral range (0.4 – 0.7  $\mu\text{m}$ ) is primarily sensitive to leaf pigments, while the near infrared (0.7 – 1.3  $\mu\text{m}$ ) and the shortwave infrared (1.3 – 2.5  $\mu\text{m}$ ) are predominantly sensitive to leaf cell structure and canopy structure and leaf/canopy water content, respectively. Especially hyperspectral data opened the opportunity for the development of narrowband vegetation indices (VIs), simplifying the interpretation of complex vegetation reflectance signatures based on their indirect relationships to plant physiological and structural parameters (Govender *et al.*, 2009). Numerous VIs have been developed to detect plant water stress based on VNIR/SWIR reflectance. Since most VIs are based on empirical relationships under specific experimental conditions, they are suffering from limitations of transferability to different species or environmental conditions (Jones and Vaughan, 2010).

Since the leaf chlorophyll content may decrease under water stress conditions (see section 2 of this Chapter), numerous narrowband spectral indices sensitive to leaf chlorophyll were developed (Haboudane *et al.*, 2002). While some chlorophyll-based spectral indices are sensitive to leaf color (*i.e.*, yellowing of the leaf) such as the Simple Ratio (SR, Asrar *et al.*, 1984), Normalized Difference Vegetation Index (NDVI, Rouse *et al.*, 1974) is sensitive to both chlorophyll content and canopy structural parameters (*i.e.*, changes in leaf area index (LAI)).

Leaf water content is highly correlated with water absorption bands in the NIR and SWIR (Tucker, 1980). Since leaf water content is decreased with prolonged or severe water stress (see section 2 of this Chapter), changes in the corresponding leaf reflectance signal (*i.e.*, saturation of water absorption bands) can be used to calculate water content related VIs. For example, simple ratio indices like the Water Index (WI) (Peñuelas *et al.*, 1993), the Leaf Water Index (LWI) (Seelig *et al.*, 2008) and the Moisture Stress Index (MSI) (Hunt Jr. and Rock, 1989), are sensitive to variations in the water absorption bands at 0.97  $\mu\text{m}$  and 1.45  $\mu\text{m}$ , respectively.

However, VIs related to chlorophyll or leaf water content are related to late plant responses which tend to arise with visible symptoms (*i.e.*, changing leaf color, leaf rolling or wilting). Thus, it can be assumed that their usage for pre-visual water stress detection in crops is limited.

As another narrowband spectral index, the Photochemical Reflectance Index (PRI, Gamon *et al.*, 1992) is sensitive to variations in the leaf xanthophyll pigments. PRI is directly linked to the photosynthetic process due to short-term changes in xanthophyll pigments under stress conditions. Therefore, PRI is considered a pre-visual proxy for water stress detection. For instance, Suárez *et al.* (2009) and Panigada *et al.* (2014) illustrated the feasibility of PRI as a pre-visual water stress indicator at airborne level. Suárez *et al.* (2009) observed robust relationships with canopy temperatures for various crops (*e.g.*,  $r^2=0.8$  for peach trees,  $r^2=0.65$  for olive trees,  $r^2=0.72$  for maize). Additionally, Panigada *et al.* (2014) found that PRI is more sensitive to an early plant water stress stadium than traditional VIs (*e.g.*, NDVI). However, the ability of the PRI to be used for water stress detection is not conclusive (Gerhards *et al.*, 2016; Panigada *et al.*, 2014; Rossini *et al.*, 2015b).

### 3.3 Sun-Induced Fluorescence (SIF)

As narrowband reflective VIs underlie several limitations, especially in their capability of an early or pre-visual stress detection, remote sensing of sun-induced fluorescence (SIF) has become more and more prominent over the last decade (see Meroni *et al.* (2009) for a comprehensive review). SIF is the passive measurement of chlorophyll fluorescence emission peaks centered at 670 nm and 760 nm and is considered a direct indicator of photosynthetic efficiency (Rascher *et al.*, 2015). The utility of SIF for monitoring the functional status of actual photosynthesis and the detection of plant responses to environmental stresses has been examined in ground-based experiments, airborne campaigns and even towards satellite missions (Meroni *et al.*, 2009).

Simplified, the rationale for remote sensing of SIF is based on the competitive interactions of how radiative energy absorbed by leaf chlorophyll is processed within the plant: (i) most of the energy is used for the photochemical conversion to sugars through photosynthesis, (ii) the non-used energy is rapidly re-emitted through chlorophyll fluorescence or (iii) heat dissipation (Porcar-Castell *et al.*, 2014). Since CO<sub>2</sub> uptake is reduced under water stress conditions and thus energy used by photosynthesis is also decreased, meanwhile the amount of radiative energy remains constant, SIF and/or heat dissipation would consequently also change. Therefore, changes in SIF might be highly correlated with photosynthetic efficiency and it can thus be assumed to be a proxy for early detection of plant responses to water stress (Rascher *et al.*, 2015; Rossini *et al.*, 2015a; Wieneke *et al.*, 2016).

Many ground-based studies have been undertaken to demonstrate the feasibilities of fluorescence sensing to detect and monitor plant stresses. However, current advances in sensor technology have opened new opportunities to focus on SIF imaging from airborne and even spaceborne platforms. Since the fluorescence signal is considerably lower (about 1 – 2 % of the radiation absorbed by chlorophyll) than the plant reflectance used by optical sensor systems, a sensor for SIF sensing requires an extremely high signal-to-noise-ratio (SNR) which traditionally limits other sensor abilities (*i.e.*, spectral and/or spatial resolution). Apart from this limitation, the fluorescence emission peaks appear in super-narrow spectral windows (*i.e.*, around 670 nm and 760 nm), requiring extremely high spectral resolution in the range of nanometers. Notwithstanding, major potential of SIF remote sensing could be presumed from the FLEX (Fluorescence Explorer) satellite mission supported by the European Space Agency (ESA). The aim of the FLEX mission is to measure the full spectrum of SIF emission with a spectral resolution of 0.2 nm (Rascher *et al.*, 2015). As a preliminary concept of FLEX, *HyPlant* airborne sensor (Forschungszentrum Jülich (Germany) and Specim Spectral Imaging Ltd (Finland)) enables sub-nanometer imagery of the red (670 nm) and far red (760 nm) SIF emission peaks. Although recent experiments based on *HyPlant* data demonstrated the utility of SIF for quantitative plant stress detection at airborne level (Rossini *et al.*, 2015a, 2015b), further multi-sensor airborne studies (*e.g.*, comparative research of SIF, VNIR/SWIR and TIR) are needed to establish a consistent basis for a robust assessment.

### 3.4 Multi-Sensor Approach

Since different plant stresses co-occurring under field conditions cause various plant responses, a multi-sensor approach not only provides useful information about actual plant status but also on the causes of biophysical, physiological and photochemical changes. Several airborne studies examined the relationship between different remote sensing approaches for water stress detection, ranging from optical indices over SIF to temperature-based indices. For example, Zarco-Tejada *et al.* (2013) examined the performance of a new formulation of PRI over an experimental vineyard site with three different irrigation treatments. They found that the new normalized PRI, a combination of Renormalized Difference Vegetation Index (RDVI, Roujean and Breon (1995), as an structural index) and the red edge ratio index ( $R_{700}/R_{670}$ , which is sensitive to pigment content), allows for better detection of diurnal changes in stomatal conductance and thus is a better proxy for early water stress detection compared to the original PRI. A further comparative analysis on airborne level was performed by Panigada *et al.* (2014). They found that temperature-based indices performed best in comparison to SIF and optical indices (*e.g.*, PRI) in cereal crops under different irrigation levels. However, they suggested an integrated use of thermal and narrowband optical imagery to accurately retrieve stress-related plant responses as an input for agricultural applications (*e.g.*, irrigation scheduling, phenological growth stage, agricultural species detection).

In 2018 four innovative earth observations instruments will be tested for potential future satellite-based plant function monitoring on the International Space Station (ISS) (Stavros *et al.*, 2017). This multi-sensor approach covers a wide range of instruments for the survey of novel regional and global insights into ecosystem processes and functions. The instruments are: the Global Ecosystem Dynamics Investigation (GEDI, NASA), the Ecosystem Spaceborne Thermal Radiometer Experiment on Space Station (ECOSTRESS, NASA), the Orbiting Carbon Observatory (OCO-3, NASA), and the Hyperspectral Imager Suite (HISUI, JAXA). GEDI carries a LIDAR measuring canopy structural parameters (*e.g.*, height, biomass). TIR data products (*i.e.*, surface temperature, evapotranspiration) will be delivered by ECOSTRESS. SIF is measured by OCO-3 and HISUI delivers surface reflectance (10 nm spectral resolution) in the VNIR/SWIR. The data products will be freely available and will open the unique opportunity for scientists to examine the performance and capabilities of such innovative satellite-based multi-sensor approach to study plant functioning and the response to environmental stress in a wide range of ecosystems. However, before the plant functioning monitoring on ISS will be established, multi-sensor research is limited to ground and airborne studies.

## 4 Objectives

As a matter of fact, it remains unclear to what extent current state-of-the-art hyperspectral remote sensing techniques can contribute to detect environmental stresses. It is also unclear how and why indices of different spectral domains respond to water stress. Therefore, the overall aim of this thesis is to compare and assess different remotely sensed indices for their ability to detect plant responses to water deficit stress.

Following, the specific objectives of this dissertation are listed:

**Objective I: A comparative assessment of hyperspectral remote sensing indices for water deficit stress detection** – A systematic comparison of the ability of different temperature-based indices (*e.g.*, CWSI), spectral emissivity, traditional VNIR/SWIR indices (*e.g.*, PRI, NDVI, WI, MSI), and SIF indices to detect plant water stress symptoms. Additionally, provide an assessment of the sensitivity of the different indices for the detection of water stress with respect to the underlying physiological processes.

**Objective II: Assess the potential of hyperspectral remote sensing indices for water stress detection at airborne level** – Compare the sensitivities of different indices at ground and airborne levels and provide an outlook to the prospects of satellite remote sensing of water stress detection.

**Objective III: Examination of the advantages of hyperspectral TIR remote sensing sensors for the retrieval of temperature and emissivity** – First, providing a comparison of hyperspectral and broadband TIR imaging systems with respect to their temperature retrieval accuracy as a basis for water stress detection. Second, examine the abilities of spectral emissivity of vegetation to detect water stress.

**Objective IV: Assess the effect of plant species on spectral emissivity** – Investigate if different plant species show pronounced differences in spectral emissivity derived from hyperspectral TIR imaging spectroscopy and use the derived emissivity spectra in comparison with VNIR/SWIR reflectance for species classification.



## 5 Overview and Structure of the Thesis

To provide an overview of the following chapters, short summaries of the main part of this thesis - the publications - are introduced. Three of the four presented manuscripts have been published in peer-reviewed journals. The latest research paper (Chapter IV) has been submitted to a peer-reviewed journal. Further, large parts of the introduction- (Chapter I) and synthesis chapter (Chapter VI) have been used in a review paper which is ready for submission to a peer-reviewed journal. All subjected journals are listed in the Science Citation Index Expanded (SCIE) established by the Institute for Science Information (ISI). Finally, a synthesis of the thesis is provided in Chapter VI to depict the internal coherence of the standalone publications and to give a comprehensive conclusion and outlook.

### **Chapter II: “A Hyperspectral Thermal Infrared Imaging Instrument for Natural Resources Applications”**

In this paper, first comparative measurements and a detailed instrument description of the Telops *Hyper-Cam LW* is presented. This device was also used in all following publications. The base instrument, the Telops *Hyper-Cam LW*, is a hyperspectral thermal infrared imaging spectrometer measuring emitted radiation in the 8 to 12  $\mu\text{m}$  range at a spectral resolution of up to  $0.25\text{ cm}^{-1}$ . The base instrument can be extended with a customized fore-optic allowing vertical measurements at ground and an airborne platform for aerial image acquisitions. Thus, the Telops *Hyper-Cam LW* has a large variety of applications including laboratory-, field- and airborne-scale.

The main findings of this study were: (i) first tests with *Hyper-Cam LW* on rock samples showed that the measured spectral emissivity is in overall good agreement in comparison to reference spectra measured by laboratory spectrometers (Bruker Vertex 70 (ITC) and JHU spectral library), (ii) based on this results, airborne measurements are supposed to provide high spatial resolution land surface emissivity and temperature maps for environmental monitoring (*e.g.*, plant water stress detection).

### **Chapter III: “Water Stress Detection in Potato Plants using Leaf Temperature, Emissivity, and Reflectance”**

In a first ground-based experiment, a systematic comparison of remote sensing techniques for water stress detection was performed based on 60 potato plants, half of them watered and the other half deprived of water. The overall aim of this study was to evaluate the ability of detecting plant responses induced by water stress using: (i) stomatal conductance as measured by leaf porometry, (ii) temperature-based indices retrieved from broadband and hyperspectral TIR imaging, (iii) spectral emissivity measured by hyperspectral TIR imaging, and (iv) traditional VNIR/SWIR based indices.

The results of the experiment showed that water stress was detectable two days after stress initiation as measured by stomatal conductance. Concerning remote sensing data, temperature-based indices (*e.g.*, CWSI), VNIR/SWIR indices related to plant water content (*e.g.*, MSI) and spectral emissivity were equally sensitive starting seven days after watering was stopped. Whereas, visual indices (*e.g.*, PRI) were either not sensitive to water stress symptoms at all or responded in an inconsistent manner. As an additional result, we did not examine striking differences between hyperspectral and broadband TIR imagers in deriving accurate leaf temperatures.

In conclusion, the most important finding of this research is that pre-visual measures of plant responses to water stress (*i.e.*, temperature-based indices, spectral emissivity and VNIR/SWIR based indices related to plant water content) react faster than visual measures (*i.e.*, based on leaf colour). Since pre-visual measures are based on the plant physiological response to water shortage (*i.e.*, stomatal closure), the findings should also be transferable to different crops and growth stages. However, for a potential application of TIR imaging in precision agriculture, further airborne experiments are mandatory to transfer the findings of this study from plant- to field- and regional scale.

#### **Chapter IV: “A Comparative Analysis for Remote Sensing of Plant Water Stress Symptoms Based on Airborne Optical and Thermal Hyperspectral Images”**

In a second experiment at airborne-level, water stress symptoms over a commercial grass (*Festuca arundinacea* and *Poa pratense*) farm were induced by modifying plant physiological characteristics with an anti-transpirant agent (Vapor Gard; VG) which reduced stomatal conductance, and a highly reflective powder (kaolin, KA), which increased plant surface albedo. State-of-the-art airborne remote sensing indices were retrieved from hyperspectral thermal (TIR), sun-induced fluorescence (SIF) and hyperspectral optical (VNIR/SWIR) images in order to evaluate their potential for the detection of water stress symptoms at airborne level. Airborne images were acquired at three time points during the day. The objectives of the study were: (i) to systematically compare and assess the strength of different TIR indices (*e.g.*, CWSI,  $T_s$ ,  $T_s - T_a$ ), VNIR/SWIR indices (*e.g.*, PRI, NDVI, WI, MSI), and SIF for the detection of plant symptoms as induced by chemical agents (*i.e.*, VG and KA), (ii) to examine diurnal changes in TIR index values concerning the chemical agents.

Similar to the results of the ground-based study, temperature-based indices were most sensitive to water stress symptoms compared to traditional VNIR/SWIR indices and SIF indices. In particular, the results showed that surface temperature ( $T_s$ ) was regulated by plant transpiration. Consequently,  $T_s$  increased in plots treated with VG due to reduced stomatal conductance, while  $T_s$  was consistently lower because of the reduced available energy in plots treated with KA in comparison to control plots. Since the changes to the photosynthetic efficiency and to the leaf biochemical constituents induced by the VG

treatment were too subtle, neither significant effects on SIF indices nor on VNIR/SWIR indices were recognized. In contrast, the increased plant albedo induced by KA treatment reduced  $fAPAR$  resulting in a significant reduction of SIF, and in a change of VNIR/SWIR indices.

However, a hyperspectral multi-sensor airborne approach with its high spatial, spectral and temporal resolution has great potential to bridge the gap between *in situ* and satellite observation. Furthermore, such concepts provide profound insights about the actual plant status and the rationale of physiological and biochemical changes.

### **Chapter V: “Plant species discrimination using emissive thermal infrared imaging spectroscopy”**

Plant species discrimination has always been one of the major topics in remote sensing of vegetation. However, the effect of different plant species on the emissivity spectrum is not fully understood yet. Thus, research in how the emissivity signal varies between different species can provide further advances in the understanding of the origin of spectral emissivity features and their application for the detection of plant responses to environmental stresses. The aims of the study were: (i) to assess the quality of TIR imaging spectrometer (*i.e.*, *Hyper-Cam LW*) for measuring leaf spectral emissivity in comparison to laboratory reference spectra, (ii) to examine the effect of plant species on plant emissivity. Therefore, a ground-based experiment based on eight different plant species was conducted.

In this study it was demonstrated that: (i) mean emissivity spectra as measured by *Hyper-Cam LW* were in very good agreement with the reference spectra (average Nash-Sutcliffe-Efficiency Index = 0.64), (ii) different species could be accurately classified based on species-specific spectral emissivity features. In conclusion, spectral emissivity as measured by hyperspectral TIR remote sensing offers great potential for detection and monitoring not only of earth surface materials with great spectral contrast (*i.e.*, gases, minerals and rocks) but also of very subtle features with low spectral contrast like vegetation (*i.e.*, less than 5 % absolute emissivity differences). This finding opens the opportunity to use spectral emissivity features of vegetation for the detection of plant responses to environmental stresses such as water stress.



# Chapter II

## **A Hyperspectral Thermal Infrared Imaging Instrument for Natural Resources Applications**

*Remote Sens.* 4 (12),

*December 2012, 3995 – 4009.*

DOI: 10.3390/rs4123995

Martin Schlerf, Gilles Rock, Philippe Lagueux, Franz Ronellenfitsch,  
Max Gerhards, Lucien Hoffmann and Thomas Udelhoven

© 1996-2017 MDPI AG (Basel, Switzerland) unless otherwise stated.

The following manuscript is a copy of the final version of the accepted manuscript. The paper has been through peer review, but it has not been subject to copy-editing, proofreading and formatting added by the publisher. The contribution of Max Gerhards to this scientific paper was the development and implementation of the experimental setup including sample preparation, measurement setup and data acquisition. In addition, Max Gerhards was involved in processing and analysing the data.

The version-of-record can be accessed at:

<http://www.mdpi.com/2072-4292/4/12/3995>

## Abstract

A new instrument has been setup at the Centre de Recherche Public-Gabriel Lippmann to measure spectral emissivity values of typical earth surface samples in the 8 to 12  $\mu\text{m}$  range at a spectral resolution of up to  $0.25\text{ cm}^{-1}$ . The instrument is based on a *Hyper-Cam LW* built by Telops with a modified fore-optic for vertical measurements at ground level and a platform for airborne acquisitions. A processing chain has been developed to convert calibrated radiances into emissivity spectra. Repeat measurements taken on samples of sandstone show a high repeatability of the system with a wavelength dependent standard deviation of less than 0.01 (1.25 % of the mean emissivity). Evaluation of retrieved emissivity spectra indicates good agreement with reference measurements. The new instrument facilitates the assessment of the spatial variability of emissivity spectra of material surfaces—at present still largely unknown—at various scales from ground and airborne platforms and thus will provide new opportunities in environmental remote sensing.

## 1 Introduction

Over the last three decades airborne hyperspectral imaging has become a major tool in environmental remote sensing for studying the Earth's surface and the atmosphere. The 0.35  $\mu\text{m}$  to 2.5  $\mu\text{m}$  spectral range is dominated by reflected sunlight and is well suited for detecting the spectral features related to electronic transitions (*e.g.*, iron oxides,  $\text{Fe}^{2+}$  bearing minerals, chlorophyll, *etc.*) and harmonics and combination bands of vibrational absorptions (*e.g.*, OH,  $\text{SO}_4$ ,  $\text{CO}_3$ , CH, *etc.*) in minerals, soils, vegetation, and the atmosphere. Thermal infrared (TIR) data provides complementary information in terms of spectral emissivity and temperature of environmental targets, such as key rock and soil forming minerals, specific gaseous components, and vegetation. The 8  $\mu\text{m}$  to 14  $\mu\text{m}$  spectral range spans the radiant energy peak of ambient temperature of the Earth (300 K), whereas the 3  $\mu\text{m}$  to 5  $\mu\text{m}$  band corresponds to the radiant energy peak for hot features ( $>600$  K) such as fires and lava flows according to Wien's displacement law (Jensen, 2007). Numerous studies have demonstrated the use of TIR data for many thematic areas and applications, for instance landscape characterization, determination of mineral and soil properties (Eisele *et al.*, 2012), estimation of energy fluxes (Frey and Parlow, 2012) estimation of evapotranspiration and soil moisture, drought monitoring, urban heat islands (Ogashawara and Bastos, 2012), detection of forest fires, coal fires and volcanoes (Carter and Ramsey, 2010) (compare *e.g.*, Jensen (2007) and Vollmer & Möllmann (2010) for a comprehensive overview). Currently, TERRA-AQUA/MODIS and other sensors provide low spatial resolution ( $>1$  km) TIR data. Medium spatial resolution TIR data ( $\sim 100$  m) is provided by TERRA/ASTER and Landsat/TM-ETM+, which will be followed by the Landsat Data Continuity Mission (LDCM, 2 TIR bands, Launch: 2013, <http://ldcm.nasa.gov/> (Schott *et al.*, 2012)) and by the Hyperspectral Infrared Imager (HypIRI, 7 TIR bands, Launch: 2020, <http://hypiri.jpl.nasa.gov/>). High resolution TIR data ( $\sim 10$  m) is currently only available through on-demand flights in which multispectral or hyperspectral sensors are placed on aircrafts.

Improvements of infrared technology have led to hyperspectral acquisitions in the TIR, *i.e.*, images acquired with hundreds of contiguous spectral channels rather than just 5–10 multispectral channels. While this imaging approach has been used since the 1980s in the visible, near-infrared, and shortwave infrared region, there are presently only a limited number of hyperspectral imaging instruments that operate in the TIR. Hyperspectral TIR instruments operational for airborne surveys, include the thermal emission spectrometer on the Mars Global Surveyor spacecraft (Christensen *et al.*, 2001), the airborne hyperspectral imager (AHI, (Lucey *et al.*, 2001)), the spatially enhanced broadband array spectrograph system (SEBASS, (Hackwell *et al.*, 1996)), Itres TASI-600 (<http://www.itres.com/>), Specim AisaOWL (<http://www.specim.fi>) and the Telops *Hyper-Cam LW* (Lagueux *et al.*, 2009). These instruments are dispersive infrared spectrometers, with the exception of the *Hyper-Cam LW* that belongs to the class of Fourier transform infrared (FTIR) spectrometers. The

main advantage of FTIR-spectrometers over conventional dispersive instruments is their higher achievable signal-to-noise ratio that is based on the following properties (Vollmer and Möllmann, 2010): the detector signal in an FTIR-spectrometer contains the contributions of all wavelengths whereas in a conventional dispersive spectrometer the wavelength bands are observed sequentially while scanning the grating. Therefore, in comparable measuring conditions (same detector, measurement time, spectral resolution, optical throughput and optical efficiency) there is an improved signal-to-noise ratio of FTIR-instruments by  $N^{1/2}$ , where  $N$  is the number of recorded wavelengths (Hirschfeld, 1976). This is referred to as the Fellgett advantage (also known as the multiplex effect or multiplex advantage). Furthermore, in an interferometer a higher energy throughput and thus, a higher detector signal can be measured. This is known as the Jacquinot advantage (or throughput advantage) and is due to the absence of conventional slits in the interferometer to define the spectral resolution. An additional property of FTIR instruments is their ability for self-calibration. This is achieved by a frequency-stabilized laser (*e.g.*, a HeNe-laser) that is used as an internal wavelength standard and that allows to measure optical path difference of the moving mirror very precisely from the laser interferogram, the so-called Connes advantage.

Clearly, the new hyperspectral thermal infrared instruments require the same level of research for the development of image analysis and processing techniques, field calibration and validation, and new methods for surface characterization, as previous instruments. To date, only a few scientific publications on the calibration and analysis of hyperspectral TIR image data have been published, *e.g.*, Ribeiro da Luz and Crowley (2010), Puckrin *et al.* (2012), Vaughan *et al.* (2003). In this paper we describe a new instrumental setup at the Centre de Recherche Public-Gabriel Lippmann (Belvaux, Luxembourg) with a processing chain to measure spectral emissivity values and surface temperature of typical earth surface samples in the 8 to 12  $\mu\text{m}$  range. Contrary to similar existing instruments, this new design allows for vertical measurements at ground level and airborne acquisitions from an airborne platform.

Accurate interpretation of TIR data requires the separation of temperature and emissivity. The difficulty in the temperature-emissivity separation for multispectral thermal sensors is that the solution equations are underdetermined making it difficult to uniquely separate these two parameters. While in theory this is also under-determined for hyperspectral data, the large number of wavelengths allows a good fit to the Planck radiance for a single temperature (Vaughan *et al.*, 2003). A number of approaches based on different assumptions have been developed to estimate emissivity (Gillespie *et al.*, 1998; Hook and Kahle, 1996), for instance the temperature-emissivity separation algorithm (TES, (Gillespie *et al.*, 1998)). However, for agricultural applications the TES procedure tends to underestimate emissivities and consequently overestimate land surface temperatures, with potential emissivity errors of up to 2.0 %, resulting in errors of 2 – 3°C (French *et al.*, 2008). Hyperspectral approaches can rely on a large



number of wavelengths which allows a good fit to the Planck radiance to determine land surface temperature or canopy temperature at higher accuracies than multispectral procedures (Ribeiro da Luz and Crowley, 2007; Vaughan *et al.*, 2003).

Laboratory measurements (Hecker *et al.*, 2011) have shown that TIR emissivity spectra are useful for identifying many minerals (Salisbury *et al.*, 1992), rocks, and other solid materials such as plant leaves (Ullah *et al.*, 2012b). However, laboratory spectra commonly do not represent the materials as they would be seen from remote sensing platforms. Besides, the spatial variability of emissivity spectra of material surfaces is largely unknown. Using a hyperspectral TIR imager the emissivity can be examined at various scales depending on platform and sensor viewing geometry (Balick *et al.*, 2009). In this paper we will demonstrate in the laboratory that accurate TIR emissivity spectra can be retrieved by the new Hyperspectral TIR Imager.

## 2 Instrument Setup

### 2.1 Base Instrument

The instrument is based on a *Hyper-Cam LW* (long wave) (Lagueux *et al.*, 2009) built by Telops, Quebec, Canada. The *Hyper-Cam LW* is a lightweight and compact imaging radiometric spectrometer. The spectra measurements are performed using an imaging Fourier-transform spectrometer based on a Michelson interferometer coupled to a  $320 \times 256$  long wave infrared photovoltaic MCT (mercury-cadmium-telluride) focal plane array detector that can be windowed and formatted to fit the desired size. Spectral resolution is user selectable and ranges from 0.25 to  $150 \text{ cm}^{-1}$ . This instrument gives the complete spectrum of each pixel in the image, each pixel having an instantaneous field-of-view of 0.35 mrad.

The instrument features two internal calibration blackbodies mounted in front of the *Hyper-Cam LW* used to perform a complete end-to-end radiometric calibration of the infrared measurements. In its long wave IR version, the instrument has high sensitivity over the 8–12  $\mu\text{m}$  domain. This spectral domain is ideal for passive standoff chemical agent detection at ambient temperatures for which it was originally designed. The sensor also has acquisition and processing electronics, including 4 GB of high-speed DDR-SRAM, with the capability to convert the raw interferograms into radiometrically calibrated spectra using real-time discrete-Fourier transform (DFT). Its weatherproof enclosure provides operability in harsh environments from  $-10^\circ\text{C}$  to  $+45^\circ\text{C}$ .

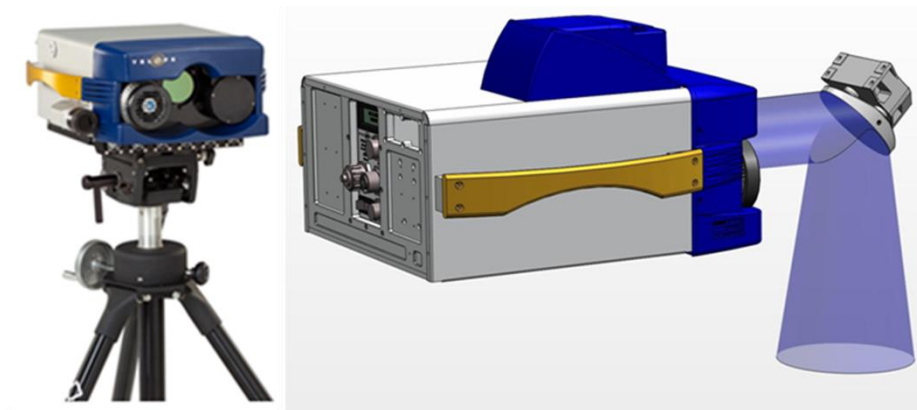
Table II-1: *Hyper-Cam LW* specifications; NESR = noise equivalent spectral radiance.

Parameter	Unit	<i>Hyper-Cam LW</i>
Spectral Range	$\mu\text{m}$	7.7–12
Spectral Resolution	$\text{cm}^{-1}$	0.25 to 150 (user adjustable)
Image Format	-	$320 \times 256$ pixels
Field of View	Degrees	$6.4 \times 5.1$ (nominal)
	Degrees	$25.6 \times 20.4$ (0.25 $\times$ telescope)
Typical NESR	$\text{nW}/\text{cm}^2 \cdot \text{sr cm}^{-1}$	<20
Radiometric Accuracy	K	<1

## 2.2 Modifications: Customized Mirror System, Setup for Vertical Measurements

The *Hyper-Cam LW* was modified to allow for vertical (nadir) measurements of targets at the ground level to resemble the observation geometry obtained from airborne or space-borne platforms. The modification consists in a custom designed folding mirror system and a telescope (Fig. II-1).

The mirror system allows the camera to look downward onto the target by deflecting the upwelling emitted radiation by  $90^\circ$  towards the optical inlet of the *Hyper-Cam LW*. The system itself consists of a  $45^\circ$  tilted gold coated mirror that is located in the instrument's field of view, providing optimal reflectivity in the 8–12  $\mu\text{m}$  spectral range. A 0.25 $\times$  telescope can be optionally installed to cover a sufficiently large field-of-view (FOV) in the vertical mode. The resulting FOV with the 0.25 $\times$  telescope at a sensor-target distance of 1.5 m is  $672 \times 538$  mm at a pixel size of 2.1 mm. Without the telescope the FOV is  $168 \times 134$  mm at a pixel size of 0.525 mm.

Fig. II-1: *Hyper-Cam LW* Sensor (left) and instrument setup for ground measurements (right).

### 2.3 Airborne Module

The airborne module includes a stabilization platform, the Image Motion Compensator (IMC) mirror, a GPS/INS (inertial navigation system) unit and a visible boresighted camera. All these modules are rigidly mounted on a high stiffness base plate. This base plate is mounted on the stabilization platform. Fig. II-2 illustrates the *Hyper-Cam LW* airborne configuration.

The IMC mirror is used to compensate the airplane pitch, roll and forward motion while the stabilization platform is used to dampen the airplane vibrations and to compensate the airplane yaw. The IMC mirror is controlled by the navigation module which receives and uses the information from the video tracker and the GPS/INS unit which enables ortho-rectification and geo-referencing of the collected data. The *Hyper-Cam LW* instrument offers uncommon flexibility in adjusting its spatial, spectral and temporal parameters. This flexibility proves to be invaluable for airborne applications where the flight parameters impose severe restrictions on spectrometer operation.

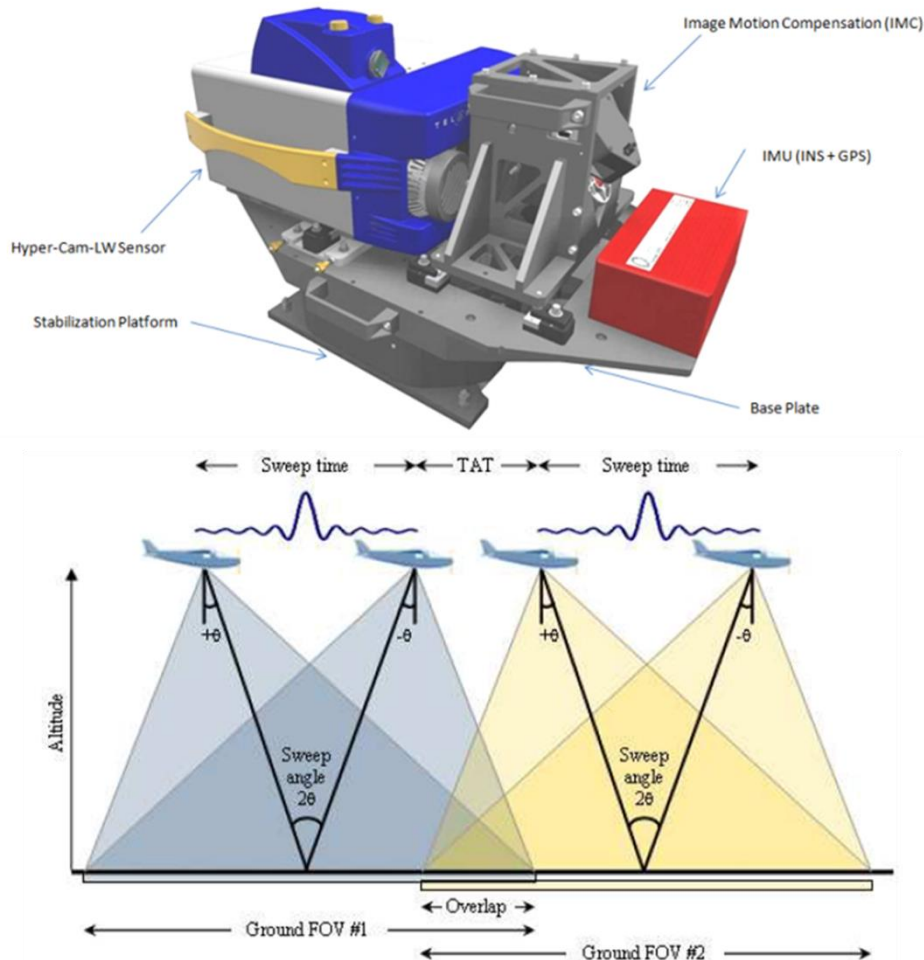


Fig. II-2: *Hyper-Cam LW* airborne assembly (top) and acquisition scheme (bottom): The IMC system is servo controlled to ensure the sensor is staring at a fixed scene during the acquisition of the hyperspectral image.

### 3 Measurement Procedures

To illustrate the capabilities of the system, measurements were done in the laboratory using heated rock and mineral samples. In this way it was possible to avoid poor outside weather conditions and to ensure stable conditions during measurements.

#### 3.1 Instrument Preparation and Settings

To setup the system for measurements, the *Hyper-Cam LW* was mounted on its tripod and the connections were plugged for CameraLink, Firewire (IEEE1394), RJ45 Ethernet and power. The start-up sequence consists of switching on the sensor, waiting for the internal diagnostics, launching the internal software suite Reveal Pro and waiting for the focal plane arrays (FPA) to cool down to 120 K which usually takes less than two minutes.

#### 3.2 Sample Preparation

The primary sample used in this study, *i.e.*, for testing the repeatability and the emissivity retrieval and for inspecting spatial emissivity features was a sandstone rock sample from the Lower Trias (Buntsandstein or Bunter Sandstone). The emissivity retrieval was repeated with quartz and calcite crystals. To obtain a high contrast between the sample and the surroundings in the laboratory, the sample was heated up to about 30 K above ambient temperature using an oven. The exact sample temperature was measured with a contact thermometer. The sample was placed at 3 m distance from the sensor so that the measured surface was perpendicular to the optical axis of the camera.

#### 3.3 Instrument Calibration

The instrument's spectral response is dependent on several factors such as detector responsivity, coatings, channel settings and integration time. A radiometric calibration is needed to acquire calibrated spectra in units of radiance (Hook and Kahle, 1996). Assuming linearity of FTIR spectrometers, the spectral response and the non-uniformities are determined for every pixel and the non-uniformities are eliminated during the calibration process using a 2-point complex radiometric calibration. For calibration, images of hot and cold blackbodies are acquired. The blackbodies' temperature can be controlled very accurately (<0.03 K stability) from ambient -15 K to ambient +75 K and should be chosen so that blackbodies are framing the scene's emitted radiation.

In this experiment, cold and hot blackbody temperatures were set to 15 °C and 65 °C, respectively, and the ambient temperature was 22 °C. Knowing the blackbodies' temperature as well as their exact spectral emissivity values, their spectral radiance was determined using the Planck's function. Starting from these two blackbody frames, a gain and offset function was calculated for every pixel which was then applied to the scene's raw spectra resulting in calibrated radiance spectra (Fig. II-3).

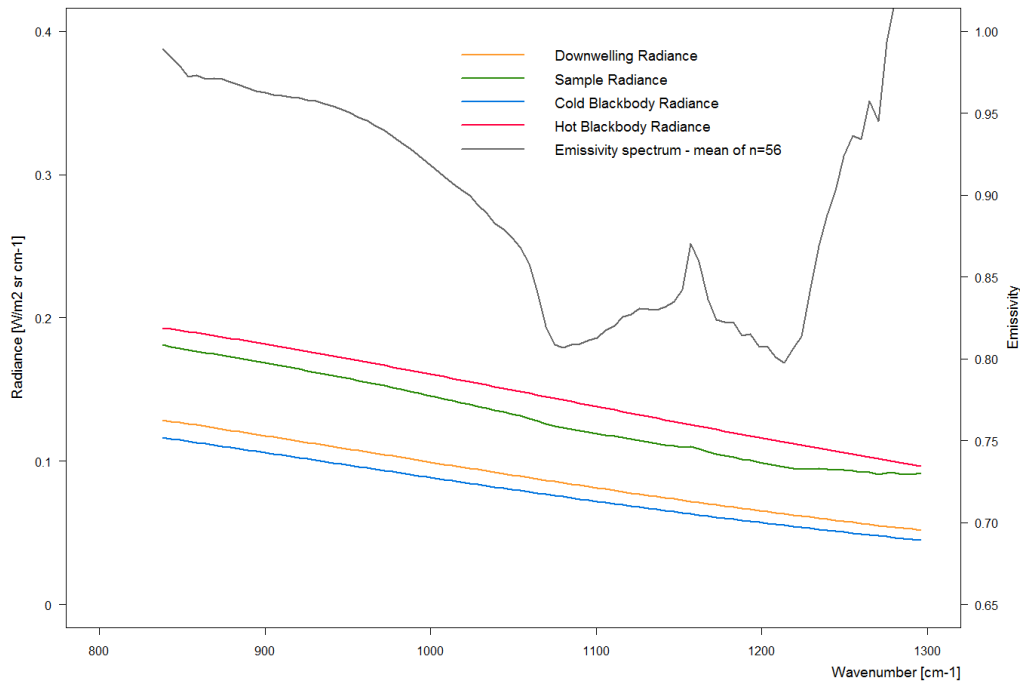


Fig. II-3: Measurement sequence of sample (sandstone), cold blackbody, hot blackbody and downwelling radiation and the derived sample emissivity spectrum. The lines shown represent the mean of 56 single measurements.

### 3.4 Background Radiation

Reflected or emitted radiance from background objects, *i.e.*, the walls and ceiling in the laboratory significantly contribute to the target measurement (Korb *et al.*, 1996). The background radiation (downwelling radiance) was measured immediately following the sample measurement by collecting the radiance of a diffuse reflective aluminum plate. The aluminum plate's exact temperature (ambient) was measured using a contact thermometer. The (unknown) emissivity of the aluminum plate was determined relative to an infragold target with known emissivity. This measurement was performed by a Bruker Vertex 70 FTIR spectrometer. The resulting overall emissivity value was 20% which is in good agreement with values found in literature.

### 3.5 Emissivity Calculation

Emissivity is a sample's efficiency to behave as a blackbody radiator and is scaled between 0 and 1. The calculation of a sample's emissivity requires knowledge of the radiance spectrum of a blackbody with the sample's temperature. However, accurate determination of the (unknown) sample temperature is often difficult and requires fitting the Planck equation to a measured radiance spectrum. Hyperspectral data with its continuous coverage of wavebands allows a good fit to the Planck radiance curve for spectral regions where emissivity is close to unity (Vaughan *et al.*, 2003).

Emissivity was assumed to have a certain fixed value over a defined wavelength region which allowed to iteratively fit a Planck radiance curve to the measured sample radiance spectrum. Emissivity was set to a value of 0.97 at the wavelength of the maximum brightness temperature following the approach by Kealy and Hook (1993). The fitting was performed over wavebands from 850 to 905 wave-numbers. An alternative approach would have been to set emissivity to a value of 1.0 in the 7.7–7.8  $\mu\text{m}$  region. In this region where silicate minerals typically have their Christiansen frequency, the emissivity is generally assumed constant and very close to 1.0 (Hook and Kahle, 1996). However, the first approach was preferred, as it produced more realistic emissivity spectra.

Blackbody radiance was simulated in unit wavenumber  $\sigma$ , commonly used in spectroscopy as (<http://www.spectralcalc.com/>):

$$L_{bb\sigma}(T) = 2hc^2\sigma^3 \frac{1}{e^{\frac{hc\sigma}{kT}} - 1} \text{Wm}^{-2}\text{sr}^{-1}(\text{cm}^{-1})^{-1}$$

where  $L_{bb\sigma}$  is the spectral radiance emitted by a blackbody at the absolute temperature  $T$  for wave-number  $\sigma$ ,  $h$  is the Planck constant,  $k$  is the Boltzmann constant, and  $c$  is the speed of light.

The blackbody radiance was then fitted to the measured sample radiance  $L_{sa\sigma}$  over the defined waveband region by adjusting  $T$  assuming the predefined emissivity  $\varepsilon_\sigma$ :

$$L_{sa\sigma} = \varepsilon_\sigma L_{bb\sigma}(T)$$

Finally, spectral emissivity  $\varepsilon_\sigma$  was calculated as:

$$\varepsilon_\sigma = \frac{L_{sa\sigma} - L_{dw\sigma}}{L_{bb\sigma}(T) - L_{dw\sigma}}$$

where  $L_{dw\sigma}$  is the downwelling radiance.  $L_{dw\sigma}$  was determined following an approach by Horton and co-workers (Horton *et al.*, 1998):

$$L_{dw\sigma} = \frac{L_{ref\sigma} - \varepsilon_{ref\sigma} \cdot L_{BB\sigma,T}}{1 - \varepsilon_{ref\sigma}}$$

where  $L_{ref\sigma}$  = measured radiance from reference panel (aluminum or infragold),  $\varepsilon_{ref\sigma}$  = spectral emissivity of reference panel,  $L_{BB\sigma,T}$  = blackbody radiance at temperature  $T$  of reference panel.

### 3.6 Testing Repeatability

For testing repeatability of data measured with the *Hyper-Cam LW* replicate measurements of the same sample material were performed under laboratory conditions. An experimental setup was chosen to allow acquiring multiple data cubes in a short time interval. To have a limited cooling effect on the recorded spectra, small image subsets ( $64 \times 20$  pixels) were acquired at a spectral resolution of  $6.2 \text{ cm}^{-1}$ . The sandstone sample was placed at a distance of three meters from the sensor. The sandstone sample was uniformly heated up to  $60 \text{ }^\circ\text{C}$  and 20 frames were captured within 30 s. During this short time interval the temperature of the sample decreased less than 0.5 K as measured with a contact thermometer. This image acquisition was repeated thrice so that altogether 58 frames were measured (two frames were removed). Due to the direct dependence of the radiance spectra on the sample temperature; emissivity spectra (temperature independent) were derived and considered for further investigation. Downwelling radiation was corrected for by measuring a diffuse reflecting aluminum plate.

In a user defined region of interest, the radiance spectra were isolated for every pixel and the mean emissivity spectrum was derived. Using the  $n = 58$  emissivity spectra, for every single wavenumber the mean value  $\bar{x}$  and standard deviation  $s$  were computed and the confidence interval was calculated as  $\bar{x} \pm s(t/\sqrt{n})$ , where  $t$  is a critical value determined from the  $t_{n-1}$  distribution.

### 3.7 Comparison with Reference Spectra

Derived emissivity spectra were compared with reference spectra. The same rock and mineral samples were measured at the spectrometry laboratory of University of Twente (ITC) using a laboratory device (Bruker Vertex 70 FTIR spectrometer) following the procedures described in (Hecker *et al.*, 2011). The spectra were measured in directional hemispherical reflectance. Assuming opaque properties of the rock samples, the emissivity was obtained by using Kirchhoff's Law ( $\epsilon = 1 - \rho$ ) which previously had been verified by both laboratory and field measurements (Korb *et al.*, 1996; Salisbury *et al.*, 1994). In addition, sandstone emissivity spectra from a spectral library collected by John Hopkins University were used for a plausibility check.

## 4 Results and Discussion

### 4.1 Repeatability

To test the repeatability of the system, replicate measurements of the sandstone sample were analyzed. A plot of the mean emissivity spectrum and the standard deviation of 58 single measurements (Fig. II-4) indicate good repeatability over the three measurement cycles with standard deviations less than 0.01 and variation coefficients of up to 1.25 %.

Hecker *et al.* (2011) performed a repeatability test for absolute measurements of directional-hemispherical reflectance (DHR) of quartz sand over 2 weeks using a Bruker Vertex 70 FTIR spectrometer. They obtained standard deviations in the range of 0.001 to 0.007 for most wavelengths which corresponds, with a mean DHR value of 0.4 at 9  $\mu\text{m}$ , to variation coefficients of 0.25 % – 1.75 %. In comparison to these values, a variation coefficient of up to 1.25 % obtained with the *Hyper-Cam LW* seems to be acceptable.

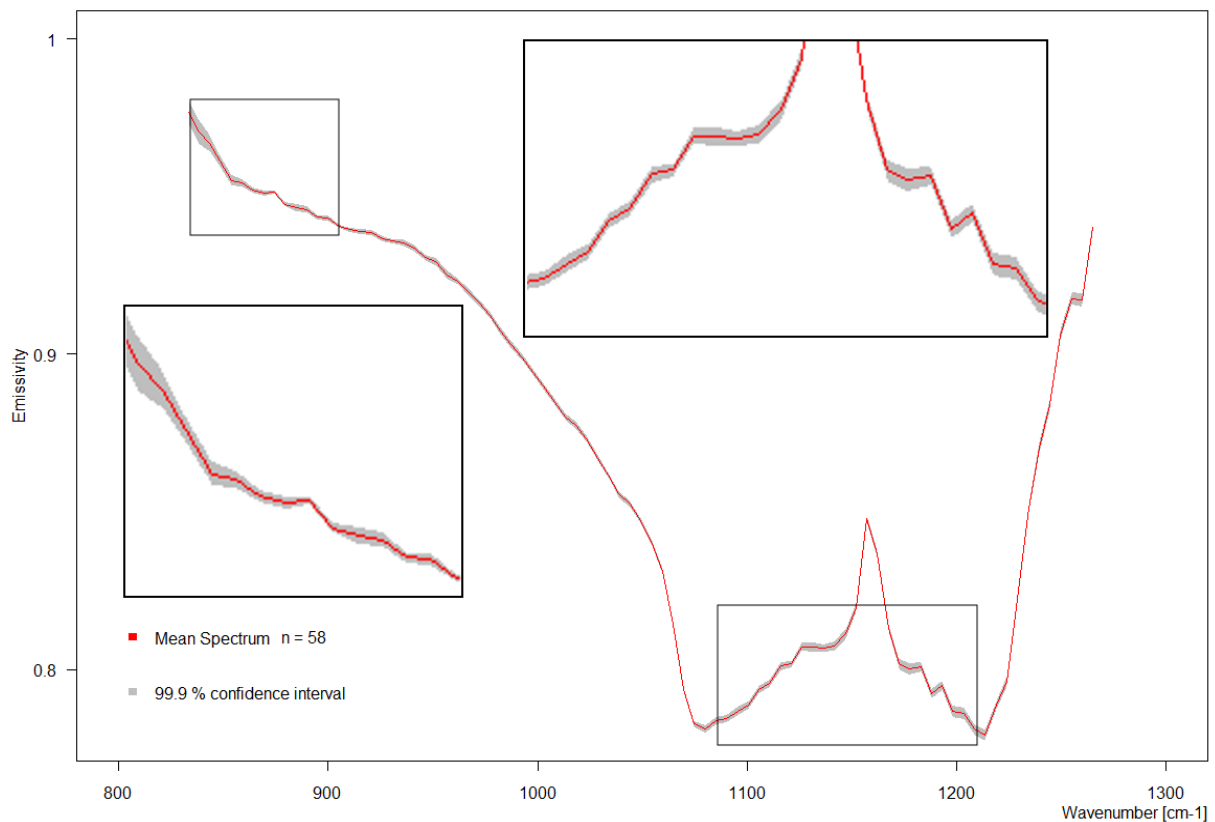


Fig. II-4: Demonstration of repeatability: The red line is an average of 56 single measurements and the grey band indicates the 99.9 % confidence interval of the mean at each wavenumber.



## 4.2 Comparison of Emissivity Spectra with Reference Spectra

The comparison of the Bunter Sandstone emissivity spectrum derived with the *Hyper-Cam LW* and the Bruker Vertex 70 (Fig. II-5) shows a relatively good agreement. Both spectra show the main quartz doublet around  $1,175\text{ cm}^{-1}$  with the characteristic maximum and the minima around  $1,080\text{ cm}^{-1}$  and around  $1,220\text{ cm}^{-1}$ . The spectra agree particularly well for the spectral regions left and right of the Quartz doublet. However, for wavenumbers between the two minima larger discrepancies between *Hyper-Cam LW* and Bruker spectra exist. One explanation for this difference is that different parts of the sandstone sample were observed during the two measurement setups. Besides, the comparison of the Bunter Sandstone emissivity spectrum derived with the *Hyper-Cam LW* with two sandstone spectra (Arkosic Sandstone and Ferruginous Sandstone) of the spectral library of John Hopkins University indicated a general agreement in the shape of the curves (not shown). Also the other *Hyper-Cam LW* emissivity spectra obtained for calcite and quartz (Fig. II-6) compare relatively well to the Bruker reference spectra with respect to their main spectral features. In comparison to previously published spectra, *e.g.*, (Hook and Kahle, 1996), the quartz spectrum reveals similarities in the general shape of the spectrum, but also differences in the magnitude of emissivity, *i.e.*, at  $1,220\text{ cm}^{-1}$   $\varepsilon\sim 0.80$  in this study and  $\varepsilon\sim 0.60$  in (Hook and Kahle, 1996). These enormous differences are likely to be caused by differences in surface roughness. For instance, differences in emissivity of comparable magnitude (*e.g.*,  $\varepsilon$ -differences of up to 0.25) were also found by (Balick *et al.*, 2009) for matte and rough mineral samples of identical mineral composition.

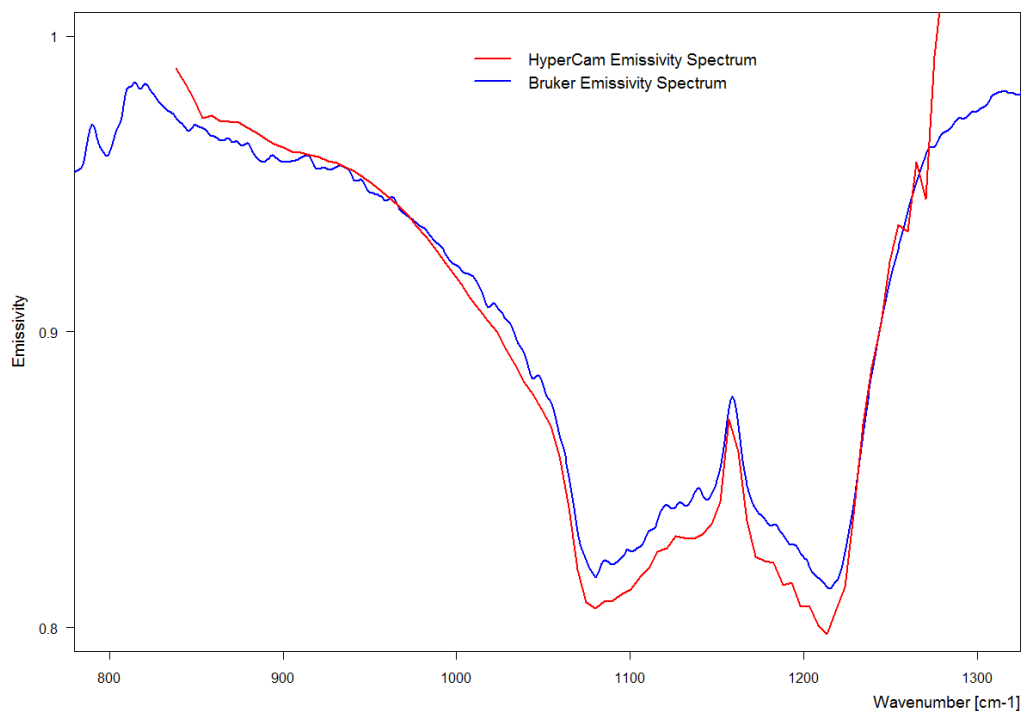


Fig. II-5: Emissivity spectra of the Bunter Sandstone sample derived from the *Hyper-Cam LW* (red) and from the Bruker (blue).

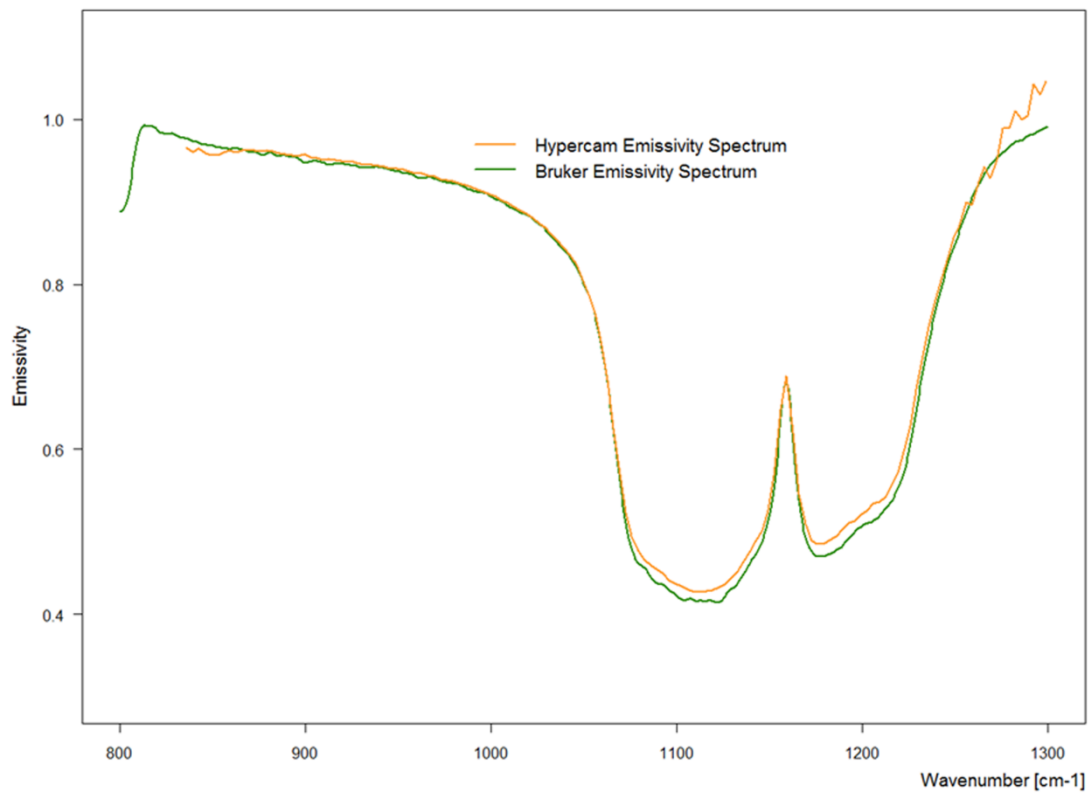


Fig. II-6: Emissivity spectra of Calcite (top), and Quartz (bottom) derived from *Hyper-Cam LW* and Bruker spectrometers.

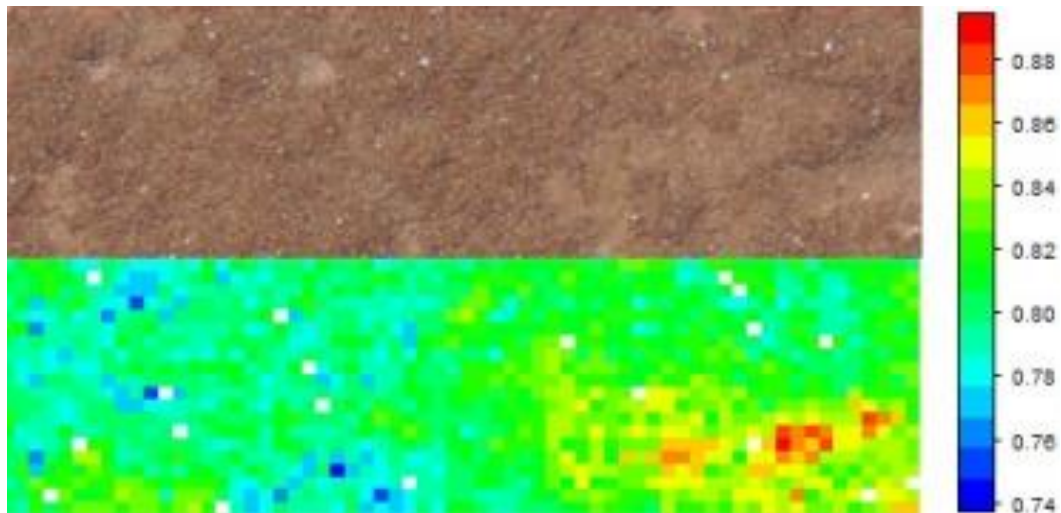


Fig. II-7: Surface of the sandstone sample (top) and derived emissivity values at 1,095  $\text{cm}^{-1}$  (bottom). White pixels are detector failures which are marked as bad pixels by the Reveal Pro software.

### 4.3 Spatial Variability of Emissivity

When looking at the spatial emissivity patterns (Fig. II-7), there is a clear variation of emissivity over the sandstone surface which is not obvious from a visual inspection of the rock sample. Within the dominant matrix of emissivity values of 0.81–0.83 (shown in green colour) there are marked areas with much smaller values of around 0.76–0.78 (shown in blue) and larger values of around 0.86–0.88 (shown in red). The observed spectral emissivity variations within the rock sample may be attributed to roughness, surface geometry, and compositional variation (Balick *et al.*, 2009).

## 5 Conclusions and Outlook

The first tests with the new Hyperspectral Thermal Infrared Imaging Instrument suggest that the system is capable of measuring spectral emissivity and its spatial variation over natural surfaces with good accuracy. Current tests were performed in the laboratory with heated rock samples and will be repeated outside under clear sky conditions with samples at ambient temperature.

The similarity between the emissivity spectra obtained by the *Hyper-Cam LW* and reference spectra (Bruker Vertex 70 and JHU spectral library) appears close enough for mapping such minerals from airborne hyperspectral (or spaceborne multispectral) TIR measurements (such as ASTER Level 2 surface emissivity products) based on the shapes of the laboratory reference spectra, for instance using respective band ratio techniques (Rockwell and Hofstra, 2008).

The final implementation of the airborne platform will facilitate generating accurate maps of land surface emissivity and land surface temperature at very high spatial resolution which in turn will provide new opportunities in environmental remote sensing such as monitoring natural and urban environments, volatile organic compounds, detection of vegetation stress, evapotranspiration rates and energy fluxes, mineral mapping, and bio-diversity.

Airborne observations require taking atmospheric effects and instrument noise into consideration (Jiménez-Muñoz *et al.*, 2012). Since atmospheric absorption (mainly by H<sub>2</sub>O and CO<sub>2</sub>) is the dominant process in the TIR, while dispersion processes are negligible, at a first glance atmospheric correction in the TIR seems to be simpler than for shortwave radiation. However, it has to be noted that in addition to the surface, the atmosphere also emits radiation towards the sensor. This requires solving the equation of radiative transfer for the TIR region, which makes the interpretation of airborne hyperspectral TIR data more ambiguous than ground based measurements.

Due to the complementary nature of the reflective (VSWIR) and emissive (TIR) spectral regions a synergistic use of airborne data from both domains bears great potential. This might significantly improve our understanding of biochemical and physical land surface properties. Specifically, VSWIR imaging spectrometers can discriminate surface materials and TIR data acquisitions can help to identify thermal characteristics for different material and land cover types. For instance, combining emissivity spectra with reflectance spectra in a mixing model would improve discriminating soils from impervious surfaces (Roberts *et al.*, 2012).

## Acknowledgments

The setup of the instrument facility was supported by the European Fund for Economic and Regional Development (AIRSPEC Project, grant 2008-01-15-20). Financial support by the Fonds National de la Recherche Luxembourg (FNR) for the HYPERFOREST Project (Advanced airborne hyperspectral remote sensing to support forest management, research grant INTER/STEREO/09/01) is greatly acknowledged. We wish to thank Chris Hecker (ITC, University of Twente, The Netherlands) for his assistance in measuring reference spectra at ITC spectral laboratory facilities.



# Chapter III

## Water Stress Detection in Potato Plants using Leaf Temperature, Emissivity, and Reflectance

*Int. J. Appl. Earth Obs. Geoinf.* 53,

*December 2016, 27 – 39.*

DOI: 10.1016/j.jag.2016.08.004

Max Gerhards, Gilles Rock, Martin Schlerf and Thomas Udelhoven

© 2016 Elsevier B.V. All rights reserved.

The following manuscript is a copy of the final version of the accepted manuscript. The paper has been through peer review, but it has not been subject to copy-editing, proofreading and formatting added by the publisher. The contribution of Max Gerhards to this scientific publication was the development and implementation of the experiment, as well as the processing, analysis and interpretation of the data. Furthermore, Max Gerhards took the lead in writing and editing the manuscript.

The version-of-record can be accessed at:

<http://www.sciencedirect.com/science/article/pii/S0303243416301349>

## Abstract

Water stress is one of the most critical abiotic stressors limiting crop development. The main imaging and non-imaging remote sensing based techniques for the detection of plant stress (water stress and other types of stress) are thermography, visible (VIS), near- and shortwave infrared (NIR/SWIR) reflectance, and fluorescence. Just very recently, in addition to broadband thermography, narrowband (hyperspectral) thermal imaging has become available, which even facilitates the retrieval of spectral emissivity as an additional measure of plant stress. It is, however, still unclear at what stage plant stress is detectable with the various techniques.

During summer 2014 a water treatment experiment was run on 60 potato plants (*Solanum tuberosum* L. *Cilena*) with one half of the plants watered and the other half stressed. Crop response was measured using broadband and hyperspectral thermal cameras and a VNIR/SWIR spectrometer. Stomatal conductance was measured using a leaf porometer. Various measures and indices were computed and analysed for their sensitivity towards water stress (Crop Water Stress Index (CWSI), Moisture Stress Index (MSI), Photochemical Reflectance Index (PRI), and spectral emissivity, amongst others).

The results show that water stress as measured through stomatal conductance started on day 2 after watering was stopped. The fastest reacting, *i.e.*, starting on day 7, indices were temperature based measures (*e.g.*, CWSI) and NIR/SWIR reflectance based indices related to plant water content (*e.g.*, MSI). Spectral emissivity reacted equally fast. Contrarily, visual indices (*e.g.*, PRI) either did not respond at all or responded in an inconsistent manner.

This experiment shows that pre-visual water stress detection is feasible using indices depicting leaf temperature, leaf water content and spectral emissivity.

## 1 Introduction

Today, agriculture consumes about 80-90 % of fresh water worldwide (Gonzalez-Dugo *et al.*, 2010; Morison *et al.*, 2008). Water-deficit stress, usually shortened to water- or drought-stress, is a phenotypic characteristic that exhibits dehydration in the plant due to the lack of available water required to keep cell concentrations at an acceptable and healthy level (Hopkins and Hüner, 2009). Water stress is one of the most critical abiotic stressors limiting plant growth, crop yield and quality concerning food production (Hsiao *et al.*, 1976).

As a plant physiological reference, stomatal conductance measured by a porometer is the most sensitive reference measurement of plant water stress induced by water deficit (Jones, 2004b). A porometer measures the vapour concentrations at two different locations within a defined path using humidity sensors from which leaf transpiration is calculated. Knowing the leaf transpiration, stomatal conductance is directly calculated (Percy *et al.*, 1989). However, the direct measure of leaf transpiration using porometry involves contact with the leaves and intervenes in the interactions between the leaf and the surrounding environment. Further, the method is labour-intensive, time-consuming, and only provides point measurements (Costa *et al.*, 2013).

Imaging techniques open the possibility of fast and non-destructive spatio-temporal monitoring of many physiological and structural crop characteristics. The main remote sensing techniques for the detection of plant stress (water stress and other types of stress) are thermal imaging (thermography; 8 – 14  $\mu\text{m}$ ), visible, near- and shortwave infrared reflectance (VNIR/SWIR; 0.4 – 2.5  $\mu\text{m}$ ), and fluorescence (*e.g.*, 0.76  $\mu\text{m}$ ). Thermal imaging takes advantage of the leaf energy balance equation, *i.e.* leaf temperature varies with transpiration from leaves (Jones, 1999a; Tanner, 1963). The underlying concept is that a decrease in plant water status leads to a reduction in leaf transpiration as a result of active regulation of stomatal aperture, consequently increasing the leaf temperature due to a reduced evaporative cooling (Inoue *et al.*, 1990). Conversely, a well-watered plant will have a lower temperature in comparison to the ambient air temperature. The stomatal regulation of a plant also highly depends on the actual meteorological factors, such as solar radiation, wind speed, ambient air temperature and vapour pressure deficit (VPD). VPD is the difference between the actual amount of water in the air and the maximum amount of water vapour in the air for a given temperature and therefore gives the capability of leaf transpiration. In general, the higher the VPD the higher the leaf transpiration rate for a healthy plant. In summary, leaf and canopy temperatures are a function of stomatal conductance and meteorological variables (Jones, 2004a). Stomatal closing is one of the first responses to water deficit and thus gives thermal imaging the possibility for detecting water stress pre-visual, *i.e.* before the change of leaf colour (Costa *et al.*, 2013; Jackson *et al.*, 1981; Jones, 2004a; Maes and Steppe, 2012).



The main problem of this temperature-based approach is constituted by the fact that the direct use of leaf or canopy temperature values alone cannot be an absolute estimator of the physiological status of crop plants (Inoue *et al.*, 1990) since leaf temperatures measured under natural field conditions are very sensitive to highly fluctuating environmental factors. Thus, a variety of approaches were developed in the past to calibrate or normalize leaf temperature to estimate plant water stress more quantitatively. First corrections were done by the difference between leaf and air temperature (Idso *et al.*, 1977a). The popular Crop Water Stress Index (CWSI) (Jackson *et al.*, 1981) not only corrects for air temperature but rather for all meteorological variables. In particular, the use of dry and wet artificial reference surfaces, which neglect additional meteorological data to describe the current environmental conditions, improved the usability of CWSI for thermal remote sensing (Jones, 1999a).

Up to now, most studies regarding temperature based plant water stress detection used handheld broadband infrared cameras (Grant *et al.*, 2006; Jones *et al.*, 2009b). The temperature retrieval using these 1 channel camera systems underlies the assumption of a constant emissivity (*e.g.*,  $\varepsilon=0.97$  for vegetation), which in nature does not exist (Ullah *et al.*, 2012b). Thus, neglecting the spectral emissivity of the leaves themselves limits the accuracy of temperature estimation. For example, an error in the assumed emissivity of 1 % results in absolute temperature errors of about 1K (Jones, 2004a). Thermal hyperspectral imaging systems such as Telops *Hyper-Cam LW*, Itres TASI-600, Specim AisaOWL have recently become available. The great advantage of these devices is the ability to measure the emitted radiance in many narrow bands, which compared to broadband thermal cameras allows a very stable temperature emissivity separation (TES) and very accurate temperature retrievals (Schlerf *et al.*, 2012).

Besides temperature, these hyperspectral thermal infrared (TIR) imagers also have the ability to derive spectral emissivity by using a solid TES. Emissivity is defined as the ratio of radiative energy from the surface of an object of interest to the radiation from a blackbody following Planck's law depending on the wavelength at the same surface temperature. Until recently, emissivity spectra have not been exploited in vegetation studies for the following reasons: (i) low and complex spectral emissivity variations originate from plant physiological and biochemical processes as well as from plant structural effects; (ii) low signal-to-noise ratio as well as low spatial and spectral resolution of airborne or satellite remote sensing TIR sensors fail to detect minor variations in plants' TIR spectral fingerprint; (iii) to retrieve exact emissivity spectra accurate atmospheric correction and temperature emissivity separation (TES) methods are needed. Thus, only few authors studied plant properties in TIR mainly focusing on species discrimination (*e.g.*, Ribeiro da Luz and Crowley, 2010, 2007; Salisbury, 1986; Ullah *et al.*, 2012b). Concerning plant stresses in the TIR, just very recently Buddenbaum *et al.* (Buddenbaum *et al.*, 2015) and Buitrago *et al.* (2016) demonstrated the ability of stress detection using the spectral emissivity. Buitrago *et al.* (2016) revealed the detection of water and cold stress at two different points in time based on the spectral emissivity of both European beech (*Fagus sylvatica*) and rhododendron

(*Rhododendron cf. catawbiense*) leaves. They used a directional hemispherical reflectance (DHR) Bruker Vertex 70 FTIR laboratory spectrometer, equipped with an integrating sphere (Hecker *et al.*, 2011). In comparison to passive emissive measurement devices, this non-imaging method is destructive, very time-consuming and limited to single leaves. On the contrary, Buddenbaum *et al.* (Buddenbaum *et al.*, 2015) were able to clearly differentiate water stressed and non-stressed European beeches (*Fagus sylvatica*) based on spectral emissivity using a passive emissive imaging spectrometer, the Telops *Hyper-Cam LW*. No conclusions were drawn at which stage water stress can be detected using spectral emissivity in comparison to other stress sensitive methods (*e.g.*, plant temperature, stomatal conductance), since this study was conducted during one diurnal course. Nevertheless, spectral emissivity facilitates new possibilities to detect water stress in contrast to the hyperspectral VNIR/SWIR spectral domain. Spectral radiation in the VNIR/SWIR is dominated by overtones and combination modes of fundamental vibrations, which originate from the interactions of solar radiation and leaf contents (*e.g.*, leaf pigments). In comparison, spectral emissivity as the capability of emitting thermal radiation has large potential for the quantification of vegetation stresses, since it may be directly linked to leaf physiology and biochemistry (Ribeiro da Luz and Crowley, 2007).

Water stress not only changes leaf temperature and spectral emissivity but also leaf and canopy water content, pigment content, and structure. These leaf and canopy parameters are driving leaf and canopy reflectance in the solar reflective spectral range of the electromagnetic spectrum (VNIR/SWIR). Especially hyperspectral data opened the opportunity for the development of narrowband vegetation indices (VIs), which simplify the complex vegetation reflectance signatures and are indirectly related to plant physiological and structural parameters (Govender *et al.*, 2009). Numerous studies make use of (VIs) for water stress detection such as the Water Index (WI, Peñuelas *et al.* (1997)), the Normalized Difference Vegetation Index (NDVI, Rouse *et al.* (1974)), and the Photochemical Reflectance Index (PRI, Gamon *et al.* (1992)). Suárez *et al.* (2009) observed robust relationships of PRI against canopy temperatures for various crops (*e.g.*,  $R^2=0.72$  for maize). Furthermore, Panigada *et al.* (2014) observed PRI as a more sensitive indicator for early plant water stress, when only plant physiological parameters are affected, than traditional VIs (*e.g.*, NDVI). Additionally, VNIR fluorescence imaging is a good indirect estimator of water stress (Lang *et al.*, 1996).

From the above discussion we derived the following aims for this study: (i) to evaluate in a controlled experiment the ability of temperature based indices and VNIR/SWIR reflectance based indices for detecting water stress in comparison to plant physiological measurements, (ii) to compare hyperspectral and broadband imaging systems for deriving temperatures as a basis for water stress detection and (iii) to examine the abilities of detecting water stress using the spectral emissivity of plant leaves.

## 2 Materials and Methods

### 2.1 Experiment

In the period from July, 16<sup>th</sup> (0 days after stress) to 25<sup>th</sup> (9 days after stress) 2014, an outdoor water stress experiment on potato plants (*Solanum tuberosum L. Cilena*) was conducted under controlled conditions next to the greenhouse facilities of the Geobotany Department of Trier University (49°44'49.2"N, 6°41'02.4"E). The start of the experiment was set at the end of the flowering and the beginning of tuber initiation, when water consumption is highest (Dalla Costa *et al.*, 1997). Potato tubers were sown in single pots (n=60) with a substrate mixture of peat moss and sand (1:3, vol:vol). After the first day of measurement (16<sup>th</sup> July 2014) two treatments (control and treatment with n=30 each), non- and fully-irrigated were applied. Plants were stored under a roof to prevent any external water supply (Fig. III-1 (b)). Before measuring, plants were moved outside to adapt to sunny conditions for at least half an hour. All data of the study were recorded during midday (11:00–15:30 CEST) under clear sky conditions. Bad weather conditions during the experiment prevented continuous measurements on a daily basis, which reduces the dataset to six dates (0, 1, 2, 7, 8 and 9 days after stress initiation). Furthermore, the number of observations (n) (Table III-1) was mainly reduced due to failures of measurement devices and rapidly changing weather conditions. At the end of the experiment, tubers were harvested and the yields obtained for stressed and non-stressed plants were compared.

Table III-1: Number of observations per day after stress initiation.

<b>Days after stress</b>	<b>0</b>	<b>1</b>	<b>2</b>	<b>7</b>	<b>8</b>	<b>9</b>
<i>Hyper-Cam LW</i> (emissivity)	59	59	58	56	60	60
<i>Hyper-Cam LW</i> (temperature)	37	58	57	36	56	58
Fluke	60	10	48	59	60	60
ASD (leaf scale)	59	59	56	56	54	29
ASD (canopy scale)	60	59	59	-	15	60
Porometer	9	12	12	11	12	-
Weather station	60	59	59	59	60	60

## 2.2 Meteorological Measurements

The meteorological variables air temperature ( $T_{\text{air}}$ ), air pressure, and relative humidity (RH), were measured at the study site using a portable automatic weather station (Vaisala WXT520) with a CR800 (Campbell scientific, Inc.) data logger. Measurements were recorded continuously at 10 sec intervals at 2 m above ground. Following the findings of Anderson (1936), VPD is a more sensitive indicator of water vapour condition than relative humidity (RH) and therefore describes the interaction of plants with the intervening atmosphere more precisely. VPD (kPa) was calculated using equation (II-1) (Struthers *et al.*, 2015):

$$VPD = e_s \times \frac{100 - RH}{100} \times 0.1 \quad (\text{III-1})$$

$$e_s = 6.11 \times \exp\left(\frac{L}{Rv} \left(\frac{1}{273} - \frac{1}{T}\right)\right)$$

where  $e_s$  is the saturation vapour pressure in mbar,  $L$  is the latent heat of vaporization ( $2.5 \times 10^6 \text{ J kg}^{-1}$ ),  $Rv$  is the gas constant for water vapour ( $461 \text{ J K}^{-1} \text{ kg}^{-1}$ ) and  $T$  is the actual air temperature (K). RH is the relative humidity (%).

## 2.3 Porometry

Plant physiological measurements of leaves, such as stomatal conductance ( $g_s$ ;  $\mu\text{mol m}^{-2} \text{ s}^{-1}$ ), leaf transpiration rate ( $E$ ;  $\text{mmol m}^{-2} \text{ s}^{-1}$ ) and photosynthetic rate ( $A$ ;  $\mu\text{mol m}^{-2} \text{ s}^{-1}$ ) were derived using a gas exchange porometer with a corresponding leaf chamber (LCi, ADC BioScientific Ltd., Hoddesdon, UK). Porometer measurements were carried out in the upper part of the canopy using only sunlit leaves at ambient illumination. Due to the self-calibration of the gas exchange system, the measurement takes approx. 10 min per leaf, limiting the number of observations to  $n=12$  plants per day. Measurements were taken automatically every 30 seconds. Leaves of the control and treatment group were measured alternately. To ensure that only measurements under clear sky conditions were taken into account, data points with a photosynthetically active radiation (PAR) greater than  $400 \mu\text{mol m}^{-2} \text{ cm}^{-1}$  were selected, which correspond well with the light saturation curve of potatoes (Pleijel *et al.*, 2007).

## 2.4 Thermal Infrared

### 2.4.1 Image Acquisition

Hyperspectral TIR data were recorded using a *Hyper-Cam LW* (Telops Inc., Québec, Canada), which consists of an FTIR (Fourier transformed infrared) spectrometer using a 320 x 256 pixel MCT (mercury cadmium telluride) focal plane array (FPA) detector with up to  $0.25\text{cm}^{-1}$  spectral resolution, corresponding to 5 nm at  $10\ \mu\text{m}$ , in the spectral range of 7.7 to  $11.5\ \mu\text{m}$  (Schlerf *et al.*, 2012). In simplified terms, this FTIR spectrometer works on the operating principles of a Michelson interferometer. It measures interferograms, which are translated into spectral radiances ( $\text{W m}^{-2}\ \text{sr}^{-1}\ \text{cm}^{-1}$ ) using real-time discrete-Fourier transform. Further, the camera system is provided with two internal blackbodies with a known emissivity ( $\epsilon \geq 0.99$ ). The imaging spectrometer was equipped with a wide-angle telescope and a  $45^\circ$  tilted gold-coated mirror, which allowed vertical view with a field of view (FOV) of 672 mm x 538 mm and a pixel size of 2.1 mm at 1.5 m distance. A spectral bandwidth of  $4\ \text{cm}^{-1}$  FWHM (Full Width at Half Maximum) corresponding to 40 nm at  $10\ \mu\text{m}$  was chosen in the spectral domain from 869 to  $1298\ \text{cm}^{-1}$  (7.7 –  $11.5\ \mu\text{m}$ ), resulting in 120 bands.

The broadband TIR images were taken by a Fluke TiR1 thermal imager (Fluke Inc., Everett, WA, USA), which has an uncooled microbolometer FPA of 160 x 120 pixel size and is sensitive in the spectral range of 7.5 to  $14\ \mu\text{m}$ . The emissivity coefficient is user selectable. Furthermore, the system is equipped with a co-registered 640 x 480 pixel visual camera, which facilitates a picture-in-picture image interpretation (Fluke Corporation, 2010).

Fig. III-1 shows the experimental setup. Hyperspectral images were taken from a tripod with a sensor target distance of about 1.5 m. The Fluke TiR1 was mounted 1.2 m on top of the *Hyper-Cam LW*, due to its smaller FOV and in order to co-register both thermal imaging systems. Further, a highly diffused Infragold standard (Labsphere Inc, North Sutton, USA) was arranged within each scene for downwelling radiance (DWR) collection. Moreover, dry and wet artificial reference surfaces, leaf-shaped and consisting of a green felt, were placed in each image to determine lowest and highest possible leaf transpiration rates under actual micro-meteorological conditions. To improve the signal-to-noise ratio (SNR) of the hyperspectral data, eight consecutive images were recorded per plant. One measurement cycle took approximately four minutes. All 60 canopies were measured synchronously with the *Hyper-Cam LW* and the Fluke TiR1 in a consistent order for each day of the experiment.



Fig. III-1: Experimental setup with *Hyper-Cam LW* on the tripod, Fluke TiR1, Lci leaf porometer, Infragold as well as dry and wet references targets (a), plant breeding and storage of the 60 potato plants under a roof construction (b), plants of the control (c) and treatment (d) group at day 9 after stress initiation.

#### 2.4.2 Temperature Retrieval

To compare the both TIR imaging systems, corresponding regions of interests (ROIs) were selected in each image pair (*Hyper-Cam LW* and Fluke). Only sunlit leaves as well as sunlit parts of the dry and wet references were selected. A single ROI of a plant contained approximately 300 pixels for the Fluke TiR1 and 800 pixels for the *Hyper-Cam LW*, due to its larger FOV. In an equal manner ROIs were drawn for the dry and wet references and the Infragold.

In order to avoid FOV-effects between the *Hyper-Cam LW* and the Fluke, three temperature retrievals were performed depending on their origin: (i) ‘spectral smoothness’ TES based on hyperspectral radiances (*Hyper-Cam LW*), (ii) broadband temperatures based on hyperspectral radiances spectrally resampled to broadband radiance (*Hyper-Cam LW* broadband) and (iii) broadband temperature based on Fluke brightness temperatures (Fluke).

First, surface temperatures were retrieved from the hyperspectral *Hyper-Cam LW* data. Therefore, the first step was to transfer the raw interferograms into spectral radiances ( $\text{W m}^{-2} \text{sr}^{-1} \text{cm}^{-1}$ ). This radiometric calibration, including a Fourier transformation, a two-point calibration based on the internal blackbodies with known temperature and emissivity ( $\epsilon \geq 0.99$ ), as well as a bad pixel correction, was performed by Telops Reveal Calibrate software. Next, the so called ‘spectral smoothness’ approach (Horton *et al.*, 1998) for temperature and emissivity separation (TES) was applied to retrieve surface temperatures from the spectral radiances. This state of the art TES approach allows for DWR correction and is most suited for outside measurements. The approach is only applicable for outside measurements under clear sky conditions and requires a short sensor-target distance to neglect distortions by the intervening atmosphere and to guarantee highly accurate surface temperature retrieval. It is based on the minimisation of isolated water vapour lines within the spectrum through changing the temperature. The temperature, which specified the smoothest spectrum, was chosen as surface temperature ( $T_s$ ). We used the water absorption line at  $1174.5 \text{ cm}^{-1}$  ( $8.51 \text{ }\mu\text{m}$ ).

Second, concerning the possible FOV-effects between the two imaging systems a spectral resampling was applied on the hyperspectral *Hyper-Cam LW* data. The resampling was done by summing up the spectral radiances per spectral band multiplied by the mean FWHM, resulting in a single spectral radiance over the spectral range from  $869$  to  $1298 \text{ cm}^{-1}$  ( $7.7 - 11.5 \text{ }\mu\text{m}$ ). Using a look up table (LUT) containing black body radiances with varying temperatures from  $220$  to  $350 \text{ K}$  at a resolution of  $0.001 \text{ K}$ , corresponding brightness temperatures were retrieved from the resampled spectral radiances. In comparison, the Fluke already provides images of brightness temperature. Lastly, surface temperatures of both broadband datasets (*Hyper-Cam LW* broadband and Fluke) were calculated using Stefan-Boltzmann law corrected for DWR and an adjusted emissivity for vegetation ( $\epsilon = 0.97$ ) (Maes and Steppe, 2012):

$$T_s = \sqrt[4]{\frac{T_{br}^4 - (1 - \epsilon) \times T_{bg}^4}{\epsilon}} \quad (\text{III-2}),$$

Where  $T_s$  is the surface temperature of the object of interest,  $T_{br}$  is the brightness temperature measured by the sensor, and  $(1 - \epsilon) \times T_{bg}^4$  is equivalent blackbody temperature for the DWR derived from the Infragold pixel within the specific image.

For further analysis we averaged the single temperatures per ROI, resulting in one temperature reading per potato plant and temperature retrieval approach.

### 2.4.3 Temperature Based Indices

Pure leaf temperatures can be used as a water stress detection estimator at one specific point in time, but are not suitable for water stress detection at several dates or during the course of the day, due to the interaction with rapidly changing meteorological conditions. To consider this fact, two temperature based indices were calculated: (i) the difference between leaf and air temperature ( $T_{\text{leaf}} - T_{\text{air}}$ ) following the approach of the Stress Degree Day (SDD) (Jackson *et al.*, 1977) and (ii) the prominent Crop Water Stress Index (CWSI) using artificial wet and dry reference surfaces (Jones, 1999a). CWSI was computed as follows:

$$CWSI = \frac{T_{\text{leaf}} - T_{\text{wet}}}{T_{\text{dry}} - T_{\text{wet}}} \quad (\text{III-3}),$$

where  $T_{\text{leaf}}$  is the leaf temperature,  $T_{\text{wet}}$  is the lower boundary for canopy temperature, assuming a leaf with stomata fully open and a potential transpiration rate of 100 %,  $T_{\text{dry}}$  is the upper boundary compared to a non-transpiring leaf with stomata completely closed. Therefore, the use of artificial wet and dry references considers actual environmental conditions within the same image and no additional meteorological measurements are needed. In comparison,  $T_{\text{leaf}} - T_{\text{air}}$  does correct for the fluctuation in  $T_{\text{air}}$ , but neglects the influence of VPD, solar radiation, or wind speed, which are considered in CWSI through the artificial reference surfaces.

### 2.4.4 Spectral Emissivity Retrieval

Knowing the DWR, which was measured using the Infragold standard, surface emissivity spectra are derived using equation (III-4):

$$\varepsilon_s(\sigma) = \frac{L_s(\sigma) - L_{DWR}(\sigma)}{L_{BB}(T_s, \sigma) - L_{DWR}(\sigma)} \quad (\text{III-4}),$$

where  $\sigma$  is the spectral wavenumber [ $\text{cm}^{-1}$ ],  $\varepsilon_s(\sigma)$  is the sample's spectral emissivity,  $L_{DWR}(\sigma)$  the downwelling radiance, and  $L_{BB}(T_s, \sigma)$  the blackbody radiance at the sample's temperature  $T_s$ . When using equation (III-4), mostly exact knowledge of the leaf kinetic temperature is required. This temperature ( $T_s$ ) was retrieved using the 'spectral smoothness' approach (Horton *et al.*, 1998).

Emissivity spectra were originated from the same ROIs as the *Hyper-Cam LW* temperatures. For further analysis we averaged the spectral emissivities per ROI, resulting in one spectral emissivity reading per potato plant at several days of measurement.



## 2.5 VNIR/SWIR

To compare the sensitivity of water stress detection using TIR with common vegetation indices in the 0.35 – 2.5  $\mu\text{m}$  spectral range, leaf as well as canopy spectra were measured using an ASD Fieldspec-3 spectrometer (ASD Inc., Boulder, CO, USA). The spectral resolution of the spectrometer is 3 nm at 0.7  $\mu\text{m}$  and 10 nm at 1.4  $\mu\text{m}$  and 2.1  $\mu\text{m}$ . Leaf reflectance measurements were taken with an ASD Plant Probe, consisting of a clamp with a constant light source and turnable dark or white (Labsphere Spectralon reference) background with spot size of 10 mm. This setup ensures non-destructive leaf contact measurements under controlled illumination conditions. Canopy reflectances were measured with an ASD pistol grip under clear sky conditions. To account for specific illumination conditions a Spectralon reference panel was used to adjust the sensitivity of the detector. White reference as well as grating drift corrections were performed on each spectrum following Dorigo *et al.* (2006). For the further analysis we took an average spectrum for each plant, which consists of three leaves or parts of the canopy per plant times three single spectra per leaf times 30 scan repetitions per spectrum for both canopy and leaf reflectance measurements. Only leaves or parts from the upper sunny canopy were selected.

To examine the ability of detecting plant water stress using the VNIR/SWIR spectral region, several narrowband vegetation indices (Table III-2) related to leaf physiology, structure and water content were calculated from the leaf and canopy reflectance spectra. The spectral bands centred at 0.531  $\mu\text{m}$  and 0.57  $\mu\text{m}$  were used to calculate Photochemical Reflectance Index (PRI) (Gamon *et al.*, 1992). As three simple ratio indices related to water content, we estimated the Water Index (WI) (Peñuelas *et al.*, 1993), the Leaf Water Index (LWI) (Seelig *et al.*, 2008) and the Moisture Stress Index (MSI) (Hunt Jr. and Rock, 1989), which are sensitive in the scope of the water absorption bands at 0.97  $\mu\text{m}$  and 1.45  $\mu\text{m}$  respectively. Additionally, the Normalized Difference Water Index (NDWI) (Gao, 1996) and the Normalized Difference Vegetation Index (NDVI) were tested (Rouse *et al.*, 1974).

Table III-2: Optical (VNIR/SWIR) narrow-band indices grouped by category: (1) xanthophyll pigments, (2) water content and (3) greenness. R is the reflectance at the ASD Fieldspec 3 wavelength in nm.

Category	Index	Equation	Reference
<i>Xanthophyll</i>	PRI	$PRI = (R_{570} - R_{531}) / (R_{570} + R_{531})$	Gamon <i>et al.</i> (1992)
<i>Greenness</i>	NDVI	$NDVI = (R_{800} - R_{670}) / (R_{800} + R_{670})$	Rouse <i>et al.</i> (1974)
<i>Water content</i>	WI	$WI = R_{900} / R_{970}$	Peñuelas <i>et al.</i> (1997)
	LWI	$LWI = R_{1300} / R_{1450}$	Seelig <i>et al.</i> (2008)
	MSI	$MSI = R_{1600} / R_{820}$	Hunt & Rock (1989)
	NDWI	$NDWI = (R_{857} - R_{1241}) / (R_{857} + R_{1241})$	Gao (1996)

## 2.6 Statistical Analysis

To compare the three temperature retrieval approaches, a repeated measures ANOVA was used over all days of measurements. A repeated measures ANOVA considers the fact that the same samples were measured at multiple dates (days after stress initiation) and thus highly correlated. Further, statistical evaluation was performed on a daily basis to compare the sensitivity of the plant physiological measurements, the leaf temperatures and temperature based indices of the three temperature retrieval approaches and the vegetation indices regarding water stress detection. Graphical analysis was done by boxplots. Mann-Whitney-U-tests at a level of significance of 5 % were performed in order to examine significant differences between the two water treatments for the single days of the study. Furthermore, Mann-Whitney-U-tests at a level of significance of 5 % were also applied per wavenumber to analyse emissivity regarding differences in the spectra of control and treatment plants. Additionally, the relationships between all investigated variables are represented in a correlogram of Spearman's rank correlation coefficient. All analyses were performed in RStudio.

## 3 Results and Discussion

### 3.1 Effect of Water Stress on Yield

Application of water stress on potato plants had a highly significant effect ( $p < 0.001^{***}$ ) on potato yield with average yields of 0.40 kg and 0.28 kg per plant for control and treatment, respectively (Fig. III-2). This confirms that during the experiment a severe water stress had been applied to the treated plants.

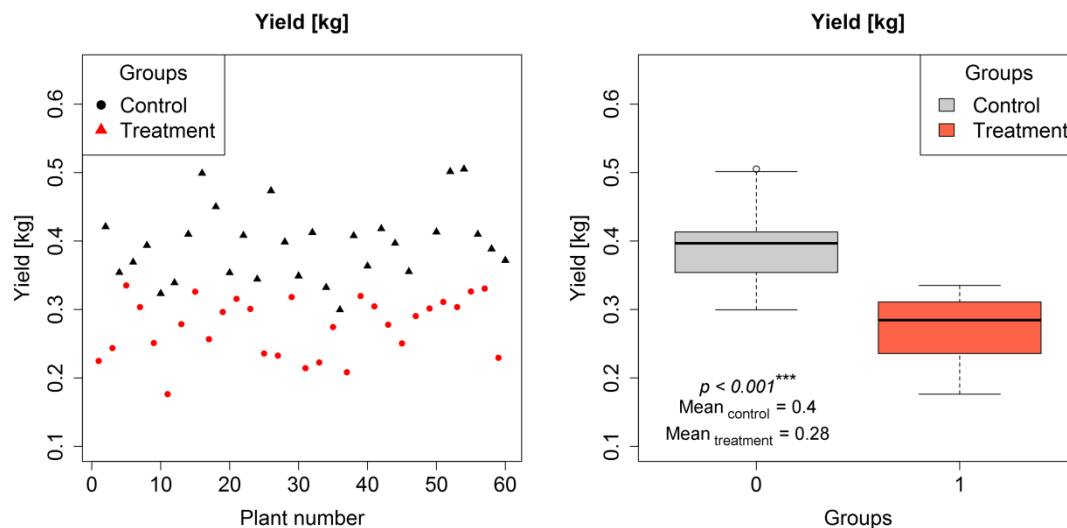


Fig. III-2: Potato yield of stressed (treatment) and non-stressed (control) plants (left), boxplots and mean values per group as well as corresponding p-value of a t-test (right).

### 3.2 Meteorological Measurements

$T_{\text{air}}$ , VPD and RH data were synchronised with the *Hyper-Cam LW* measurements for the six study dates.  $T_{\text{air}}$  and VPD showed a very similar course over time (Fig. III-3), increasing until day 2 and decreasing afterwards until the end of the experiment. Mean  $T_{\text{air}}$  ranged from minimum 23.8°C at day 9 to 29.9°C at day 2 after stress initiation with an average over all days of 26.4°C. On these same days VPD and RH minima (1.4 kPa and 40 %) and maxima (2.6 kPa and 53 %) also occurred.  $T_{\text{air}}$ , VPD and RH show strong correlations (Fig. III-4). The meteorological variables reveal weather conditions suitable for the conducted water stress experiment.

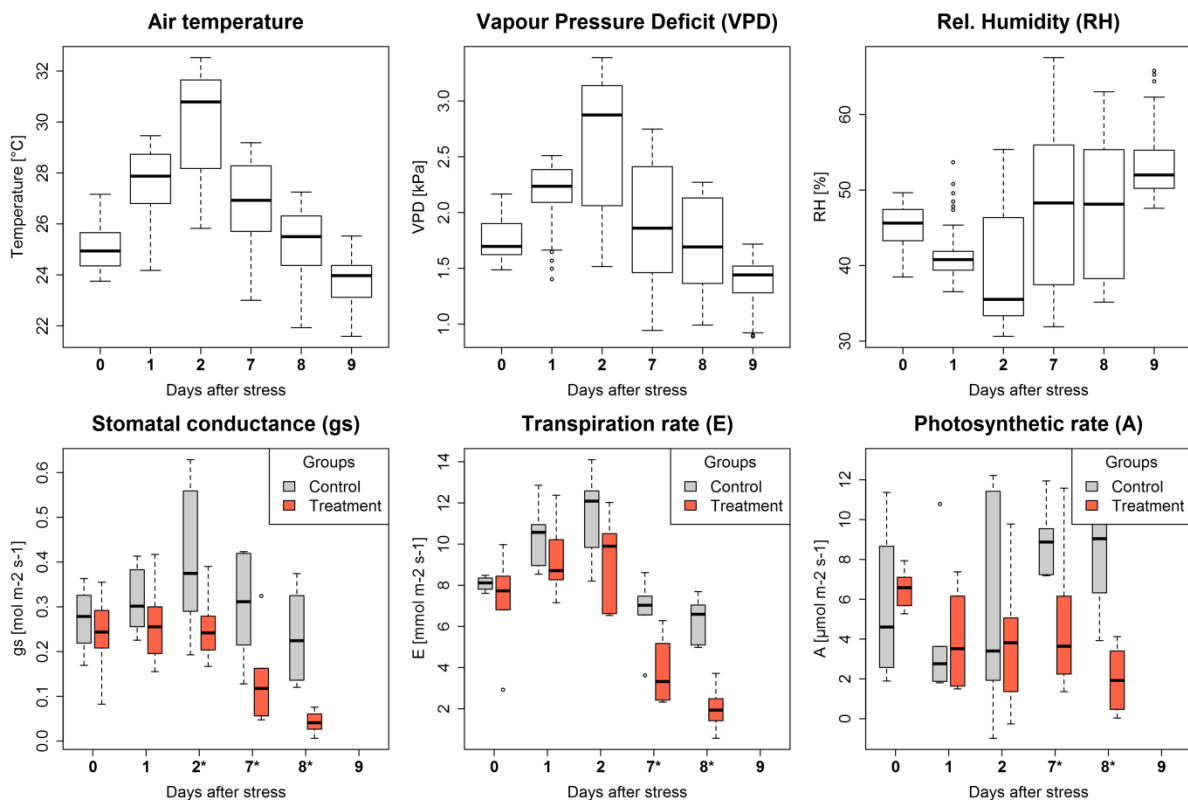


Fig. III-3: Boxplots per day after stress initiation of the meteorological (air temperature, VPD, rel. humidity) and plant physiological measurements (stomatal conductance, transpiration and photosynthetic rate). Asterisks (\*) indicating significant differences between control and treatment group at 5 % significance level.

### 3.3 Porometry

Stomatal conductance and transpiration rate show a high correlation ( $r = 0.77^{***}$ ) (Fig. 0-4), whereas the relation between stomatal conductance and photosynthetic rate is weaker ( $r = 0.45^{***}$ ). Boxplots of the three variables are shown in Fig. III-3, grouped by treatment and control. Control and treatment groups are significantly different in stomatal conductance starting from 2 days after stress initiation ( $p = 0.04^*$ ). The two groups are significantly different in transpiration rate and photosynthetic rate starting 7 days after stress (Table III-3). Therefore, stomatal conductance is most sensible for water stress detection using plant physiological data as well as in comparison with TIR and VNIR/SWIR data. Further, the dependency of stomatal conductance and transpiration rate from meteorological variables ( $T_{air}$  and VPD) is well described by the courses of the boxplots; highest values can be found at day 2 where VPD and  $T_{air}$  are also at maximum for this study.

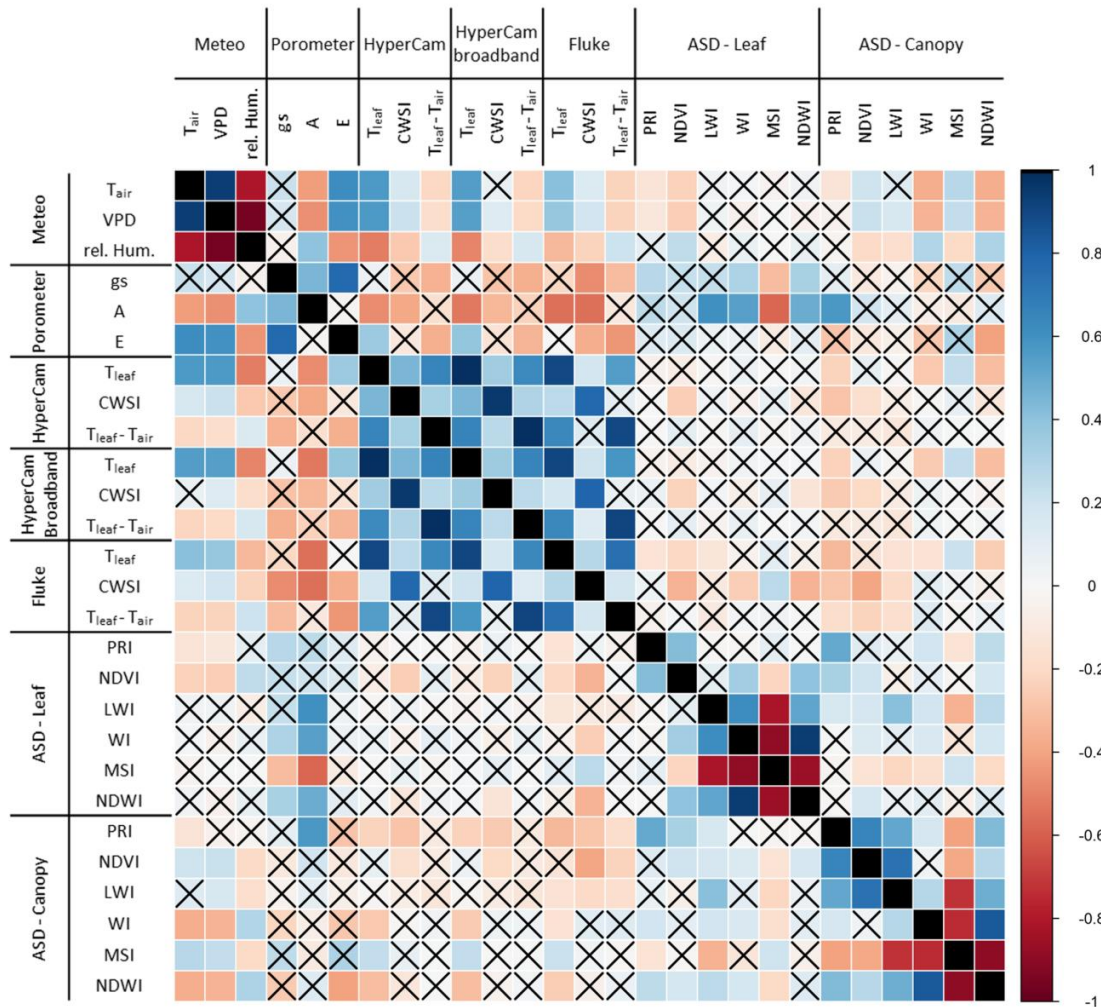


Fig. III-4: Correlogram of Spearman correlation of observed variables. Relationships which are not significant at 5 % significance level are marked by crosses. Main correlation clusters occur within meteorological variables, comparing the three retrieval approaches of temperature based indices (e.g., CWSI) as well as water content based indices (e.g., WI and MSI). Furthermore, strong individual correlation can be observed, e.g. between  $T_{leaf}$  and meteorological variables.

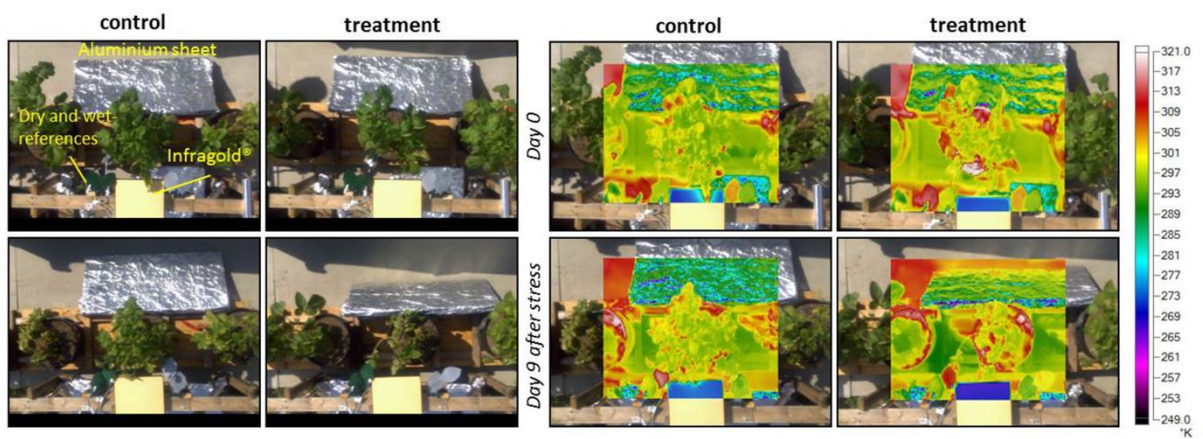


Fig. III-5: Example of visual images (left) and corresponding temperature maps (right) taken with Fluke thermal imager at first and last day of the experiment. At the overlaid temperature maps Infragold reflecting the cold sky (blue coloured) at the bottom image edges can be registered as well as obvious temperature differences between the wet (yellowish green coloured with approx. 295 K) and dry reference targets (red coloured with approx. 310 K). Aluminium sheet was used to reduce the DWR from neighbouring objects.

### 3.4 Thermal Infrared

Fig. III-5 shows an example of visual images and corresponding temperature images of plants from both water treatment groups at the start and end dates of the experiment. The raw temperatures are not comparable due to rapidly changing meteorological conditions. However, from the visual images, structural canopy as well as colour differences between the first and the last day of measurement can be clearly recognized for the treatment, whereas the control group is still healthy.

#### 3.4.1 Temperature Comparison

To examine if a hyperspectral thermal imaging system provides more precise results concerning water stress detection based on temperatures in comparison to a broadband system, a first comparison of the three temperature retrieval approaches was conducted. The total mean temperature values for all days are very similar and differentiate only up to 0.6 K for the Fluke TiR1 and the *Hyper-Cam LW* broadband temperatures and 0.2 K for the Fluke TiR1 and the *Hyper-Cam LW* (hyperspectral). The difference between the two *Hyper-Cam LW* approaches amounts to less than 0.4 K. This positive agreement is confirmed by a very high correlation coefficient  $r = 0.99^{***}$  for the two *Hyper-Cam LW* approaches (hyperspectral vs. broadband). Even the Fluke TiR1 is highly correlated with the *Hyper-Cam LW* and *Hyper-Cam LW* broadband temperatures with  $r = 0.89^{***}$  and  $r = 0.90^{***}$  respectively (Fig. III-4). Moreover, the repeated measures ANOVA confirmed these findings showing no significant differences between the three introduced temperature retrieval approaches ( $p = 0.12$ ).

Therefore, the choice of the TIR camera system had no significant effect on the retrieved temperatures. This finding implies that the assumption of  $\varepsilon = 0.97$  for the broadband approaches fits

excellently for the examined potato plants (*Solanum tuberosum L. Cilena*). A key advantage of a hyperspectral over a simple broadband imaging system is the possibility to correct for atmosphere effects. Not surprisingly, in this ground based experiment with a negligible amount of interfering atmosphere, this potential advantage played a lesser role. It is expected that hyperspectral systems outperform broadband systems in air- or spaceborne missions, where high spectral resolution is essential for an appropriate atmospheric correction and TES like ARTEMIS (Automatic Retrieval of Temperature and Emissivity using Spectral Smoothness; Borel, 2003).

### 3.4.2 Water Stress Detection

Regarding the two *Hyper-Cam LW* approaches, CWSI and  $T_{\text{leaf}} - T_{\text{air}}$  are also highly correlated with  $r = 0.96^{***}$  and  $r = 0.99^{***}$  respectively (Fig. III-4). The Fluke TiR1 shows also high correlations for the CWSI ( $r = 0.78^{***}$  and  $r = 0.79^{***}$ ) and for the  $T_{\text{leaf}} - T_{\text{air}}$  ( $r = 0.90^{***}$  and  $r = 0.91^{***}$ ). The relationship of the  $T_{\text{leaf}}$  and meteorological data ( $T_{\text{air}}$  and VPD) is proved by correlation coefficients of up to  $0.57^{***}$ . No statistically significant relationships can be found between simple leaf temperatures and stomatal conductance. Further, CWSI and difference between  $T_{\text{leaf}}$  and  $T_{\text{air}}$  are not very strong related to stomatal conductance. These small or non-existent relationships are mainly based on the small number of available observations for the plant physiological measurements.

For each variable,  $p$ -values between treatment and control group at every time point are listed in Table III-3. Stomatal conductance (gs) shows significant differences between the two treatments of water supply starting from 2 days after stress initiation. At this point in time, none of the other variables respond. This is not surprising as gs is a genuine physiological variable and thus directly connected to the plant physiological response to stress.

Variables that respond at 7 days after stress comprise CWSI (computed from broadband TIR images), WI, and MSI based on leaf scale reflectance measurements in the NIR/SWIR spectral range. Contrarily, indices in the VIS (PRI and NDVI) do not respond at all. Consequently, the responding variables are all of a pre-visual kind, *i.e.* not computed from wavebands located in the VIS domain.

Surprisingly, CWSI computed from *Hyper-Cam LW* images only respond starting from 8 days after stress. Also the simple temperatures as well as  $T_{\text{leaf}} - T_{\text{air}}$  show consistent results for the two broadband approaches ( $p < 0.05$ ), whereas the *Hyper-Cam LW* temperatures ( $p = 0.063$  and  $p = 0.057$ ) are only significant at day 7 after stress initiation. Regarding the above mentioned temperature comparison these contradictory findings are mainly based on the very small differences in the corresponding  $p$ -values (*i.e.*, for  $T_{\text{leaf}} - T_{\text{air}}$  at 9 days after stress with  $p = 0.057$  for the *Hyper-Cam LW* and  $p = 0.046^*$  for the *Hyper-Cam LW* broadband), which is also obvious considering the boxplots (Fig. III-6). These small differences, in addition to a relatively large number of observations ( $n = 58$ ), last in statistically significant results at 5 % significance level.

Therefore, CWSI is most suitable for water stress detection based on temperatures in comparison to the simple leaf temperature ( $T_{leaf}$ ) and their correction with air temperature ( $T_{leaf} - T_{air}$ ), due to its robustness against the actual meteorological environment. For example, decreasing of VPD (Fig. III-3) from day 8 to day 9 leads to smaller absolute temperature differences between the two water treatment groups, which, comparing the three retrieval approaches, makes the results difficult to interpret. On the contrary, the CWSI shows consistent results for *Hyper-Cam LW*, *Hyper-Cam LW* broadband as well as Fluke TiR 1 (Table III-3).

Table III-3: p-values (level of statistical significance: \*\*\*p < 0.001, \*\*p < 0.01, \*p < 0.05) of Mann-Whitney-U-test per day after stress initiation.

Device	Days after stress	0	1	2	7	8	9
Porometer	<i>n</i>	9	12	12	11	12	-
	<i>gs</i>	0.365	0.155	0.047*	0.041*	0.001**	-
	<i>A</i>	0.365	0.066	0.066	0.009**	0.001**	-
	<i>E</i>	0.365	0.066	0.066	0.009**	0.001**	-
<i>Hyper-Cam LW</i>	<i>n</i>	37	58	57	36	56	58
	$T_{leaf}$	0.742	0.598	0.651	0.724	0.003**	0.063
	$T_{leaf} - T_{air}$	0.77	0.65	0.391	0.703	0.001**	0.057
	<i>CWSI</i>	0.658	0.785	0.554	0.365	<0.001***	0.002**
<i>Hyper-Cam LW</i> broadband	<i>n</i>	37	58	57	36	56	58
	$T_{leaf}$	0.732	0.475	0.645	0.537	0.002**	0.043*
	$T_{leaf} - T_{air}$	0.722	0.586	0.367	0.512	<0.001***	0.046*
	<i>CWSI</i>	0.635	0.827	0.528	0.15	<0.001***	<0.001***
Fluke	<i>n</i>	60	# 10	48	59	60	60
	$T_{leaf}$	0.607	0.155	0.569	0.035*	<0.001***	0.03*
	$T_{leaf} - T_{air}$	0.596	0.345	0.528	0.011*	<0.001***	0.036*
	<i>CWSI</i>	0.439	0.655	0.399	0.042*	<0.001***	<0.001***
ASD-Leaf	<i>n</i>	59	59	56	56	54	# 29
	<i>PRI</i>	0.158	0.13	0.147	0.91	0.362	0.972
	<i>NDVI</i>	0.115	0.096	0.179	0.366	0.002**	0.177
	<i>WI</i>	0.165	0.118	0.097	0.024*	<0.001***	0.188
	<i>LWI</i>	0.461	0.291	0.293	0.237	<0.001***	0.2
	<i>MSI</i>	0.169	0.144	0.192	0.047*	<0.001***	0.035*
	<i>NDWI</i>	0.309	0.331	0.23	0.095	0.001**	0.234
ASD-Canopy	<i>n</i>	60	59	59	0	# 15	60
	<i>PRI</i>	0.354	0.479	0.101	-	0.047*	<0.001***
	<i>NDVI</i>	0.343	0.053	0.425	-	0.036	<0.001***
	<i>WI</i>	0.065	0.682	0.302	-	0.86	1
	<i>LWI</i>	0.195	0.21	0.345	-	0.06	<0.001***
	<i>MSI</i>	0.065	0.461	0.271	-	0.306	0.238
	<i>NDWI</i>	0.063	0.91	0.331	-	1	0.39

# reduced sample size

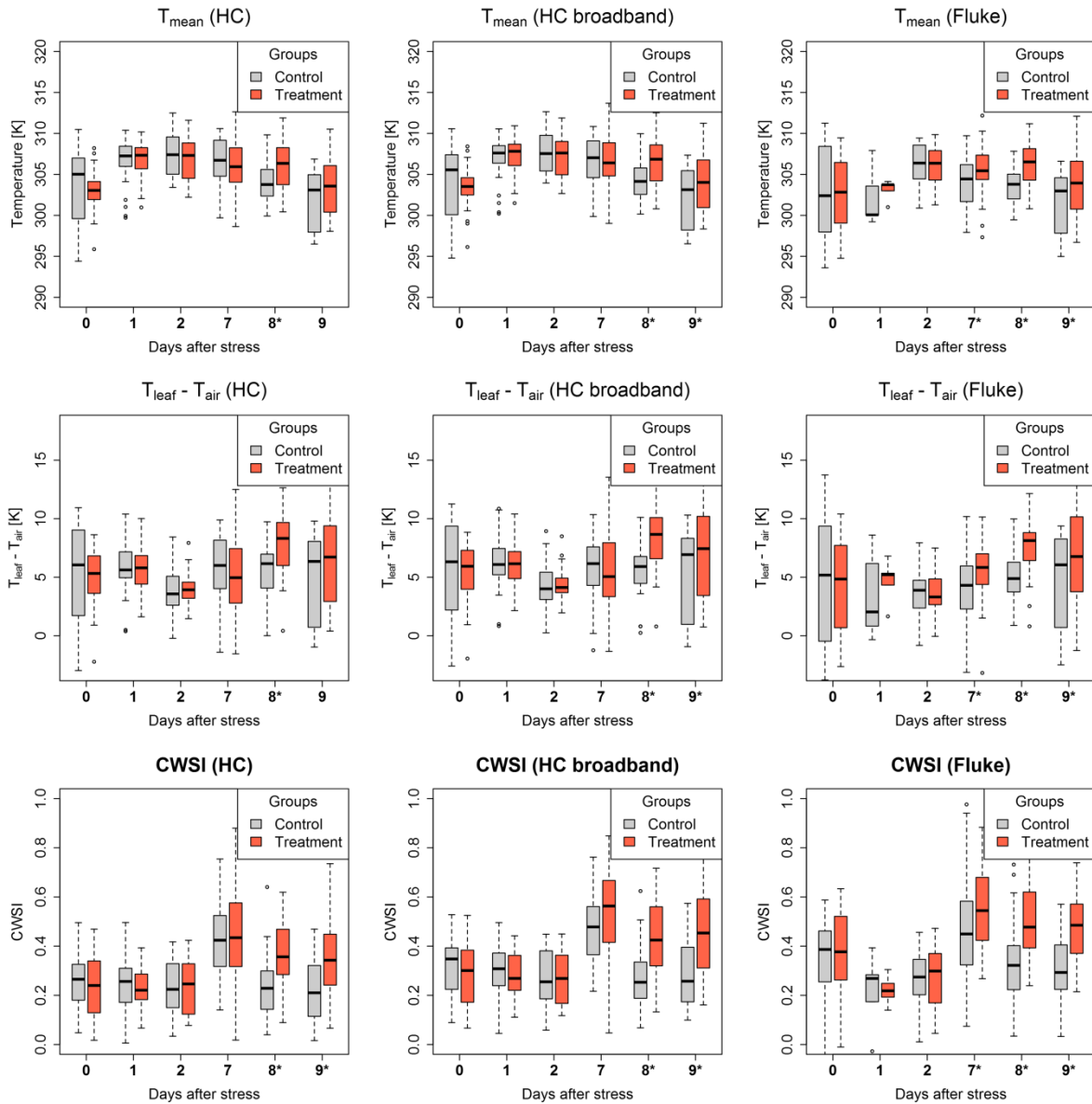


Fig. III-6: Boxplots per day after stress initiation of leaf temperatures ( $T_{\text{mean}}$ ),  $T_{\text{leaf}} - T_{\text{air}}$  and CWSI of the three temperature retrieval approaches (*Hyper-Cam LW* (HC), *Hyper-Cam LW* broadband (HC broadband), Fluke). Asterisks (\*) indicating significant difference between control and treatment group at 5 % significance level.

A critical point of this study is the gap of measurements of four days during 19<sup>th</sup> and 23<sup>rd</sup> July 2014 due to unsuitable weather conditions. However, even if measurements had been taken during day 3 – 6 after stress initiation, we presume that CWSI would have not been sensitive to water stress before days 7 to 8 of the experiment. As a matter of fact, undisturbed outdoor experiments of this kind can hardly be guaranteed under the prevailing weather conditions in Central Europe.



### 3.5 VNIR/SWIR

All indices linked to water content are highly statistically significant (Table III-3, Fig. III-7) at day 8 after stress for leaf measurements. Only MSI showed consistent results starting from day 7 ( $p=0.047^*$ ), which is comparable to the results of the Fluke TiR1. Considering that water related indices are highly correlated, *e.g.*  $r=0.94^{***}$  for WI and NDWI, none of the observed indices seems to be more sensitive comparing the two water treatment groups. The relationship between water sensitive indices at leaf scale and stomatal conductance are weak, *e.g.*  $p=0.30^*$  for WI (Fig. III-4).

NDVI and PRI are correlated with  $r=0.43^{***}$  for leaf and  $r=0.65^{***}$  for canopy scale. For the leaf measurements PRI showed no significant differences between the two water treatments. Whereas, NDVI shows highly significant results ( $p=0.002^{**}$ ) at day 8 after stress initiation at leaf scale. On the contrary, PRI treatment and control were significantly different ( $p=0.047^*$ ) based on canopy measurements taken 8 days after stress. Similar results were found for NDVI. Thus, the findings of Panigada *et al.* (2014) that PRI is more sensitive to early stadium of plant water stress than NDVI could not be confirmed.

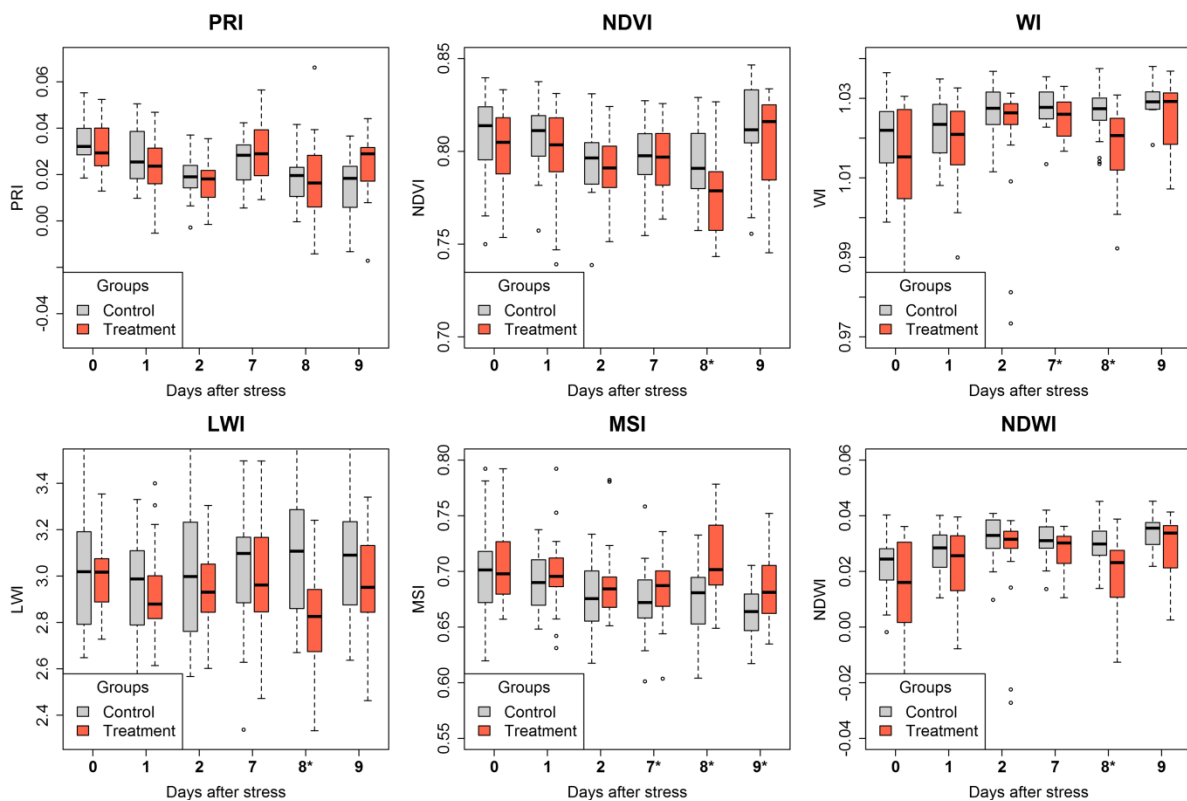


Fig. III-7: Boxplots per day after stress initiation of vegetation indices at leaf scale. Asterisks (\*) indicating significant difference between control and treatment group at 5 % significance level.

The results may be somewhat less robust due to the reduced sample size for leaf measurements at day 9 after stress (n=29) and canopy measurements at day 7 (n=0) and 8 (n=15).

Overall, using leaf measurements and narrowband spectral vegetation indices linked to water content, water stress can be also detected at the same date as using CWSI. Therefore, TIR based indices and NIR/SWIR indices related to plant water content are equally sensitive and respond quicker than visual indices such as PRI and NDVI.

### 3.6 Spectral Emissivity

Fig. III-8 shows the mean emissivity spectra per day after stress initiation for control (black) and treatment (red) groups. All spectra shown are a consistent shape with a prominent spectral feature around  $1000\text{ cm}^{-1}$  ( $10\text{ }\mu\text{m}$ ). For example, weaker features were recognized around  $950\text{ cm}^{-1}$  ( $10.53\text{ }\mu\text{m}$ ),  $1080\text{ cm}^{-1}$  ( $9.26\text{ }\mu\text{m}$ ) or  $1130\text{ cm}^{-1}$  ( $8.85\text{ }\mu\text{m}$ ). For the first three days, the two water treatments were not significantly different ( $p\text{-values} > 0.05$ ; right-handed ordinate). However, control and treatment groups were significantly different ( $p\text{-values} < 0.05$ ) starting from day 7 after stress initiation for a wavenumber greater than  $925.99\text{ cm}^{-1}$  ( $10.79\text{ }\mu\text{m}$ ) and even starting from  $886.02\text{ cm}^{-1}$  ( $11.29\text{ }\mu\text{m}$ ) for the last day of the experiment, respectively. At day 8 the differences were slightly less consistent, but still prominent. Therefore, spectral emissivity was equally sensitive to water stress as temperature based indices or NIR/SWIR based indices related to leaf water content.

For the water-stressed plants, emissivity increased in a consistent manner over all spectral bands, whereas the spectral shape remained unchanged. In particular, the spectral contrast around  $1000\text{ cm}^{-1}$  decreased for the treatment group, while the control group constantly remained at an averaged emissivity value of 0.98 for all days of the experiment. Buitrago *et al.* (2016) examined changes in spectral emissivity for cold and water stress on two different species, European beech (*Fagus sylvatica*) and rhododendron (*Rhododendron cf. catawbiense*), respectively. They observed a similar emissivity increase for stressed plants of the rhododendron and related this increase to cavity effects (*i.e.*, loss of spectral contrast due to multi scattering (Kirkland *et al.*, 2002)) as a result of an increase of cuticle thickness. Similar results were also observed by Ribeiro da Luz and Crowley (2007). Regarding these findings, we expected that potatoes would react similarly to the beeches with a decrease in emissivity in the TIR rather than the rhododendron with its thicker and more complex cuticle compared to the examined potato plants.

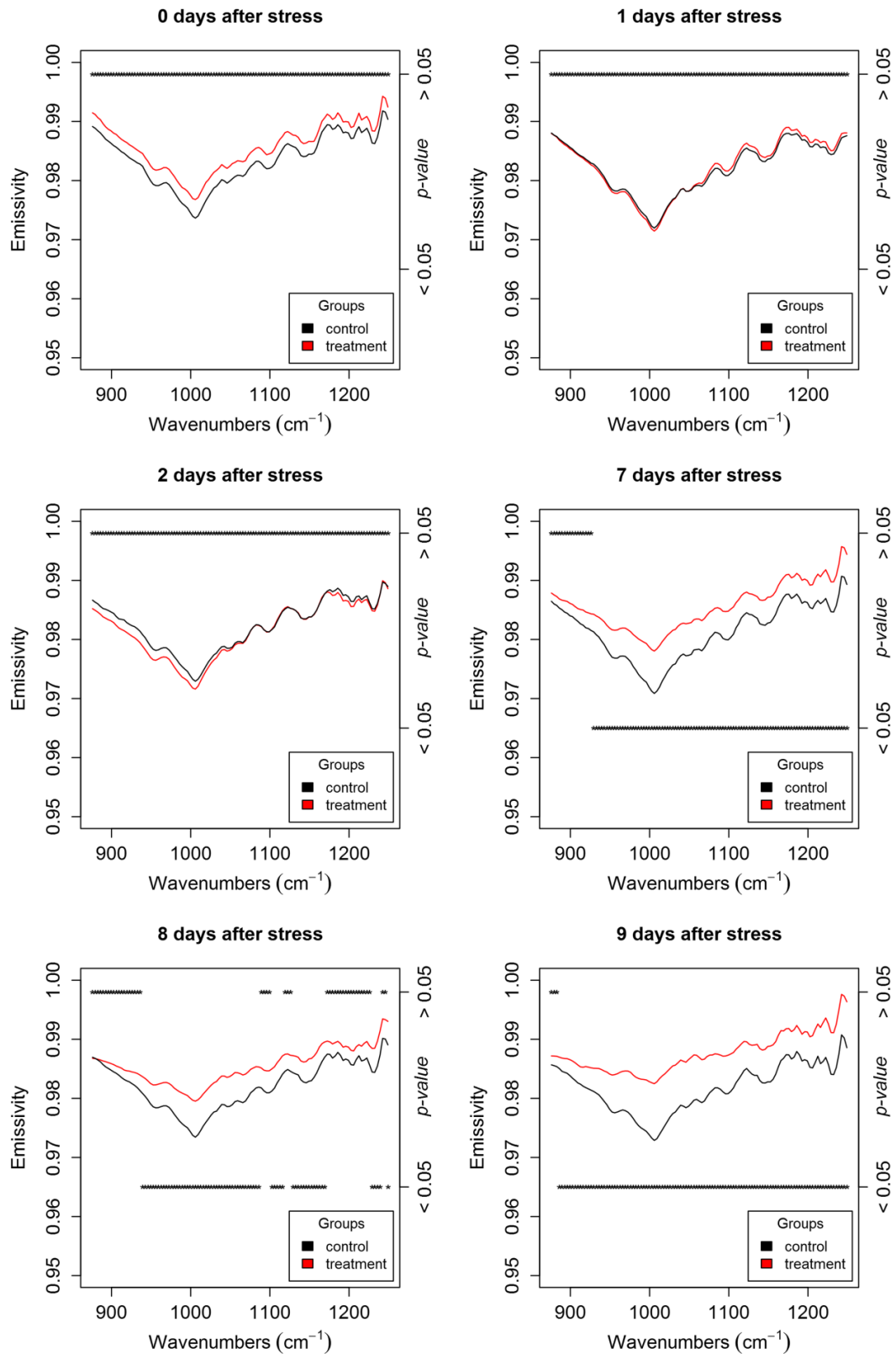


Fig. III-8: Mean emissivity spectra of potato plants (*Solanum tuberosum L. Cilena*) per day after stress initiation for control (black) and treatment (red) group. Corresponding  $p$ -values of a Mann-Whitney-U-tests at 5 % level of significance per wave-number are grouped by significance (right-handed and marked with asterisks).

Spectral features can be allocated neither to structural characteristics nor biochemical compounds, since corresponding reference measurements (*e.g.*, thickness of cuticles or biochemical analysis) for the current study were not available. Notwithstanding, the overall increase in emissivity of the treatment group may most likely be related to cavity effects resulting from biochemical and structural changes in the leaf due to shortage of water.

Finally, we would like to highlight that this study resulted in a successful detection of plant emissivity changes with stress measured through an emissive imaging device. On the contrary, most other studies (*e.g.*, Buitrago *et al.*, 2016; Ribeiro da Luz and Crowley, 2007; Ullah *et al.*, 2012b) have based plant emissivity retrieval on non-imaging and slow reflectance-based (DHR) measurements. Therefore, such TIR imaging sensors have the potential to map plant emissivity from airborne platforms.

## 4 Conclusion

In this paper, we systematically compared temperature based measures, NIR/SWIR reflectance based indices and VIS reflectance based indices, as well as spectral emissivity in their ability to detect water stress in potato plants. Besides, we investigated hyperspectral and broadband TIR imaging devices for their ability to measure leaf temperature as the basis for the temperature based measures.

The main findings are: (i) water stress as measured through stomatal conductance started on the second day after watering was stopped; (ii) temperature based indices and NIR/SWIR reflectance based indices related to plant water content as well as spectral emissivity were equally sensitive and responded quicker than visual indices such as PRI and NDVI; (iii) spectral emissivity showed a steady overall increase with increasing water stress; (iv) no striking differences appeared for hyperspectral and broadband TIR imagers in deriving accurate leaf temperatures; (v) among the temperature based measures, CWSI was most suitable for water stress detection, due to consideration of actual meteorological conditions based on dry and wet reference targets.

The most important conclusion of this research is that pre-visual measures of water stress (based on temperature, emissivity and water content) react faster than visual measures (based on leaf colour). The approach of pre-visual water stress detection is based on the physical nature of plant water reactions (*i.e.*, stomatal closure due to water shortage). Thus, it should be possible to transfer this finding to other crop types. Under presence of water stress, pre-visual indices should also work at times in the growing season different to those that have been examined. Therefore, hyperspectral TIR measures like temperature based indices and especially spectral emissivity have an enormous potential for water stress detection and irrigation management. Nevertheless, following Costa *et al.* (2013) it should be pointed out that there is still a need for establishing thresholds for TIR based stress indices (*e.g.*, CWSI) for different

biotic or abiotic stress effects and for different species and varieties depending on the plant specific structure and stress strategies (*e.g.*, hypo- or amphi-stomatous leaves).

The general validity of the experiment is slightly limited due to the four days gap of measurements and the reduced sample size of plant physiological and VNIR/SWIR reflectance measurements. Therefore, additional studies with comparable experimental setups should be conducted to confirm these results. Notwithstanding, given the typical weather conditions in Central Europe, it is in general very difficult to achieve over a sufficiently long period contiguous experimental datasets.

For potential application of TIR imaging in precision agriculture, the obtained results need to be confirmed at parcel and farm scales. The need for additional reference panel measurements for CWSI computation imposes a serious limitation for practical applications. Thus, there is a need to develop new approaches that characterise crop water stress independent from additional field measurements. Measures of spectral emissivity open new opportunities in TIR remote sensing and its application in agriculture. But, crop emissivity information is definitely limited by the availability of TIR imaging spectrometers, which are currently still very large in size and heavy (*e.g.*, *Hyper-Cam LW* with 30kg) and thus, limited to operating on airborne platforms. Additionally, to fully exploit the emissivity signal, more fundamental research is needed to understand how spectral emissivity is affected by biochemical compounds, structural properties and the effects of stressors.

## Acknowledgements

The authors would like to thank the Fonds National de la Recherche (FNR) of Luxembourg for funding the PLANTSSENS research project [‘Detection of plant stress using advanced thermal and spectral remote sensing techniques for improved crop management’; AFR reference: C13/SR/5894876] and the PhD research of Gilles Rock [AFR reference: 2011-2/SR/2962130]. Also, we wish to thank the Trier University’s Department for Geobotany for using their greenhouse facilities and measurement equipment. Furthermore, a special thank goes to Christian Bossung, Henning Buddenbaum, Kim Fischer, Miriam Machwitz and Franz Kai Ronellenfisch for their tireless support during the experiment.



# Chapter IV

## **A Comparative Analysis for Remote Sensing of Plant Water Stress Symptoms Based on Airborne Optical and Thermal Hyperspectral Images**

*Submitted to Int. J. Appl. Earth Obs. Geoinf.*

Max Gerhards, Martin Schlerf, Uwe Rascher, Thomas Udelhoven, Radosław Juszczak, Giorgio Alberti, Franco Miglietta and Yoshio Inoue

© 2017 Elsevier B.V. All rights reserved, given the fact that the manuscript will be accepted and published by Int. J. Appl. Earth Obs. Geoinf.

The following manuscript has been submitted to the *International Journal of Applied Earth Observation and Geoinformation* (peer-reviewed, Elsevier B.V.). The contribution of Max Gerhards to this scientific publication was the development and implementation of the experiment, as well as the processing, analysis and interpretation of the data. Furthermore, Max Gerhards took the lead in writing and editing the manuscript.

## Abstract

High-resolution airborne hyperspectral thermal infrared (TIR) together with sun-induced fluorescence (SIF) and hyperspectral optical images (visible, near- and shortwave infrared; VNIR/SWIR) were jointly acquired over an experimental site. The objective of this study was to evaluate the potential of these state-of-the-art remote sensing techniques for detecting water stress symptoms at airborne level.

Flights with two camera systems (Telops *Hyper-Cam LW*, Specim *HyPlant*) took place during 11<sup>th</sup> and 12<sup>th</sup> June 2014 in Latisana, Italy over a commercial grass (*Festuca arundinacea* and *Poa pratense*) farm with plots that were treated with an anti-transpirant agent (Vapor Gard®; VG) and a highly reflective powder (kaolin; KA). Both agents affect energy balance of the vegetation by reducing transpiration and thus reducing latent heat dissipation (VG) and by increasing albedo, *i.e.* decreasing energy absorption (KA). Concurrent *in situ* meteorological data from an on-site weather station, surface temperature and chamber flux measurements were obtained. Image data were processed to orthorectified maps of TIR indices (surface temperature ( $T_s$ ), Crop Water Stress Index (CWSI)), SIF indices ( $F_{687}$ ,  $F_{780}$ ) and VNIR/SWIR indices (photochemical reflectance index (PRI), normalized difference vegetation index (NDVI), moisture stress index (MSI), *etc.*). A linear mixed effects model that respects the nested structure of the experimental setup was employed to analyse treatment effects on the remote sensing parameters.

Airborne  $T_s$  were in good agreement ( $< 0.35$  K error) compared to *in situ*  $T_s$  measurements. Maps and boxplots of TIR based indices show diurnal changes:  $T_s$  was lowest in the early morning, increased by 6 K up to late morning as a consequence of increasing net radiation and air temperature ( $T_{air}$ ) and remained stable towards noon due to the compensatory cooling effect of increased plant transpiration; this was also confirmed by the chamber measurements. In the early morning, VG treated plots revealed significantly higher  $T_s$  compared to control (CR) plots ( $p = 0.01$ ), while SIF indices showed no significant difference ( $p = 1.00$ ) at any of the overpasses.

This shows that the polymer di-1-*p*-menthene had an anti-transpiring effect on the plant while photosynthetic efficiency of light reactions remained unaffected. VNIR/SWIR indices as well as SIF indices were highly sensitive to kaolin, because of an overall increase in spectral reflectance and thus a reduced absorbed energy. Comparing the performance of TIR, VNIR/SWIR and SIF for detecting water stress symptoms, temperature-based indices were most sensitive. The benefit of a multi-sensor approach is not only to provide useful information about actual plant status but also on the causes of biophysical, physiological and photochemical changes.



## 1 Introduction

In the context of climate change and an increasing global water scarcity, especially water deficit stress (normally shortened to water stress) is one of the most critical abiotic stressors to plant growth. In order to increase the quantity and quality of food production with a reduced amount of water used, the detection and quantification of plant stresses is of major interest for agriculture in general and precision farming in particular (Mulla, 2013). Remote sensing provides powerful tools in different spectral domains for spatio-temporal monitoring of water stress (Atzberger, 2013).

Plant response to water stress is expressed by a variety of physiological changes (*e.g.*, stomatal behaviour, leaf water content), biophysical changes (energy balance, leaf and canopy structure, biomass and yield) as well as photochemical processes (Hsiao *et al.*, 1976; Jones, 2004b; Yordanov *et al.*, 2003). Accordingly, various attempts have been made to detect these changes using remotely sensed signatures. To date, the main remote sensing imaging techniques for plant water stress detection are thermal imaging (TIR; 8 – 14  $\mu\text{m}$ ), visible, near- and shortwave infrared reflectance (VNIR/SWIR; 0.4 – 2.5  $\mu\text{m}$ ), and sun-induced fluorescence (SIF; 0.69 and 0.76  $\mu\text{m}$ ).

TIR imaging has been well studied for water stress detection (*e.g.*, Cohen *et al.*, 2005; Jones, 2004; Möller *et al.*, 2007). The underlying principle is that plant temperature rises with increasing water stress in comparison to a well-watered plant due to decreasing evaporative cooling through stomatal closing (Inoue *et al.*, 1990). Since stomatal closure is one of the first responses to water stress, plant temperature as measured by TIR sensors can be used to detect water stress pre-visually (Costa *et al.*, 2013; Jones, 2004a; Maes and Steppe, 2012). Plant temperature, however, is not solely governed by the plant water supply but also by the actual micro-meteorological conditions (*i.e.*, solar radiation, wind speed, leaf boundary layer resistance and vapour pressure deficit (VPD)). Therefore, as an alternative to using absolute temperature, several temperature-based indices were developed over the last decades with the aim to compensate for varying meteorological conditions. For example, the prominent Crop Water Stress Index (CWSI) (Jackson *et al.*, 1981) by means of artificial references does not require any additional meteorological measurements to be calculated. The usefulness of temperature-based indices has recently been demonstrated in several airborne studies (Panigada *et al.*, 2014; Rossini *et al.*, 2015b; Zarco-Tejada *et al.*, 2013, 2012). Currently, the main limitation of all temperature-based (*i.e.*, absolute temperature and temperature-based indices) approaches arises from the use of broadband infrared cameras with erroneous temperature retrieval by assuming an emissivity value that is pre-determined (*e.g.*,  $\epsilon = 0.97$  for vegetation) and constant over the spectral range from 8 to 14  $\mu\text{m}$ . For example, an error of 1% emissivity results in an absolute temperature error of 1 K (Jones, 2004a). However, just very recently hyperspectral TIR airborne imagers such as Telops *Hyper-Cam LW*, Itres *TASI-600*, or Specim *AisaOWL* became available. These devices allow for stable temperature and emissivity separation (TES) and very accurate temperature retrieval (*i.e.*,  $< 0.5$  K) by measuring the emitted radiation in many

narrow bands (Schlerf *et al.*, 2012). The importance of airborne (hyperspectral) TIR remote sensing lies in the possibility to bridge the gap between ground based thermography (*e.g.*, Maes and Steppe, 2012; Gerhards *et al.*, 2016) and proposed satellite missions, such as ECOSTRESS (Ecosystem Spaceborne Thermal Radiometer Experiment on Space Station, Stavros *et al.*, 2017), HypsIRI (Hyperspectral Infrared Imager, Lee *et al.*, 2015) or the hyperspectral mission concept HiTeSEM (High-resolution Temperature and Spectral Emissivity Mapping, Udelhoven *et al.*, 2017).

In the VNIR/SWIR domain, various spectral vegetation indices (VI) have been developed for the assessment of plant water status (*e.g.*, PRI, NDVI, MSI). Among the large variety of available indices, the PRI (photochemical reflectance index; Gamon *et al.* 1992) is related to non-photochemical heat dissipation, which may be linked to water availability and photosynthetic efficiency. In fact, PRI is heavily influenced by canopy effects and pigment content, but Suárez *et al.* (2010, 2009, 2008) suggest that the use of PRI in combination with radiative transfer modelling, accounting for these effects, can effectively provide very good means for monitoring water stress in crops and natural vegetation at airborne level. However, the ability of the PRI to be used for water stress detection is not conclusive at a small scale experimental ground and airborne level (Gerhards *et al.*, 2016; Panigada *et al.*, 2014; Rossini *et al.*, 2015b).

At the same time, remote sensing of sun-induced fluorescence (SIF) has become increasingly popular over the last decade with a variety of studies ranging from ground-based experiments to airborne campaigns and even towards satellite missions (see Meroni *et al.* (2009) for a comprehensive review). In principle, radiative energy absorbed by leaf chlorophyll is processed along three competing pathways: (i) conversion of photosynthetic active radiation (PAR) to sugars through photosynthesis, (ii) the re-emission of non-used energy through chlorophyll fluorescence or (iii) dissipation of heat (Porcar-Castell *et al.*, 2014). Hence, these three processes are in competition to each other; variation in one of the processes affects the others (Rossini *et al.*, 2015a). For example, plant photosynthetic efficiency is reduced under environmental stress conditions (*i.e.*, water or nutrient shortage, heat stress, and other types of stress) due to plants protective mechanisms (*e.g.*, leaf rolling reduces the plants surface and therefore the PAR absorbance; stomatal closure reduces water loss and CO<sub>2</sub> uptake). In this context, SIF is expected to be a direct indicator of photosynthetic efficiency and plant stress, although further studies are needed to establish a consistent basis for robust assessment (Rascher *et al.*, 2015; Porcar-Castell *et al.*, 2014). The *HyPlant* sensor facilitates subnanometer airborne acquisitions from the red (0.68 µm) towards the far red (0.78 µm) spectral range. Current experiments using the *HyPlant* sensor demonstrated the capability of quantitative plant stress detection at airborne level using both red and far red chlorophyll fluorescence peaks (Rossini *et al.*, 2015a).

These preceding studies suggest that plant water stress symptoms may be detectable by means of the three approaches (TIR temperature indices, VNIR/SWIR VIs and SIF indices). However, since they are based on different models and physiological processes, the sensitivity and suitability of these approaches may vary depending on the target and environmental conditions. Therefore, to assess the detectability of water stress symptoms by the three approaches, we conducted a field-scale experiment specifically designed to tentatively evaluate the potential of state-of-the-art remote sensing at airborne level. *Hyper-Cam LW* as well as *HyPlant* sensors were flown over a commercial grass farm. Water stress symptoms were simulated by treating grass surfaces with two different chemical agents and comparing them to untreated Control (CR) plots.

The first agent, the anti-transpirant Vapor Gard® (VG; Miller Chemical & Fertilizer, Hanover, Pennsylvania 17331 USA), is composed of di-1-*p*-menthene, a natural terpene polymer. The emulsion surrounds the leaves with a thin film and is supposed to reduce the plants water transpiration by limiting stomatal conductance. Thus, VG is recommended for farming to reduce water loss and prevent water stress in times of limited water availability (Francini *et al.*, 2011; Mikiciuk *et al.*, 2015; Ouerghi *et al.*, 2015). Because of decreasing stomatal conductance, transpiration is also reduced and consequently plant surface temperature is expected to be significantly increased in comparison to a CR plot. Furthermore, VG does not only have an effect on the permeability of water but also reduces CO<sub>2</sub> uptake rates (Plaut *et al.*, 2004). The second agent, kaolin (KA) is a highly reflective white powder and can be dissolved in water and sprayed on plants. The white color of KA increases the albedo of the plant surface and therefore reduces the absorbed light energy (APAR).

Thus, we assume (Table IV-1) that VG treated plants (in comparison to CR plants) have: i) decreased transpiration, ii) increased leaf temperature, and iii) decreased photosynthetic activity, while keeping relatively high leaf water and chlorophyll content (in case of enough soil moisture). We assume further that KA treated plants (in comparison to CR plants) have: iv) decreased absorbed radiation resulting in decreased transpiration under energy-limited conditions (in case of sufficient soil water), but also vi) little change in stomatal conductance, leaf temperature, photosynthetic efficiency, leaf water and chlorophyll content.

Table IV-1: Assumed effects of treatments on spectral domains.

Treatment	Effect on VNIR/SWIR	Effect on TIR	Effect on SIF
CR	Normal	Normal	Normal
VG	Unchanged indices due to normal leaf water content and chlorophyll content	Increased $T_s$ due to reduced transpiration	Variations in SIF indices due to changes in photosynthetic electron transport rates
KA	Overall increase in reflectance and corresponding reduction of absorbed APAR and thus, a change in index values	Reduced $T_s$ due to decrease in absorbed radiation	Reduced SIF indices due to decreased overall available absorbed energy (APAR)

However, it is still unknown how well they allow the detection of plant water stress symptoms at airborne level. Thus, the overall aim of this study was to comparably assess the capability of selected TIR and VNIR/SWIR hyperspectral remote sensing indices, as well as SIF remote sensing for detection of plant water stress symptoms. The specific objectives were: i) a systematic comparison of the ability of different temperature-based indices (*e.g.*, CWSI,  $T_s$ ,  $T_s - T_{air}$ ), traditional VNIR/SWIR indices (*e.g.*, PRI, NDVI, MSI), and SIF indices to detect plant stress symptoms as induced by chemical treatments (VG and KA); ii) an assessment of why the different indices may or may not have changed from treatments with respect to the underlying physiological processes; iii) specifically examining diurnal changes in temperature-based index values regarding different treatments.

## 2 Materials and Methods

### 2.1 Experimental Design

In June 2014, a field scale experiment was conducted on a 2 ha commercial grass (*Festuca arundinacea* and *Poa pratense*) farm near to Latisana, north east Italy (45°46'46.1"N, 13°00'50.5"E) (Fig. IV-1). Plant characteristics were modified by two chemical treatments (VG and KA) to simulate water stress symptoms. A replicated block design with three replicates was adopted (Fig. IV-1). The average plot size was 12 x 9 m for CR and VG and 9 x 9 m for KA plots. In the evening of 10<sup>th</sup> June 2014, tagged plots were treated by 15 l of an emulsion of 3% VG and 15 l of 60 g l<sup>-1</sup> KA.

During the experiment, airborne and *in situ* data were collected. Airborne data were acquired with two camera systems (Telops *Hyper-Cam LW*, Specim *HyPlant*) during 11<sup>th</sup> and 12<sup>th</sup> June 2014. Concurrent *in situ* meteorological data from an on-site weather station, surface temperature and chamber flux measurements were obtained.

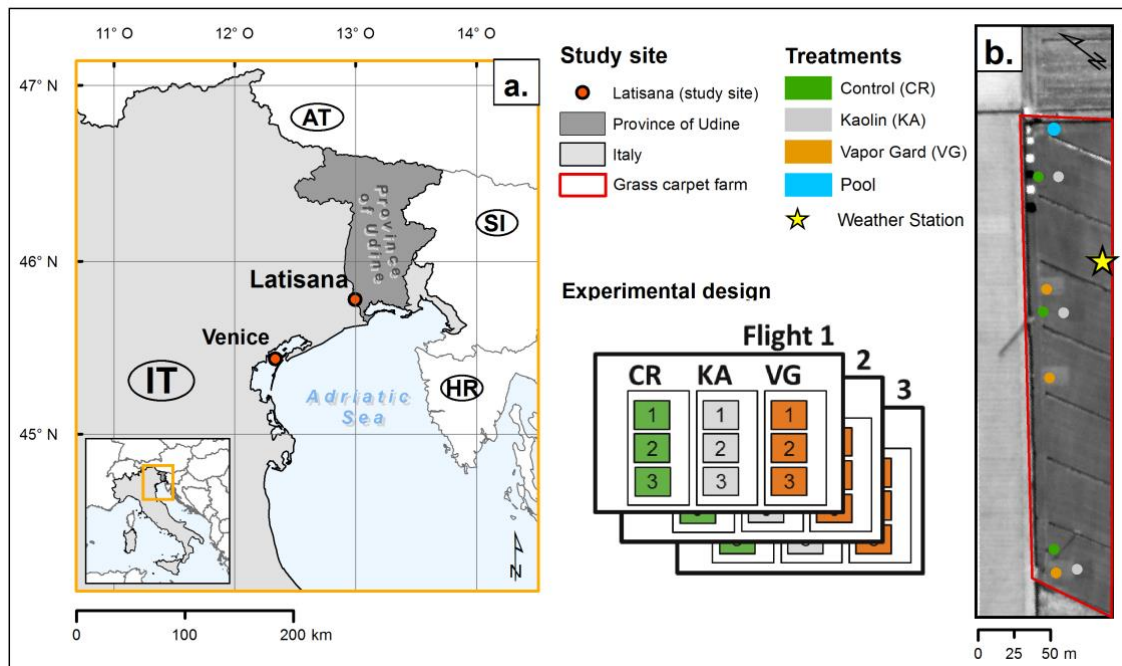


Fig. IV-1: Overview of the study site with the experimental setup. The study site was located in north eastern Italy near the town of Latisana (a.). (b.) shows the locations of the experimental plots, pool and weather station. A scheme of the experimental design is presented in the legend.

## 2.2 Airborne Images

### 2.2.1 Overview

The airborne flight campaign was organised in the framework of an annual FLEX-EU campaign. The experimental site was overpassed three times during 11<sup>th</sup> and 12<sup>th</sup> June from both *Hyper-Cam LW* and *HyPlant* airborne sensor, respectively. Hyperspectral TIR images were acquired using Telops *Hyper-Cam LW* on 11<sup>th</sup> June 2014 in the early morning at 09:18, late morning at 10:48 and at midday near solar noon at 12:51 (all Central Europe Solar Time, CEST). Unfortunately, synchronised overpasses of both airborne sensor were not possible. Thus, the nearest available three *HyPlant* imagery acquisitions were selected. The first flight occurred on 11<sup>th</sup> June at 14:52, whereas, second and third overpasses were performed one day later (12<sup>th</sup> June) at 12:02 and 13:40 (all CEST), respectively.

*Hyper-Cam LW* sensor was flown at a survey height of 1430 m above ground resulting in a ground sampling distance (GSD) of 0.5 m per pixel. *HyPlant* sensor was flown at 600 m height resulting in 1 m GSD. To obtain a consistent dataset, *HyPlant* images were co-registered to Telops *Hyper-Cam LW* spatial resolution (0.5 m). Nearest neighbor interpolation was used for resampling. Over each plot a circular region of interest (ROI, size: 32 pixels) was defined and the corresponding image values were extracted and stored in a database. The ROI were defined to be circular around the central pixel of each plot, in order to prevent any boundary effects. Each ROI covers a grass surface area of approximately 8 m<sup>2</sup>.

### 2.2.2 Hyperspectral Thermal Images

Hyperspectral TIR airborne data were recorded using a *Hyper-Cam LW* (Telops Inc., Québec, Canada, [www.telops.com](http://www.telops.com)) mounted on a customized airborne platform. The base instrument is a FTIR (Fourier transformed infrared) spectrometer consisting of a 320 x 256 pixel MCT (mercury cadmium telluride) focal plane array (FPA) detector with up to  $0.25 \text{ cm}^{-1}$  spectral resolution in the spectral range of 7.7 to  $11.5 \text{ }\mu\text{m}$  ( $1298.7$  to  $869.6 \text{ cm}^{-1}$ ). The camera system is provided with two internal blackbodies with a known emissivity ( $\epsilon \geq 0.99$ ) for radiometric calibration. The airborne platform combines the Image Motion Compensator (IMC) mirror, an Inertial Measurement Unit (IMU) consisting of GPS and Inertial Navigation System (INS), as well as a visible boresighted camera mounted on a base plate (Schlerf *et al.*, 2012). The IMC mirror compensates for airborne forward motion and guarantees gapless image acquisition. Furthermore, the IMC balances airborne pitch and roll, while the stabilization platform reduces airborne vibrations and airborne yaw. The IMU recordings enable ortho-rectification and geo-referencing of the collected data. Hyperspectral TIR images were acquired with a spectral sampling distance of  $6.65 \text{ cm}^{-1}$  with  $8 \text{ cm}^{-1}$  FWHM (Full Width at Half Maximum) in the spectral domain from  $878$  to  $1277 \text{ cm}^{-1}$  resulting in 60 spectral bands.

In order to retrieve LST (Land Surface Temperature) from hyperspectral *Hyper-Cam LW* data cubes several radiometric and geometric processing steps were performed. First, raw interferograms were transformed to spectral radiances ( $\text{W m}^{-2} \text{ sr}^{-1} \text{ cm}^{-1}$ ) using a Fourier transformation, followed by a two-point calibration based on the internal blackbodies with known temperature and emissivity ( $\epsilon \geq 0.99$ ). This process was conducted using Telops Reveal calibrate software resulting in single image cubes in units of spectral radiance. Second, the single image cubes were ortho-rectified and geo-referenced using the information of the IMU, before they were mosaicked to single flight lines. This geometric correction was performed using Telops Airborne software. Third, the so-called “Blackbody Fit” approach (Kahle and Alley, 1992) was performed to retrieve LST from spectral radiances. This simple approach needs a minimum of a priori knowledge to fit the measured spectral radiances of each pixel to a Planck-curve with a known temperature. Following Schlerf *et al.* (2012) the fit was performed in the spectral range between  $880 \text{ cm}^{-1}$  ( $11.4 \text{ }\mu\text{m}$ ) and  $912 \text{ cm}^{-1}$  ( $11.0 \text{ }\mu\text{m}$ ) and with an assumed emissivity of 97 % ( $\epsilon = 0.97$ ), which is in good agreement with common findings about plant emissivity (*e.g.*, Buitrago *et al.*, 2016; Gerhards *et al.*, 2016; Rock *et al.*, 2016; Salisbury and D’Aria, 1992). The best fit was then found by iteratively changing the temperature of the Planck-curve and using a non-linear least square curve fitting approach to assess the goodness of fit (Lourakis, 2005).

Any atmospheric distortions within the optical path (*i.e.*, upwelling and downwelling radiance as well as transmittance) were neglected for the following reasons: (i) because of the low survey altitude, the atmosphere imposes limited effects on the recorded signal; (ii) the small scale study site limited horizontal variations in atmospheric gas concentrations and (iii) only relative differences in temperature (*i.e.*, temperature-based indices) were studied.

To validate the accuracy of LST retrieval, airborne temperature ( $T_{airborne}$ ) were compared to ground measured temperatures ( $T_{ground}$ ) of a water body.  $T_{ground}$  was measured at the surface of a water filled pool along a profile of five thermocouples. Thermocouples have a certificated accuracy (ISO 17025) of 0.5 K.  $T_{airborne}$  was extracted from corresponding TIR images as an average of four pixels within the pool.

Since absolute plant temperatures are very sensitive to rapidly changing meteorological conditions and therefore are not very suitable to detect water stress symptoms and diurnal changes, two additional temperature-based indices were calculated: i) the difference between plant surface and air temperature ( $T_s - T_{air}$ ) based on the approach of Stress Degree Day (SDD) (Jackson *et al.*, 1977) and ii) the in-scene Crop Water Stress Index (CWSI) approach following the idea of using artificial wet and dry reference surfaces (Jones, 1999a). CWSI was retrieved using following equation (IV-1):

$$CWSI = \frac{T_s - T_{wet}}{T_{dry} - T_{wet}} \quad (IV-1),$$

where  $T_s$  is the plant surface temperature,  $T_{wet}$  for the lower boundary of plant surface temperature, assuming a leaf with stomata fully open and a potential transpiration rate of 100% and  $T_{dry}$  is the upper boundary compared to a non-transpiring leaf with stomata completely closed. Since the fleece material artificial reference surfaces located next to the treatment plots turned out unsuitable for this study (*i.e.*, wet reference surface was warmer than coolest CR pixel and dry reference surface was up to 15 K warmer compared to the warmest pixel of the VG treatment), CWSI was determined by an empirical approach. The lower limit ( $T_{wet}$ ) was calculated using the coolest 5 % of the CR treatment pixel (Gonzalez-Dugo *et al.*, 2013), assuming that the CR plots were well watered. The upper boundary was calculated by adding 5 K to the current  $T_{air}$  (*i.e.*,  $T_{dry} = T_{air} + 5$  K). This approach has been previously suggested by Meron *et al.* (2003) and Cohen *et al.* (2005).

### 2.2.3 Hyperspectral Optical Images

*HyPlant* airborne sensor was developed at Forschungszentrum Jülich (Germany) in cooperation with Specim Spectral Imaging Ltd ([www.specim.fi](http://www.specim.fi)). *HyPlant* was designed as an airborne demonstrator of ESA's Fluorescence Explorer (FLEX) satellite mission. The push-broom imager consists of two modules. First, the dual-channel module is measuring reflected surface radiance in the wavelength range of 0.38 – 0.97  $\mu\text{m}$  with a spectral resolution of 4 nm (FWHM) at a sampling interval of 1.7 nm and from 0.97 – 2.5  $\mu\text{m}$  with 13.3 nm FWHM at 5.5 nm sampling interval, respectively. Second, the fluorescence module was especially designed to retrieve the emitted fluorescence signal within the atmospheric oxygen bands, O<sub>2</sub>-A (760 nm, F<sub>760</sub>) and O<sub>2</sub>-B (687 nm, F<sub>687</sub>). Therefore, the fluorescence module provides a very high spectral resolution of 0.25 nm (FWHM) covering the spectral range from 670 to 780 nm resulting in 1024 spectral bands. Therefore, *HyPlant* is the only available airborne imaging spectrometer offering the detection of the two broadband chlorophyll fluorescence emission peaks at 687 and 760 nm. Further technical details, sensor calibration and image processing are documented in Rascher *et al.* (2015).

The emitted sun-induced chlorophyll fluorescence F<sub>760</sub> and F<sub>687</sub> were retrieved from *HyPlant*'s fluorescence module images using a Fraunhofer Line Depth (FLD) approach. In detail, the fluorescence retrieval implemented for *HyPlant* is based on the 3FLD approach as initially introduced by Maier *et al.* (2003) and the iFLD method as proposed by Alonso *et al.* (2008). The method was fundamentally refined and adapted to high performance spectrometers and for airborne fluorescence retrieval. In essence it is complemented with the simulation of atmospheric components using MODTRAN5 (Berk *et al.*, 2005) in combination with the MODTRAN5 interrogation technique as introduced by Verhoef & Bach (2003), and using an empirical constraint based on non-fluorescing reference surfaces (see Wiencke *et al.* (2016) for a recent detailed description of the retrieval method).

Additionally, several reflectance-based narrowband VIs (Table IV-2) related to plant physiology, structure and water content were calculated from *HyPlant* dual-channel module to determine their ability of detecting plant water stress symptoms induced by chemical treatments. PRI (Gamon *et al.*, 1992) was calculated using the average of three spectral bands in *HyPlant* closest to 531 nm and 570 nm, respectively (centre wavelength  $\pm 1$  band). As simple ratio indices related to water content we applied the Water Index (WI) (Peñuelas *et al.*, 1993), the Leaf Water Index (LWI) (Seelig *et al.*, 2008) and the Moisture Stress Index (MSI) (Hunt Jr. and Rock, 1989), which are sensitive in the domain of the water absorption bands at 970 nm, 1450 nm and 1600 nm respectively. Additionally, the Simple Ratio (SR) (Jordan, 1969) index and the Normalized Difference Vegetation Index (NDVI) were evaluated (Rouse *et al.*, 1974). All water content and greenness related indices were calculated with a spectral window of centre wavelength  $\pm 4$  *HyPlant* spectral bands.



Table IV-2: Optical (VNIR/SWIR) narrow-band indices grouped by category: (1) xanthophyll pigments, (2) greenness and (3) water content. R is the reflectance center wavelength of *HyPlant* Dual Chanel in nm.

Category	Index	Equation	Reference
<i>Xanthophyll</i>	PRI	$PRI = (R_{570} - R_{531}) / (R_{570} + R_{531})$	Gamon <i>et al.</i> (1992)
<i>Greenness</i>	SR	$SR = R_{800} / R_{670}$	Jordan (1969)
	NDVI	$NDVI = (R_{800} - R_{670}) / (R_{800} + R_{670})$	Rouse <i>et al.</i> (1974)
<i>Water content</i>	WI	$WI = R_{900} / R_{970}$	Peñuelas <i>et al.</i> (1993)
	LWI	$LWI = R_{1300} / R_{1450}$	Seelig <i>et al.</i> (2008)
	MSI	$MSI = R_{1600} / R_{820}$	Hunt & Rock (1989)

### 2.3 Meteorological Data

A weather station was set up close to the experimental plots within a non-treated grass area. The station was equipped with a four band net radiometer (NR01-L Campbell Sci., USA), an air temperature and humidity sensor (HMP45AC, Vaisala, Finland), soil water content (TDR CS616, Campbell Sci., USA), and canopy temperature (Calex Electronics, UK). All of the sensors were connected to a data logger (CR1000, Campbell Sci., USA) and acquired at 0.1 Hz, then averaged half hourly. As vapour pressure deficit (VPD) is a more sensitive indicator of water vapour condition than relative humidity (RH) and therefore describes the interaction of plants with the intervening atmosphere more precisely, VPD (hPa) was calculated using equation (IV-2) (Struthers *et al.*, 2015):

$$VPD = e_s \times \frac{100 - RH}{100} \quad (IV-2),$$

$$e_s = 6.11 \times \exp\left(\frac{L}{Rv} \left(\frac{1}{273} - \frac{1}{T}\right)\right)$$

where  $e_s$  is the saturation vapour pressure in mbar, L is the latent heat of vaporization ( $2.5 \times 10^6 \text{ J kg}^{-1}$ ), Rv is the specific gas constant for water vapour ( $461 \text{ J K}^{-1} \text{ kg}^{-1}$ ) and T is the current air temperature (K). RH is the relative humidity (%).

## 2.4 Chamber Flux Measurements

CO<sub>2</sub> and H<sub>2</sub>O flux measurements were taken on 11<sup>th</sup> June 2014 over plots treated with VG and CR. For logistical reasons no chamber flux measurements were taken at KA treated plots. Non-steady-state flow-through a chamber system consisting of transparent and non-transparent chambers was used to measure net ecosystem exchange (*NEE*) and ecosystem respiration (*Reco*) fluxes, respectively. Both chambers had a volume of 0.3 m<sup>3</sup> and their dimensions were 0.78 x 0.78 x 0.50 m. Chambers were equipped with fans, temperature sensor and a vent to equilibrate pressure changes during measurements (Juszczak *et al.*, 2013). Water vapour fluxes were calculated based on measurements taken with transparent chamber made from 3 mm thick PLEXIGLAS (Clear 0A000 GT, Evonik Industries, Germany) (Acosta *et al.*, 2017; Chojnicki *et al.*, 2010). Gas concentration changes in the chambers were measured with an infrared gas analyser (LI-840, LICOR, USA) installed in the portable control box equipped with a pump and CR1000 data logger (Campbell Sci., USA). Air was circulated between the chamber and the analyser in the closed loop with the flow rate of 0.7 Lmin<sup>-1</sup>. During measurements chambers were fixed to the preinstalled soil frames (one per experimental plot) inserted to soil to 5 cm depth on 5<sup>th</sup> of June 2014. The chamber closure time used for *NEE* and H<sub>2</sub>O fluxes estimation did not exceed 1 minute to avoid overheating of the chamber headspace and 2 minutes for the non-transparent chamber. The chambers were un-cooled in order to not reduce H<sub>2</sub>O fluxes due to condensation on cooling items in accordance with Chojnicki *et al.* (2010) and Acosta *et al.* (2017). The chamber measurements started at 9:30 in the morning and were continued until 17:00 (CEST), but only measurements taken until the 3<sup>rd</sup> overpass at 13:40 were considered in analyses corresponding to the *Hyper-Cam LW* overpasses. There were 10 flux measurements taken on VG and CR plots within this time window.

H<sub>2</sub>O and CO<sub>2</sub> fluxes were calculated based on a gas concentration changes over the closure time using the linear regression type as described in Juszczak *et al.* (2013). In order to avoid underestimation of the fluxes due to a gas saturation, fluxes were calculated from the first 30 – 40 seconds of measurements for data with the highest regression slopes in accordance with Hoffmann *et al.* (2015). Coefficient of determination ( $R^2$ ) for the fluxes considered in analyses exceeds 0.9.

Gross Ecosystem Productivity (GEP), indicating the amount of CO<sub>2</sub> assimilated by grass in photosynthesis, was calculated as a sum of absolute *NEE* and *Reco* values from the two consecutive measurements of *NEE* and *Reco* (*Reco* was measured just after *NEE*).

Incoming PAR was measured continuously by a PAR quantum sensor (SKP215, Sky Instruments, UK) installed on a weather station located approximately 100 meters from the experimental plots. Considering that chamber flux measurements were taken at CR and VG plots at different times and under different PAR- and temperature conditions, the H<sub>2</sub>O fluxes were normalised over PAR, dividing H<sub>2</sub>O fluxes by PAR (both in  $\mu\text{mols m}^{-2} \text{s}^{-1}$ ).

## 2.5 Statistical Analysis

For statistical analysis, we used R (R Core Team, 2017) and the R package *nlme* (Pinheiro *et al.*, 2017) to perform a linear mixed effects model to describe the nested structure of our experimental setup. An interaction term between the variables treatment and flight time was introduced as fixed effects, because we were rather interested in the comparison of the treatments at each flight time and less in the differences between the treatments accumulated over all three overpasses. As random effects, we set the variable ID (flight : treatment : plot), which describes the nesting of the variables plot within treatment and treatment within flight as well as the repeated measure problem of the three overpasses. To take care of the autocorrelation of neighbouring pixels within each plot, we included a Gaussian spatial correlation structure term in the model for the residuals, which considered a distance ( $d$ ) dependent correlation following a Gaussian distribution for a certain range ( $r$ ) ( $\exp\{-[(r_{1-2})/d]^2\}$ ). The overall number of observation is  $n = 864$ , 3 treatments with 3 repetitions each by 3 flights by 32 pixels per plot. Visual inspection of residual plots did not reveal any obvious deviations from homoscedasticity or normality. For pairwise comparison we used a student  $t$ -statistic with a 0.05 Tukey-adjusted significance level, which is implemented in the R package *lsmeans* (Lenth, 2016).

## 3 Results

### 3.1 Meteorological Data

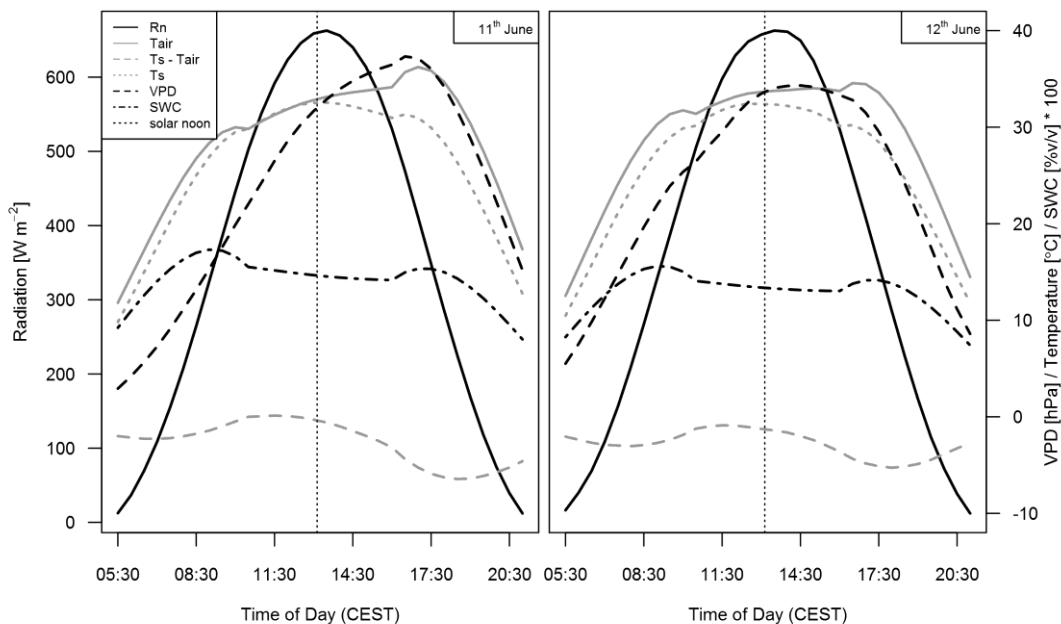


Fig. IV-2: Environmental conditions (net radiation ( $R_n$ ), air temperature ( $T_{air}$ ), surface temperature ( $T_s$ ),  $T_s - T_{air}$ , vapour pressure deficit (VPD), as well as soil water content (SWC)) for 11<sup>th</sup> and 12<sup>th</sup> of June 2014 over a non-treated grass surface measured by the weather station.

Fig. IV-2 shows the diurnal variations of environmental conditions (net radiation (Rn), air temperature ( $T_{air}$ ), surface temperature ( $T_s$ ), the difference of  $T_s$  and  $T_{air}$ , and vapour pressure deficit (VPD) as well as soil water content (SWC)) for 11<sup>th</sup> and 12<sup>th</sup> of June from sunrise (05:30 CEST) until sunset (21:00 CEST). The meteorological data were retrieved from the weather station measurements (see section 2.2). Measurements were taken over an untreated site and can therefore be considered as a Control (CR) plot. In fact, no major differences were observed between the 11<sup>th</sup> and 12<sup>th</sup> of June. For both dates, Rn steeply increased from 0 Wm<sup>-2</sup> to a maximum of 670 Wm<sup>-2</sup> around solar noon, before it decreased again.  $T_{air}$  and  $T_s$  also rapidly rose on the 11<sup>th</sup> June until solar noon from 19.7 to 32.6 °C and 14.6 to 32.4 °C, respectively. Almost similar temperatures were observed on the 12<sup>th</sup> of June. Similarly, VPD almost increased tenfold (3.8 – 31.5 hPa) until 13:30 (CEST) for both dates. After solar noon,  $T_s$  decreased, whereas  $T_{air}$  and VPD still rose until late afternoon. This decrease of  $T_s$  with a simultaneously increase of  $T_{air}$  and the high capability of potential transpiration characterised by high VPD values, results from evaporative cooling and indicates plants are highly transpiring in the afternoon. Thus, we can state that during the 11<sup>th</sup> and 12<sup>th</sup> of June 2014 plant water supply over control plots was sufficient and no actual water stress prevailed, which is in very good agreement with the constant values of SWC (Fig. IV-2).

### 3.2 Chamber Flux Measurements

Fig. IV-3 shows the diurnal course of H<sub>2</sub>O flux (solid lines) and PAR (dashed lines) for CR (green) and VG (orange) treatments observed by chamber flux measurements. During the day, H<sub>2</sub>O flux and PAR increased until solar noon. The observed variations in the measured fluxes might reflect the differences between plots (measurements were taken on three CR and three VG plots). The average H<sub>2</sub>O flux rates (n = 10, both for CR and VG) for the time between 9:30 and 13:40 (CEST) was 20% higher in average for CR plots ( $10.6 \pm 2.61$  mmols H<sub>2</sub>O m<sup>-2</sup> s<sup>-1</sup>) than for VG plots ( $8.44 \pm 3.21$  mmols H<sub>2</sub>O m<sup>-2</sup> s<sup>-1</sup>), although this difference was not significant ( $p = 0.11$ , Fig. IV-3 lower left). Considering that measurements were taken at different time and under different PAR and temperature conditions, the H<sub>2</sub>O fluxes were normalised over PAR (Fig. IV-3 lower right). After normalisation with PAR the difference between VG and CR transpiration was significant ( $p < 0.05^*$ ), which proves that VG substantially reduced transpiration.

The average *GEP* (n = 10, both for CR and VG) for the same time between 9:30 and 13:40 (CEST) was 21% higher ( $p < 0.01^{**}$ , not shown) for CR plots ( $35.91 \pm 5.15$  μmols CO<sub>2</sub> m<sup>-2</sup> s<sup>-1</sup>) than for VG plots ( $28.51 \pm 9.59$  μmols CO<sub>2</sub> m<sup>-2</sup> s<sup>-1</sup>).

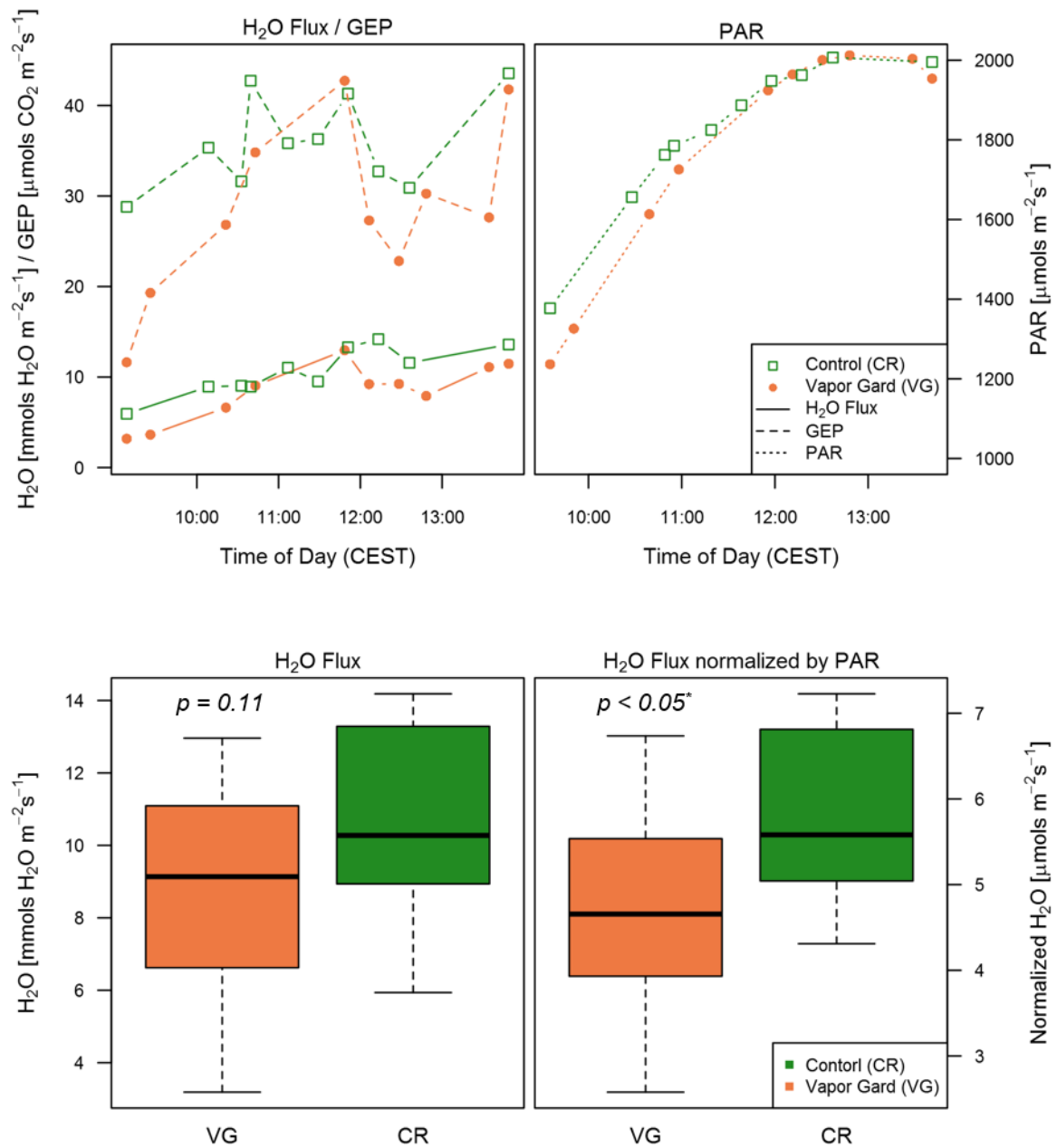


Fig. IV-3: Diurnal changes in chamber flux measurements for CR (green) and VG (orange) treatments. Solid lines are showing H<sub>2</sub>O fluxes in  $\text{mmols H}_2\text{O m}^{-2} \text{s}^{-1}$  and GEP is represented in dashed lines measured in  $\mu\text{mols CO}_2 \text{ m}^{-2} \text{s}^{-1}$  (upper left). PAR as measured in  $\mu\text{mols m}^{-2} \text{s}^{-1}$  is represented with dotted lines (upper right). Boxplots for H<sub>2</sub>O fluxes (lower left) and H<sub>2</sub>O fluxes normalized by PAR (lower right).

### 3.3 Hyperspectral Thermal Images

#### 3.3.1 Accuracy of Temperature Images

Image temperatures retrieved from the hyperspectral TIR airborne sensor (Telops *Hyper-Cam LW*) were compared with ground temperatures of the water filled pool at each overpass (Table IV-3). Overall, the airborne image temperatures agree very well with the ground temperatures with less than 0.35 K averaged absolute error, which is within the accuracy of the thermocouples (0.5 K, see above). The observed error increased with increasing temperature (*i.e.*,  $\Delta T = 0.19$  at 09:18 and  $\Delta T = 0.49$  at 12:51). In comparison, using a single band of the airborne hyperspectral scanner (AHS) Sobrino *et al.* (2006) were only able to retrieve surface temperatures with an accuracy of 2 K.

#### 3.3.2 Temperature-based Indices

Maps of temperature-based indices (Fig. IV-4) as well as boxplots (Fig. IV-5) show diurnal changes within the experimental site and treatments. It can be noted that the relative relationships (order) among the three treatments were consistent for all indicators and all flights (Fig. IV-5, Appendix Table IV-A1 for mean ( $\bar{x}$ ) and standard deviation (*sd*) of each index per flight and treatment).

For the CR plots,  $T_s$  was lowest in the early morning (9:18) with  $301.43 \pm 0.21$  K and increased by more than 6 K to  $307.53 \pm 0.44$  K in the late morning (10:48). From late morning to midday (12:51),  $T_s$  remained almost constant ( $307.99 \pm 0.14$  K).  $T_s - T_{air}$  was also lowest in the early morning ( $0.97 \pm 0.21$  K), increased to late morning ( $3.5 \pm 0.44$  K) and then slightly decreased by midday ( $2.3 \pm 0.14$  K). Finally, CWSI values also increased from early ( $0.08 \pm 0.04$ ) to late morning ( $0.44 \pm 0.2$ ), but decreased almost towards initial values during midday ( $0.11 \pm 0.04$ ). Diurnal courses of VG and KA treatment plots were similar to those of CR plots.

Table IV-3: Ground ( $T_{ground}$ ) and airborne ( $T_{airborne}$ ) temperatures of a water filled pool and their differences ( $\Delta T$ ) per TIR airborne overpass.

date	Flight	$T_{ground}$	$T_{airborne}$	$\Delta T$
11/06/2014 09:18	1	297.69	297.5	0.19
11/06/2014 10:48	2	299.41	299.79	0.38
11/06/2014 12:51	3	301.21	301.7	0.49

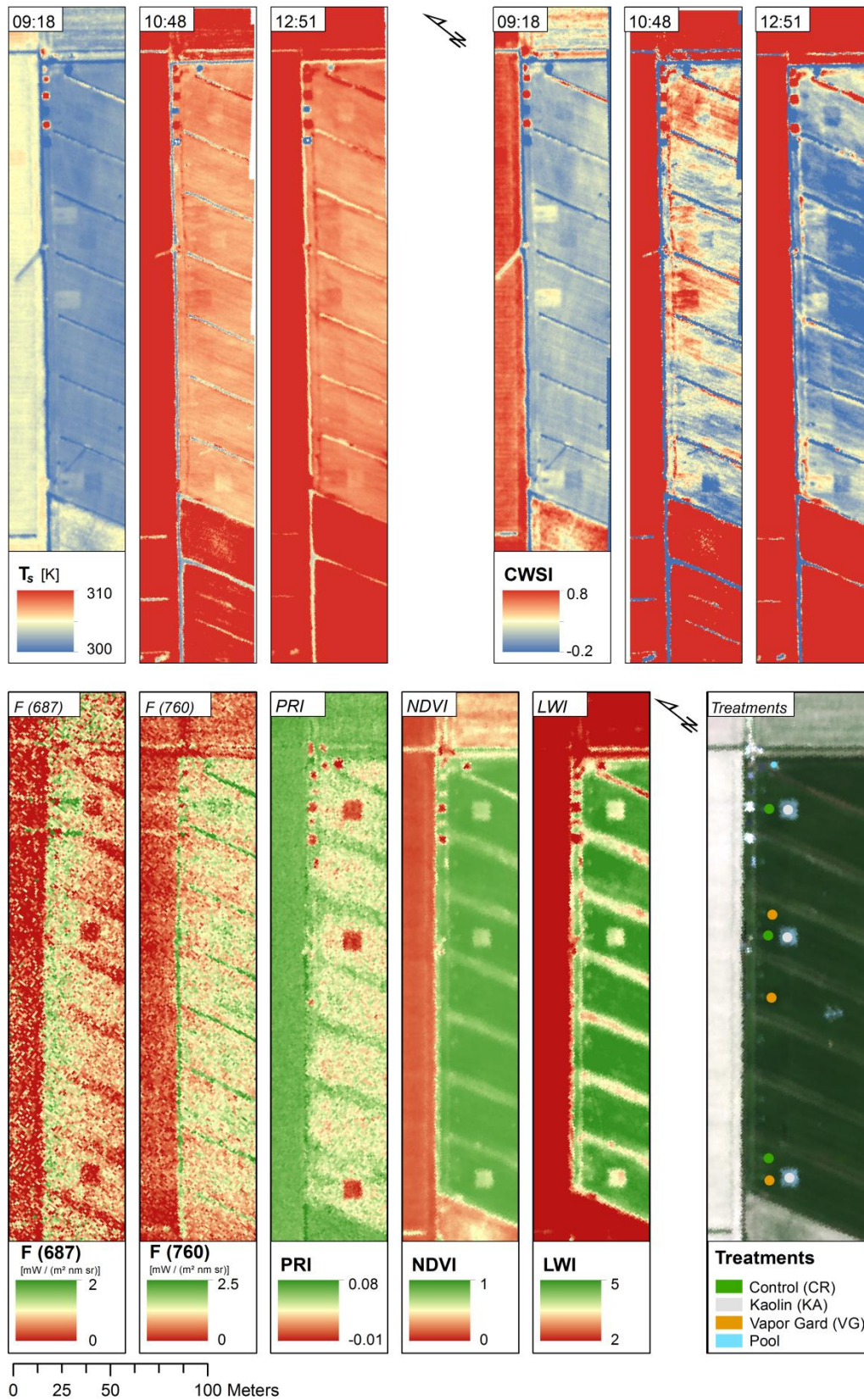


Fig. IV-4: Diurnal  $T_s$  [K] and CWSI maps at 11<sup>th</sup> June (top),  $F_{687}$ ,  $F_{760}$ , PRI, NDVI and LWI maps of the same day (11<sup>th</sup> June, 14:52 CEST) (bottom left), and locations of the treatments (bottom right).

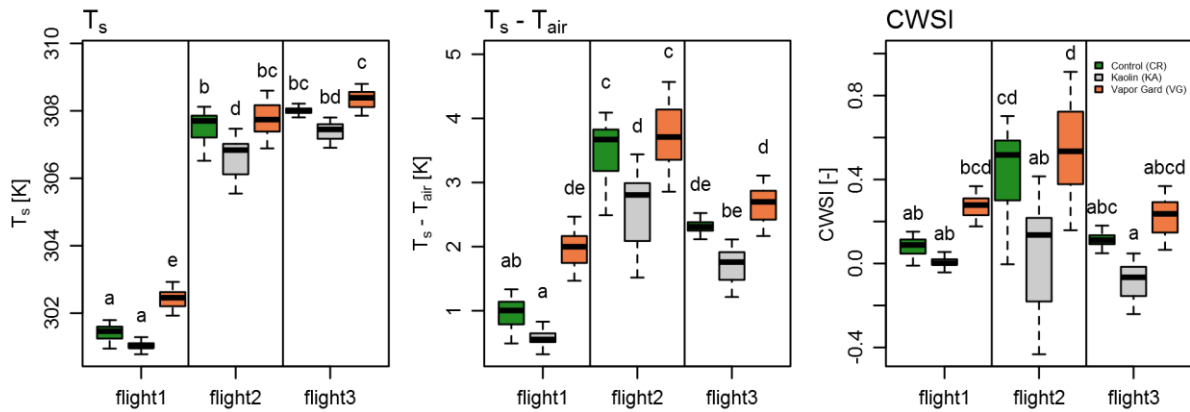


Fig. IV-5: Boxplots of the different treatments (CR, KA, VG) at the three overpasses for  $T_s$ ,  $T_s - T_{air}$  and CWSI. Different letters indicate significant differences ( $^*p \leq 0.05$ ).

A distinct pattern between all temperature-based indices was recognized (Fig. IV-5), with KA was showing the lowest values in comparison to CR, whereas VG had the highest for all three flights (e.g.,  $T_s$  (KA) = 301.03 K,  $T_s$  (CR) = 301.43 K and  $T_s$  (VG) = 302.42 K at early morning). A pairwise comparison of the treatments (see Tukey's HSD in Appendix Table IV-A2) revealed that in the early morning VG and CR were significantly different for  $T_s$  and  $T_s - T_{air}$ , but not for CWSI ( $p = 0.59$ ). However, VG plots could be easily distinguished from CR and surroundings by visual interpretation of the CWSI map at early morning (Fig. IV-4). Additionally, the boxplots of CWSI also showed a distinct difference between CR and VG treatment at early morning. Thus, all temperature-based indices showed considerably increased values for the VG treatment at early morning. By contrast, for the late morning and midday flights VG had no significant effect ( $p > 0.05$ ) to any temperature-based index. Similar results were observed for KA, where for all temperature-based indices only at late morning KA was significantly different to CR.

### 3.3.3 VNIR/SWIR Indices and Sun-induced Fluorescence (SIF)

Fig. IV-6 shows the mean reflectance spectra from *HyPlant*'s dual-channel module (0.38 – 2.5  $\mu\text{m}$ ) per treatment and flight. The reflectance spectra for VG plots were very similar to CR, which is also confirmed by the boxplots (Fig. IV-7) as well as by the  $p$ -values (see Appendix Table IV-A3). Further, no visual differences between VG and CR were recognized in the *HyPlant* images from the maps (Fig. IV-4). In contrast, KA mean reflectance spectra had an overall higher reflectance for all wavelengths. Especially, in the visible spectral range (0.38 – 0.7  $\mu\text{m}$ ) KA displayed up to 10% higher (about 5 times larger) reflectance values, underpinning the properties of KA to increase plant albedo.



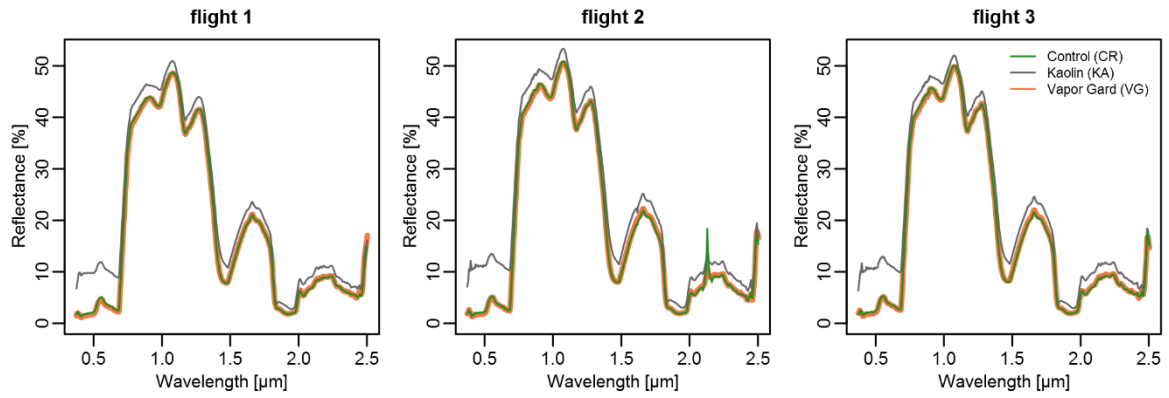


Fig. IV-6: VNIR/SWIR mean reflectance spectra from *HyPlant*'s dual-channel module.

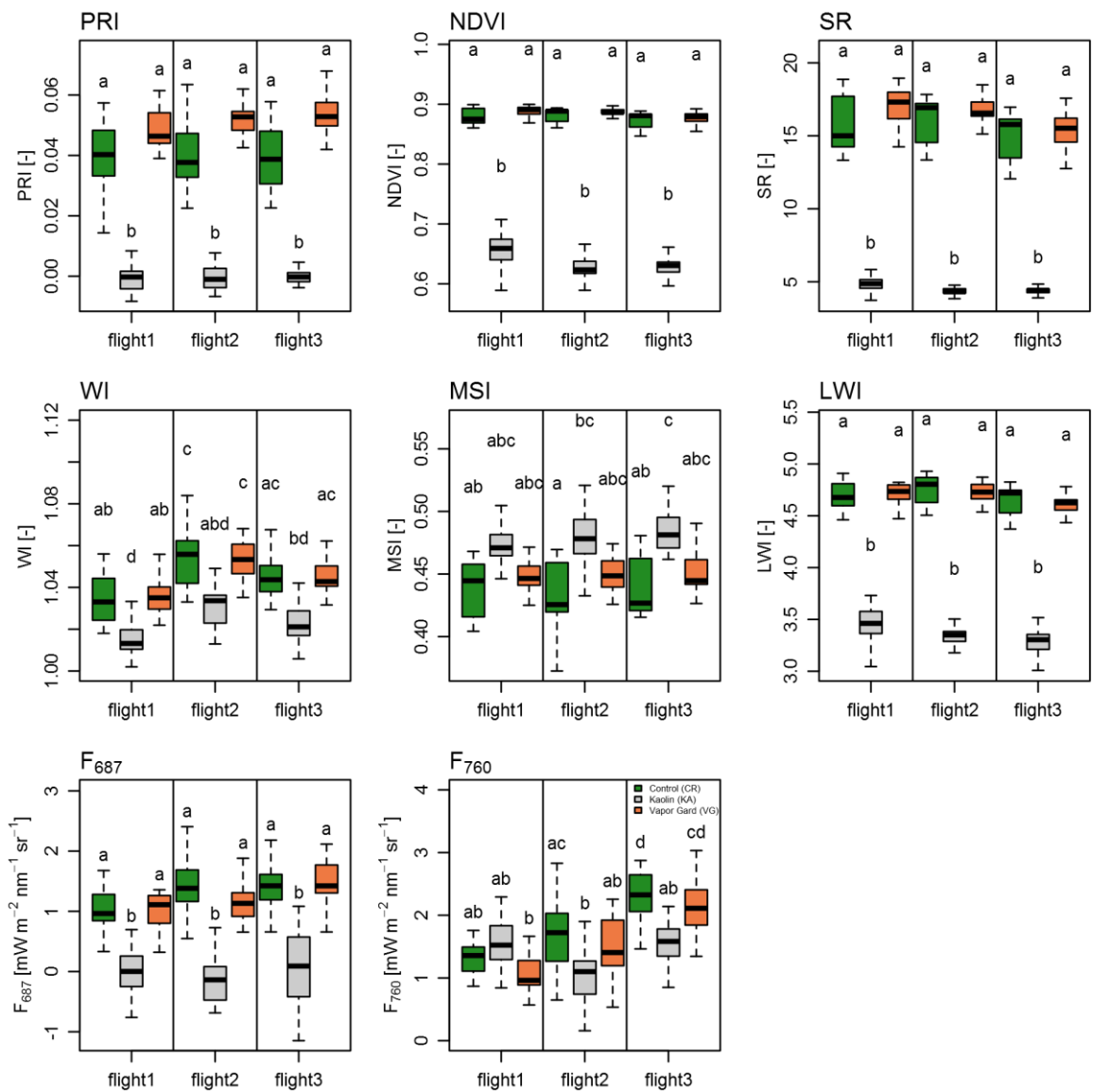


Fig. IV-7: Boxplots of the different treatments (CR, KA, and VG) at three *HyPlant* overpasses for VNIR/SWIR based indices and  $F_{687}$  and  $F_{760}$ . Different letters indicate significant differences ( $p \leq 0.05$ ).

To test for any structural changes that may have occurred because of plant growth or stress (*e.g.*, leaf rolling, leaf angle) in the course of the campaign, we evaluated the structural indices NDVI and SR that were derived from VNIR/SWIR spectra over the three acquisitions. Both structural indices were not significantly different at the three airborne overpasses (Fig. IV-7), as shown by a pairwise Tukey's HSD post-hoc test (see Appendix Table IV-A3). The similarity of all three NDVI and SR values suggests stable data collection (good repeatability). Again, NDVI and SR behaved in a similar manner over both chemical agents (Fig. IV-7). They reacted highly significant to the fact that the KA increased overall reflectance (see above) in comparison to CR plots ( $p < 0.001^{***}$ , see Appendix Table IV-A3). In contrast, VG had no significant effect on the grass surface reflectance in comparison to CR (VG and CR are almost identical, Fig. IV-6). Further, VG had no significant effect on NDVI and SR as reported by very small mean differences between VG and CR (*e.g.*, 0.01 at early morning and even 0 for late morning and midday for NDVI, see Appendix Table IV-A1).

The performance of reflectance based VIs to detect plant (water) stress was tested using PRI, as well as water content related indices (*i.e.*, WI, LWI, MSI). As KA greatly changed the reflectance in the green spectral range (Fig. IV-6), the PRI was also greatly affected in comparison to CR. No significant differences between VG and CR plots could be recognized for PRI. However, PRI values are slightly increased in the VG treatment (Fig. IV-7). Furthermore, the water absorption bands at 0.97 and 1.45  $\mu\text{m}$ , which were used in the WI and LWI, respectively, were also highly sensitive to the KA treatment compared to CR. In fact, the KA plots could be easily distinguished from the surrounding areas looking at PRI-, NDVI- and LWI-maps (Fig. IV-4). Just MSI was less sensitive and only indicated significant differences for late morning and midday.

As a fundamental difference to reflectance based VI, SIF is an emitted radiation. Therefore, SIF is not directly affected by changing the reflectance properties of grass surface by chemical agent, but rather indirectly by induced plant photochemical changes.  $F_{687}$  shows slightly negative values for KA. However, the overall pattern of  $F_{687}$  and  $F_{760}$  display consistently lower values in KA plots (Fig. IV-7), except for  $F_{760}$  at the first *HyPlant* overpass. The differences between KA and CR were up to 1.6  $\text{mW nm}^{-1} \text{sr}^{-1} \text{m}^{-2}$  for  $F_{687}$  and 0.7  $\text{mW nm}^{-1} \text{sr}^{-1} \text{m}^{-2}$  for  $F_{760}$  during the second *HyPlant* overpass. Thus,  $F_{687}$  and  $F_{760}$  of KA plots are significantly different in comparison to CR (see Appendix Table IV-A3). In contrast, VG has no effect on  $F_{687}$  and  $F_{760}$  compared to CR.

## 4 Discussion

As shown by the results of the meteorological measurements (*i.e.*, SWC, VPD; Fig. IV-2) no actual plant water stress occurred during the experiment due to sufficient water supply from the soil. Nevertheless, the VG treatment had a modest but clearly measurable effect on H<sub>2</sub>O flux relative to PAR (reduction of relative transpiration of grass by 20% in average) as well as on CO<sub>2</sub> flux (reduction by nearly 21%). This proved that real, but rather mild effects on transpiration and CO<sub>2</sub> uptake arose from the VG treatment.

The diurnal change of  $T_s$  can be explained by the effects of plant transpiration. At late morning, as a consequence of increasing net radiation and VPD (Fig. IV-2), plant transpiration and thus, evaporative cooling increased and prevented a rise in  $T_s$ . Due to the same process,  $T_s - T_{air}$  also increased from early to late morning. However,  $T_s - T_{air}$  slightly decreased from late morning to midday (Fig. IV-5) because  $T_s$  remained constant due to higher transpiration rate while  $T_{air}$  continued to rise due to increased net radiation (Fig. IV-2). Further, the diurnal changes in CWSI demonstrated the same effect as described for  $T_s - T_{air}$ . Since the upper boundary ( $T_{dry}$ ) was determined by adding 5 K to the current  $T_{air}$ ,  $T_{dry}$  increased in the same manner as  $T_{air}$  resulting in overall lower CWSI values at midday. Negative CWSI values in KA resulted from the fact that  $T_s$  was lowest for KA and the lower boundary ( $T_{wet}$ ) was determined by the coolest 5 % of CR plots, which were partly warmer than KA.

Indeed, the mild physiological manipulations through the chemical agents (*i.e.*, 20% reduced transpiration in VG) only induced very small effects to temperature-based indices. VG reduced plant transpiration and induced symptoms of water stress, *i.e.*, an overall increase in  $T_s$  compared to CR plots. Contrary, the KA treatment highly increased the plant albedo, and thus reduced the overall energy uptake by the plant causing a decrease in  $T_s$ . In this study, only absolute temperature differences of less than 1.0 K were observed between the treatments. Notwithstanding, these minor differences could be distinguished by TIR remote sensing, as observed by a distinct pattern for all temperature-based indices (Fig. IV-5). These results demonstrate that TIR remote sensing indices were sensitive to small  $T_s$  differences induced by the chemical treatments. In comparison, a recent study has demonstrated that temperature-based indices can detect water stress from airborne multispectral TIR data under distinct water deficit conditions with large temperature difference of up to 4.7 K (Panigada *et al.*, 2014; Rossini *et al.*, 2015b). However, our results indicate that the TIR-based indices can be used to detect minor or moderate level of water stress. It is well known that the leaf temperature can be increased by various stressors including water deficit and diseases (Chiwaki *et al.*, 2005; Nilsson, 1991). Therefore, TIR imaging of high spatial and spectral resolution greatly contributes to the detection and/or quantification of the physiological anomaly caused by abiotic and biotic stresses.

Basically, canopy reflectance spectra in VNIR/SWIR are affected by water content, pigment content and composition (chlorophyll, carotenoid, xanthophyll), leaf internal structure, and canopy geometry (*e.g.*, Jacquemoud *et al.*, 2009). Thus, in turn, the stress symptoms are detected via the spectral change associated to the response of these physiological traits to environmental stressors. In this study, we assumed little change in water and chlorophyll content as well as in structure among CR, KA and VG treatments. The response of all analysed VIs (PRI, NDVI, WI, LWI, MSI) that are closely related to either structure, water and pigment, or physiological functioning showed little difference between CR and VG. This fact suggests the consistency of these VIs in various conditions. On the other hand, the significant differences found between CR and KA imply that care should be taken in the application of these VIs to some specific leaf surface conditions (*e.g.*, after yellow-sand dust and volcanic ash fall). In such cases, the surface reflectance spectra could be altered (as in KA treatment) without any physiological changes. Generally, the applicability of normalized VIs is based on the consistent relationship of multiple bands to the internal physiological changes. Accordingly, alteration of the relationship between spectral bands (*i.e.*, shape of spectra) caused by external factors would strongly hamper the consistency of VIs. In fact, KA treatment increased plant albedo, but did not increase reflectance at the same ratio in all wavebands. Thus, the significant difference in KA was not caused by physiological changes, but rather indicated abnormal alteration of reflectance spectra. Since reflectance spectra is altered unusually by plant diseases such as powdery mildew and rust diseases (*e.g.*, Ashourloo *et al.*, 2014), similar unusual changes of VIs as in KA would be detected by hyperspectral measurement. Therefore, our results from the unique experimental design provide useful insights on the consistency and usefulness of hyperspectral reflectance measurements, especially for discrimination of causes of detected changes.

According to previous research (Meroni *et al.*, 2009), SIF decreases with a reduction of photosynthesis under high light and stressed conditions (*e.g.*, shortage in water availability). However, in our experiment, SIF indices showed no significant difference between VG and CR treatments while the photosynthetic efficiency should have been lowered in VG plots because of reduced H<sub>2</sub>O and CO<sub>2</sub> fluxes (as proofed by chamber flux measurements). This fact suggests that either the stress was too subtle to reduce photosynthesis, and thus had no influence on the efficiency of photosynthetic light reaction or that the used SIF indices were not sufficiently sensitive to detect the slight photosynthesis reduction. On the other hand, the significant reduction in SIF indices ( $F_{687}$ ,  $F_{760}$ ) found under KA treatment is proportional related to the reduced amount of APAR by increasing surface reflectance, and thus lowered the photosynthetic rate. Nevertheless, it is not clear whether the reduction of SIF was directly related to the change of photosynthetic photon use efficiency because the fraction of APAR (fAPAR) as well as water and chlorophyll content remained unchanged. In addition, one have to be careful about appropriate conclusion about the attenuation of SIF and incident PAR at leaf surfaces. It is still not obvious how SIF can be related to photochemistry and a unique relationship between SIF and photochemical efficiency is challenging (Porcar-Castell *et al.*, 2014). The slightly negative values in  $F_{687}$

originate from uncertainties in the  $F_{687}$  retrieval due to the largely modified surface reflectance by the KA treatment. However, our results clearly show that the subtle change in SIF indices for KA treatments was detected by the *HyPlant* sensor. Therefore, optical hyperspectral techniques bear the ability to detect both rapid photochemical change (*e.g.*, photon use efficiency) and integrated physiological change (*e.g.*, photosynthetic capacity), and to infer the causes for the changes by using multiple wavelengths. Since remotely sensed SIF is affected by the non-linear interactions of photochemical, physiological and biophysical factors, further experimental studies in combination with process-based modelling (*e.g.*, Verrelst *et al.*, 2016) are needed for both scientific and industrial applications.

In fact, the application of the results presented here to real water stress occurrence in natural conditions is limited due to the nature of the experimental design. Due to logistical challenges related to synchronous availability of both sensor systems *HyPlant* and *HyperCam-LW* and to setting up an experiment that leads to real water stress, chemical agents (*i.e.*, VG and KA) were used to simulate plant water stress symptoms. Additionally, a synchronised flight plan of both airborne sensors could not be implemented which complicated the comparison of TIR *versus* VNIR/SWIR and SIF water stress indices. Notwithstanding, the study allowed us to deduce new findings about the interplay of different indices in relation to water stress symptoms at the airborne level.

Comparing the performance of TIR, VNIR/SWIR and SIF for detecting water stress symptoms, temperature-based indices were most sensitive. Notwithstanding, biotic and abiotic plant stressors (*e.g.*, water stress, heat stress, diseases) often occur simultaneously and cause similar plant physiological responses (*e.g.*, increase in plant temperature, reduced photosynthetic efficiency, change in canopy structure). Therefore, multi-sensor and multi-temporal approaches have a great potential to not only obtain useful information about the current plant status but also on the causes of biophysical, physiological and photochemical changes. Especially airborne remote sensing with its high spatial and temporal resolutions can bridge the gap between *in situ* and satellite observations.

## 5 Conclusion

In this paper we examined the performance of different airborne hyperspectral remote sensing approaches (*i.e.*, TIR, VNIR/SWIR and SIF) for detecting water stress symptoms over a commercial grass farm. Water stress symptoms were induced by modifying plant characteristics with two chemical agents (*i.e.*, VG and KA). From the VG treatment, real but rather mild effects on plant transpiration and CO<sub>2</sub> uptake arose. From the KA treatment, plant albedo was increased.

Table IV-4: Observed effects of treatments on spectral domains.

Treatment	Effect on VNIR/SWIR	Effect on TIR	Effect on SIF
CR	Normal	Normal	Normal
VG	Indices sensitive to leaf water content and chlorophyll content remained unchanged.	$T_s$ was increased due to reduced transpiration.	SIF indices remained unchanged probably due to too subtle changes in photosynthetic efficiency
KA	Indices were highly sensitive to an overall increase in reflectance and corresponding reduction of APAR.	$T_s$ was reduced due to a decrease in absorbed radiation.	SIF indices were reduced due to decreased overall available absorbed energy (APAR)

The most important finding of this study is that TIR based indices were more sensitive compared to VNIR/SWIR indices and SIF indices for the detection of water stress symptoms. Further, the assessment of the observed effects of the treatments on the different indices is summarised in Table IV-4. First,  $T_s$  was increased in VG plots due to decreased plant transpiration. Similarly, also the diurnal changes in temperature-based indices were caused by plant transpiration. Second, SIF indices were not affected in VG plots, because the changes in photosynthetic efficiency were too subtle. Third, VNIR/SWIR indices were also not affected in VG plots due to unchanged leaf biochemical components. Fourth, KA treatment increased plant albedo, reduced APAR resulting in a reduction of  $T_s$ , in a reduction of SIF, and in a change of VNIR/SWIR indices (see Table IV-4 for details). Finally, a multi-sensor approach not only provides useful information about the current plant status but also on the causes of biophysical, physiological and photochemical changes.

## Acknowledgements

Funding for this research was provided by the Fonds National de la Recherche (FNR) of Luxembourg, particularly through the PLANTSSENS project grant (Detection of plant stress using advanced thermal and spectral remote sensing techniques for improved crop management, C13/SR/5894876) and the FNR-DFG CAOS-2 project grant (Catchments as Organised Systems, INTER/DFG/14/02).

The development of *HyPlant* was supported by the large scale investment grant of the Forschungszentrum Jülich. Campaign activities were funded by the European Space Agency (ESA) in the frame of the FLEX-EU activity (ESA Contract No. 4000107143/12/NL/FF/If). Further support was provided by the SFB/TR32 “Patterns in Soil-Vegetation-Atmosphere Systems: Monitoring, Modelling, and Data Assimilation”—subproject D2 ([www.tr32.de](http://www.tr32.de)), funded by the Deutsche Forschungsgemeinschaft (DFG) and the German Plant Phenotyping Network (DPPN), funded by the BMBF.

This study was also supported in part by JSPS and CSTI-SIP, Japan. Furthermore, we would like to thank everyone who took part in the campaign, in particular for the airborne operation of the *Hyper-Cam LW* (Franz Kai Ronellenfitsch, LIST), for ground measurements and data processing (Gilles Rock, Karolina Sakowska, Marcin Stróżecki, Micol Rossini, Marco Celesti, Anke Schickling, Patrick Rademske, Alexander Damm, Francisco Pinto, Andreas Burkart and all the others) and for the campaign coordination (Dirk Schüttemeyer, ESA).

## Appendix

Table IV-A1: Descriptive statistics: mean ( $\bar{x}$ ) and standard deviation ( $sd$ ) for every index per flight and treatment (Control (CR), Kaolin (KA) and Vapor Gard® (VG))

Flight	Treat.	$\bar{x} / sd$	T <sub>s</sub>	T <sub>s</sub> - T <sub>air</sub>	CWSI	PRI	NDVI	SR	WI	MSI	LWI	F <sub>687</sub>	F <sub>760</sub>
1	CR	$\bar{x}$	301.43	0.97	0.08	0.04	0.88	15.7	1.04	0.44	4.7	1.08	1.29
		$sd$	0.21	0.21	0.04	0.01	0.01	1.75	0.01	0.02	0.12	0.40	0.25
	KA	$\bar{x}$	301.03	0.57	0.01	0	0.65	4.82	1.01	0.47	3.43	0.03	1.52
		$sd$	0.1	0.1	0.02	0	0.03	0.46	0.01	0.02	0.18	0.40	0.39
	VG	$\bar{x}$	302.42	1.96	0.27	0.05	0.89	17.1	1.04	0.45	4.71	1.02	1.07
		$sd$	0.23	0.23	0.04	0.01	0.01	1.1	0.01	0.01	0.09	0.29	0.26
2	CR	$\bar{x}$	307.53	3.5	0.44	0.04	0.88	16.14	1.05	0.43	4.76	1.48	1.66
		$sd$	0.44	0.44	0.20	0.01	0.01	1.39	0.01	0.03	0.13	0.55	0.48
	KA	$\bar{x}$	306.65	2.62	0.05	0	0.62	4.33	1.03	0.47	3.33	-0.13	1.02
		$sd$	0.51	0.51	0.22	0	0.02	0.28	0.01	0.02	0.12	0.36	0.46
	VG	$\bar{x}$	307.75	3.72	0.54	0.05	0.89	16.65	1.05	0.45	4.73	1.16	1.45
		$sd$	0.48	0.48	0.21	0.01	0.01	0.9	0.01	0.01	0.09	0.28	0.42
3	CR	$\bar{x}$	307.99	2.3	0.11	0.04	0.87	15.07	1.04	0.44	4.65	1.38	2.28
		$sd$	0.14	0.14	0.04	0.01	0.01	1.55	0.01	0.02	0.13	0.43	0.39
	KA	$\bar{x}$	307.41	1.72	-0.08	0	0.63	4.4	1.02	0.48	3.29	0.09	1.55
		$sd$	0.23	0.23	0.08	0	0.02	0.34	0.01	0.02	0.12	0.61	0.34
	VG	$\bar{x}$	308.34	2.65	0.22	0.05	0.88	15.5	1.04	0.45	4.6	1.44	2.12
		$sd$	0.24	0.24	0.08	0.01	0.01	1.15	0.01	0.01	0.09	0.40	0.46

Table IV-A2:  $p$ -values (level of statistical significance: \*\*\* $p < 0.001$ , \*\* $p < 0.01$ , \* $p < 0.05$ ) of Tukey's HSD pairwise comparison and mean differences of treatments (CR, KA, VG) for temperature-based indices at all three *Hyper-Cam LW* overpasses.

Index	Comparison		Mean Dif- ference	$p$ -value
T <sub>s</sub>	1.CR	1.KA	0.4	0.7334
		1.VG	0.99	0.01*
	2.CR	2.KA	0.86	0.04*
		2.VG	0.24	0.9765
	3.CR	3.KA	0.58	0.3081
		3.VG	0.37	0.8139
T <sub>s</sub> - T <sub>air</sub>	1.CR	1.KA	0.4	0.7337
		1.VG	0.99	0.01*
	2.CR	2.KA	0.86	0.04*
		2.VG	0.24	0.9766
	3.CR	3.KA	0.58	0.3085
		3.VG	0.37	0.8141
CWSI	1.CR	1.KA	0.08	1
		1.VG	0.19	0.59
	2.CR	2.KA	0.38	0.02*
		2.VG	0.11	0.963
	3.CR	3.KA	0.19	0.602
		3.VG	0.12	0.940



Table IV-A3:  $p$ -values (level of statistical significance: \*\*\*  $p < 0.001$ , \*\*  $p < 0.01$ , \*  $p < 0.05$ ) of Tukey's HSD pairwise comparison and mean differences of treatments (CR, KA, VG) for VNIR/SWIR based indices and  $F_{687}$  and  $F_{760}$  at three *HyPlant* overpasses.

Index	Comparison		Mean Difference	$p$ -value
PRI	1.CR	1.KA	0.04	<0.001***
		1.VG	0.01	0.65
	2.CR	2.KA	0.04	<0.001***
		2.VG	0.01	0.18
	3.CR	3.KA	0.04	<0.001***
		3.VG	0.01	0.11
NDVI	1.CR	1.KA	0.23	<0.001***
		1.VG	0.01	0.99
	2.CR	2.KA	0.26	<0.001***
		2.VG	0	1
	3.CR	3.KA	0.25	<0.001***
		3.VG	0	1
SR	1.CR	1.KA	10.9	<0.001***
		1.VG	1.34	0.74
	2.CR	2.KA	11.74	<0.001***
		2.VG	0.57	1
	3.CR	3.KA	10.61	<0.001***
		3.VG	0.39	1
WI	1.CR	1.KA	0.02	<0.01**
		1.VG	0	1
	2.CR	2.KA	0.02	<0.01**
		2.VG	0	1
	3.CR	3.KA	0.02	<0.01**
		3.VG	0	1
MSI	1.CR	1.KA	0.04	0.16
		1.VG	0.01	1
	2.CR	2.KA	0.04	0.04*
		2.VG	0.02	0.92
	3.CR	3.KA	0.05	0.02*
		3.VG	0.01	0.95
LWI	1.CR	1.KA	1.28	<0.001***
		1.VG	0	1
	2.CR	2.KA	1.42	<0.001***
		2.VG	0.02	1
	3.CR	3.KA	1.36	<0.001***
		3.VG	0.05	1
$F_{687}$	1.CR	1.KA	1.02	<0.001***
		1.VG	0.07	1
	2.CR	2.KA	1.57	<0.001***
		2.VG	0.28	0.81
	3.CR	3.KA	1.28	<0.001***
		3.VG	0.05	1
$F_{760}$	1.CR	1.KA	0.22	0.88
		1.VG	0.24	0.84
	2.CR	2.KA	0.63	0.02*
		2.VG	0.22	0.88
	3.CR	3.KA	0.70	<0.01**
		3.VG	0.11	1



# Chapter V

## **Plant Species Discrimination using Emissive Thermal Infrared Imaging Spectroscopy**

*Int. J. Appl. Earth Obs. Geoinf.* 53,

*December 2016, 16 – 26.*

DOI: 10.1016/j.jag.2016.08.005

Gilles Rock, Max Gerhards, Martin Schlerf, Christoph Hecker  
and Thomas Udelhoven

© 2016 Elsevier B.V. All rights reserved.

The following manuscript is a copy of the final version of the accepted manuscript. The paper has been through peer review, but it has not been subject to copy-editing, proofreading and formatting added by the publisher. The contribution of Max Gerhards to this scientific paper was the development and implementation of the experimental setup including sample preparation, measurement setup and data acquisition. In addition, Max Gerhards was involved in processing and analysing the data.

The version-of-record can be accessed at:

<http://www.sciencedirect.com/science/article/pii/S0303243416301350>

## Abstract

Discrimination of plant species in the optical reflective domain is somewhat limited by the similarity of their reflectance spectra. Spectral characteristics in the visible to shortwave infrared (VSWIR) consist of combination bands and overtones of primary absorption bands, situated in the Thermal Infrared (TIR) region and therefore resulting in broad spectral features. TIR spectroscopy is assumed to have a large potential for providing complementary information to VSWIR spectroscopy. So far, in the TIR, plants were often considered featureless. Recently and following advances in sensor technology, plant species were discriminated based on specific emissivity signatures by Ullah and co-workers (2012) using directional-hemispherical reflectance (DHR) measurements in the laboratory. Here we examine if an accurate discrimination of plant species is equally possible using emissive thermal infrared imaging spectroscopy, an explicit spatial technique that is faster and more flexible than non-imaging measurements.

Hyperspectral thermal infrared images were acquired in the 7.8 to 11.56  $\mu\text{m}$  range at 40 nm spectral resolution (@10 $\mu\text{m}$ ) using a TIR imaging spectrometer (Telops *Hyper-Cam LW*) on seven plants each, of eight different species. The images were radiometrically calibrated and subjected to temperature and emissivity separation using a spectral smoothness approach. First, retrieved emissivity spectra were compared to laboratory reference spectra and then subjected to species discrimination using a random forest classifier. Second, classification results obtained with emissivity spectra were compared to those obtained with VSWIR reflectance spectra that had been acquired from the same leaf samples.

In general, the mean emissivity spectra measured by the TIR imaging spectrometer showed very good agreement with the reference spectra (average Nash-Sutcliffe-Efficiency Index = 0.64). In species discrimination, the resulting accuracies for emissivity spectra are highly dependent on the signal-to-noise ratio (SNR). At high SNR, the TIR data (Overall Accuracy (OAA) = 92.26 %) outperformed the VSWIR data (OAA = 80.28 %).

This study demonstrates that TIR imaging spectroscopy allows for fast and spatial measurements of spectral plant emissivity with accuracies comparable to laboratory measurement. This innovative technique offers a valuable addition to VSWIR spectroscopy as it provides complimentary information for plant species discrimination.

## 1 Introduction

Vegetation mapping and species discrimination are key requirements of studies focusing on ecosystem monitoring and development. The time consuming traditional methods of in-field mapping are optimized by remote sensing data collection, which facilitates the economic acquisition of repeated data products allowing for large area studies of vegetation cover (Langley *et al.*, 2001). Remote sensing based vegetation mapping has been achieved in different ways including multi-spectral, hyperspectral, and multi-temporal classification (Langley *et al.*, 2001; White *et al.*, 2005).

Multispectral and hyperspectral systems in the visible to shortwave infrared (VSWIR; 0.4 – 2.5  $\mu\text{m}$ ) spectral range demonstrated their capability in plant discrimination (Govender *et al.*, 2007; Ustin and Gamon, 2010). This is caused by the fact that the spectral features in the VSWIR are mostly defined by plant constituents such as pigments, leaf water content and other biochemicals like lignin, cellulose (Asner, 1998). Vegetation classification is facilitated by the extraction of distinct and characteristic spectral features in the VSWIR, such as green peak, red edge, and water absorption bands (Asner, 1998; Govender *et al.*, 2007).

While VSWIR spectra have been widely used for many different applications at laboratory to spaceborne levels, the use of the thermal infrared spectral domain (TIR; 8 – 14  $\mu\text{m}$ ) is not as widely spread. The reasons for this are the lack of available spectrometers and the general low SNR in combination with subtle spectral features, which had limited the benefits of TIR spectrometers in the past (Ribeiro da Luz and Crowley, 2007). However, sensor technology has improved in the past years and high resolution spectrometers became available for laboratory, in-situ and even airborne applications. The increasing availability for commercial TIR imaging spectrometers (*e.g.*, Telops *Hyper-Cam LW*, Itres TASI-600, Specim AisaOWL) in the last years underline the growing scientific community and the rising number of studies using thermal infrared imaging spectroscopy (Danilina *et al.*, 2012; Vaughan *et al.*, 2003).

Spectral characteristics in the VSWIR consist of combination bands and overtones of primary absorption bands resulting in broad spectral features. As many of the fundamental absorption bands are situated in the TIR region, thermal infrared spectroscopy is assumed to have a large potential for providing complementary information to VSWIR spectroscopy, *e.g.* identification of vegetation and the quantification of leaf constituents (Ribeiro da Luz, 2006; Silverstein *et al.*, 2005). Despite the general meaning, a few authors demonstrated that vegetation spectra in the TIR are different from blackbody (BB) signatures (Salisbury and D'Aria, 1992; Salisbury, 1986). Moreover, just very recently it could be impressively demonstrated that plant species are discriminable in the TIR (Ribeiro da Luz, 2006; Ullah *et al.*, 2012b). Ullah *et al.* (2012b) and Fabre *et al.* (2011) showed that the mid-wave infrared (MWIR; 3 – 5  $\mu\text{m}$ ) is sensitive towards leaf water content and Buitrago *et al.* (2016) even demonstrated that

multiple types of stress could be spectrally identified. These studies were laboratory-based directional hemispherical reflectance (DHR) measurements of single leaves. The results from active DHR spectroscopy can be adapted to passive acquisition techniques used for remote sensing purposes considering Kirchhoff's law. However, these laboratory measurements are time consuming (40 min. or longer for each analysis) and only allow for a single, non-imaging leaf measurement at a time (Hecker *et al.*, 2011).

Ribeiro da Luz and Crowley (2007) collected in-situ vegetation emissivity spectra using a passive non-imaging field spectrometer and recognized spectral features identified in laboratory measurements carried out before. Beyond this, new developments in emissive TIR spectroscopy focusing on hyperspectral TIR cameras offer the possibilities for fast and spatial measurements of plant emissivity. Nevertheless, the accuracy of such measurements and their suitability for species discrimination at field conditions has not been tested yet.

## 2 Objectives

The overall aim of this study was to investigate if plant species discrimination is feasible using emissive TIR imaging spectroscopy. Specific objectives were to: (i) compare emissivity spectra from a passive emissive imaging spectrometer with reference spectra from laboratory DHR measurements, (ii) classify plant species using the emissivity spectra as input, (iii) compare classification accuracies of emissivity spectra with reflectance spectra from a traditional VSWIR spectrometer, (iv) demonstrate the ability of identifying spatial heterogeneities using a TIR imaging spectrometer and (v) perform a systematic investigation on the effect of SNR on classification results.

Table V-1: The studied plant species with their common name, Latin name, sample size and short code.

Common name	Latin name	Sample size (plants x leaves)	Short code
Vine Peach	<i>Prunus persica</i>	35 (7x5)	<i>Pp</i>
Sweetgum	<i>Liquidambar styraciflua</i>	35 (7x5)	<i>Ls</i>
Redosier dogwood	<i>Cornus sericea</i>	35 (7x5)	<i>Cs</i>
Maidenhair tree	<i>Ginkgo biloba</i>	35 (7x5)	<i>Gb</i>
Cherry laurel	<i>Prunus lauracerasus</i>	35 (7x5)	<i>Pl</i>
Rhododendron	<i>Rhododendron repens</i>	35 (7x5)	<i>Rr</i>
David viburnum	<i>Viburnum davidii</i>	35 (7x5)	<i>Vd</i>
Norway maple	<i>Acer platanoides</i>	35 (7x5)	<i>Ap</i>

### 3 Methods

During summer 2013, an experiment was carried out in the greenhouse facilities at Trier University. The greenhouse setup allowed plants to be grown under controlled conditions and thermal hyperspectral measurements to be performed next to the greenhouse under clear sky conditions.

#### 3.1 Species Discrimination Experiment

Eight different plant species were selected for this study (Table V-1). Five of the eight species are identical to those used by Ullah *et al.* (2012b) and represent a wide range of leaves' properties (*i.e.*, colour, thickness, structure, shape) and different canopy structures with expected variations in emissivity. This species setup allows for direct comparison with the results of Ullah *et al.* (2012b) who assessed plant species discrimination in the thermal spectral region in a laboratory experiment using active DHR spectroscopy.

Seven individual plants from each species were obtained from a local nursery ( $n = 56$ ). Emissivity measurements of five leaves were taken of each plant, resulting in a total amount of 280 emissivity spectra. The measurements for the species discrimination experiment took place on August 21<sup>st</sup> and 22<sup>nd</sup> 2013 from 10:30 to 18:00 local time.

#### 3.2 Thermal Infrared

##### 3.2.1 Thermal Infrared Spectroscopy

Infrared spectroscopy is an analytical technique that is based on vibrational motions within molecules of matters that interact with electromagnetic radiation (Christensen *et al.*, 2000; Hecker *et al.*, 2011). A molecule starts vibrating at fundamental frequency when it is stimulated by absorption of specific electromagnetic radiation. The frequency of such molecular vibration is characteristic for a specific functional group and depends on the atoms' masses and the molecule's geometry. If a molecule absorbs higher amounts of energy, the molecule is excited in overtones or combinations of fundamental vibration frequencies (Wilson *et al.*, 1955). Whereas NIR and SWIR radiation (0.8 – 2.5  $\mu\text{m}$ ) can excite molecules to overtone vibrations, the mid-wave and longwave infrared spectral region (2.5 – 25  $\mu\text{m}$ ) may be used to study the fundamental vibrations and associated molecular structures and can be used as a diagnostic tool (Christensen *et al.*, 2000; Salisbury, 1986).

The fundamental vibration frequencies of many constituents composing the superficial epidermal layer of plant leaves are situated in the TIR spectral region. Among others, cellulose, hemicellulose, varieties of pectin and aromatic compounds have characteristic features in the 8 – 12  $\mu\text{m}$  spectral range (Elvidge, 1988; Ribeiro da Luz and Crowley, 2007; Riederer and Muller, 2006; Ullah *et al.*, 2012a). This is why TIR spectroscopy is assumed to have large potential for identification of species specific surface compositions and species discrimination.

While several techniques allow the acquisition of thermal infrared spectroscopy data, this study focuses on a passive acquisition technique. Passive measurements of emitted thermal infrared radiation always require a thermal contrast between the sample and the environment to distinguish the sample signal from radiation emitted from surroundings such as walls, ceilings, buildings and instruments, which is reflected by a surface different from a blackbody. When measuring inside a laboratory, the sample needs to be heated up to at least 20 K above ambient temperature to produce this thermal contrast (King *et al.*, 2004; Salisbury and D’Aria, 1994; Schlerf *et al.*, 2012). This method is not suitable for green leaves and other temperature sensitive samples. Alternatively, thermal measurements are possible outside under clear sky conditions. The relatively poor downwelling radiation (DWR) from clear sky appears like radiation emitted from a very cold blackbody and the samples can be measured at ambient temperature. The sample should be isolated from radiating objects, because the high amount of radiation from warm objects would overpower the subtle spectral contrast of plant spectra.

### 3.2.2 Measurement Setup

Hyperspectral thermal infrared imaging data were collected using a *Hyper-Cam LW* (Telops Inc., Québec, Canada) camera that measures radiation emitted from objects in many narrow bands. This instrument is a Fourier-transform imaging spectrometer, using a  $320 \times 256$  pixel MCT (mercury cadmium telluride) detector and records one interferogram per pixel. TIR radiance spectra can be derived from these interferograms at a spectral resolution of up to  $0.25 \text{ cm}^{-1}$  (Schlerf *et al.*, 2012). To prevent disturbances by self-emission, the detector is cooled down to 65 K. The spectrometer was equipped with a wide-angle telescope and a  $45^\circ$  tilted gold-coated mirror, which allows a vertical view with a field of view of  $25.6^\circ \times 30.6^\circ$  corresponding to  $443 \text{ mm} \times 358 \text{ mm}$  and a pixel size of 2.07 mm at 1.5 m distance. A spectral sampling distance of  $3.3 \text{ cm}^{-1}$  with  $4 \text{ cm}^{-1}$  FWHM (Full Width at Half Maximum) corresponding to 40 nm at  $10 \mu\text{m}$  was chosen in the spectral domain from  $865$  to  $1280 \text{ cm}^{-1}$  (7.8 – 11.56  $\mu\text{m}$ ), resulting in 125 bands.

At a distance of 1.5 m, a highly diffuse reference target (Infragold®, Labsphere Inc, North Sutton, USA) of known reflectance was centred in the scans to quantify DWR. Five leaves were picked per plant and clipped in a sample holder in front just above the Infragold® panel. This setup allowed the acquisition of image cubes only composed of sample spectra and DWR. Another advantage of this setup



is that target and background spectra are clearly different and this allows the identification of mixed leaf border pixel. Most of the spectrometer and the tripod were covered by crinkled aluminium foil to avoid thermal radiation emitted from the equipment from disturbing the measurements.

To achieve a high signal-to-noise ratio (SNR), eight consecutive acquisitions were collected per scene. One acquisition taking eight seconds, the total acquisition time was about one minute per scene. Because of subtle temperature fluctuations due to wind, these eight single data cubes were individually processed before being averaged.

### 3.2.3 Image Processing and Temperature-Emissivity Separation

The radiometric calibration interferogram datacubes, including Fourier transformation, 2-point-blackbody calibration ( $BB_{\text{cold}} = 20\text{ }^{\circ}\text{C}$  and  $BB_{\text{hot}} = 35\text{ }^{\circ}\text{C}$ ) and bad pixel correction, was accomplished using the *Reveal Calibrate* software (Telops, Quebec, Canada). A Hamming windowing function was chosen as apodization window, resulting in smooth radiance spectra (Blackman and Tukey, 1958).

The resulting radiance datacubes were then processed to spectral emissivity. The self-emission of an object at some temperature  $T$  is modulated by the emissivity of the material. In addition, for surfaces with emissivities differing from unity, the object leaving radiance contains a reflected downwelling component from the atmosphere. This DWR not only originates from the atmosphere above the sample, but also from the surrounding objects, such as equipment and buildings. On the other hand, the intervening atmosphere absorbs some of the surface leaving radiance and adds path radiance. Thus, the hyperspectral TIR spectra need to be corrected for these effects to retrieve surface emissivity and temperature. This is commonly combined in a process known as temperature and emissivity separation (TES).

DWR spectra, measured using an Infragold® plate, need to be corrected for the plate's self-emission that requires knowing the temperature and emissivity of the reference targets. For the Infragold® target an average emissivity of 0.046 in TIR was gathered from the calibration certificate, and the Infragold® temperature was assumed to be ambient temperature.

When DWR is known, surface emissivity spectrum is derived using the following equation:

$$\varepsilon_S(\lambda) = \frac{L_S(\lambda) - L_{DWR}(\lambda)}{L_{BB}(T_S, \lambda) - L_{DWR}(\lambda)} \quad , \quad (\text{V-1})$$

where  $\varepsilon_S(\lambda)$  is the sample's spectral emissivity,  $L_{DWR}(\lambda)$  the downwelling radiance, and  $L_{BB}(T_S, \lambda)$  the blackbody radiance at the sample's kinetic temperature  $T_S$ . In order to use Eq. (V-1), exact knowledge of the sample kinetic temperature is required.

Since kinetic surface temperatures are typically not known with the required accuracy, alternative processing approaches have to be used. For temperature retrieval under clear sky conditions, the “Downwelling Radiance Residual Index (DRRI)”- method (Wang *et al.*, 2008) was chosen, which is based on the “spectral smoothness” - approach (Horton *et al.*, 1998). Although this method is only applicable under clear sky conditions, it is less restrictive than the “reference channel” - approach (Kahle and Alley, 1992) and the “maximum spectral temperature” - approach (Korb *et al.*, 1996) because it requires no *a priori* knowledge (*e.g.*, peak value of emissivity, wavelength of peak emissivity). The sole premise of the DRRI approach is that the distance from sample to sensor is very short and that atmospheric contribution is negligible within this path.

For the application of the DRRI approach, DWR and the surface leaving radiance (approximated here by the radiance at sensor) need to be known. This data being extracted from the hyperspectral thermal infrared image data, the remaining surface temperature and surface emissivity is derived by an optimization algorithm, trying to find the surface temperature which is the solution for  $DRRI = 0$  (OuYang *et al.*, 2010).

### 3.2.4 Validation of Emissivity Spectra

For validation, *Hyper-Cam LW* spectra were compared to reference spectra from a laboratory spectrometer. Reference measurements were done at the spectroscopic facilities of the University of Twente’s GeoScience Laboratory using a Bruker Vertex 70 FTIR laboratory spectrometer, equipped with an integrating sphere (Hecker *et al.*, 2011). For every species, one representative plant was selected and 5 leaves were picked for reference measurements. Checking the range of the absolute values and the remaining atmospheric residual peaks in the processed spectra provides good initial information on the quality of the applied TES. This first test was consolidated by the calculation of similarity criteria such as the Pearson’s correlation coefficient ( $r$ ) and the Nash-Sutcliffe-Efficiency index (NSE) (Nash and Sutcliffe, 1970). The NSE ranges from 1 to  $-\infty$  where  $NSE < 0$  indicates that the mean value of the *Hyper-Cam LW* spectrum would have been a better predictor than the *Hyper-Cam LW* spectrum,  $NSE > 0$  indicates that the *Hyper-Cam LW* spectrum performs better than the mean value and  $NSE = 1$  corresponds to a perfect match between *Hyper-Cam LW* spectra and Bruker reference measurements. For each species, 100 image pixels were randomly selected over all leaves for comparison with one average reference spectrum. From these values, the probability density function was derived and the mode of this function was used to characterize the most representative similarity value between the *Hyper-Cam LW* spectra and Bruker reference spectra.

### 3.3 Visible to Shortwave Infrared

To compare the separation power for species discrimination using TIR data to that of traditional VSWIR spectra, we collected additional spectra in the 350 – 2500 nm spectral range using an ASD FieldSpec® III spectroradiometer (Analytical Spectral Devices Inc., Boulder, CO, USA) equipped with a Plant Probe. The Plant Probe consists of a clamp with a constant light source and a rotating dark or white background with a spot size diameter of 10 mm. This setup allows for non-destructive leaf measurements under controlled illumination conditions (Carvalho *et al.*, 2013). Immediately after the hyperspectral thermal infrared measurements, the same five leaves per plant were measured individually in the reflective domain. The spectroradiometer was calibrated using the white reference target of the leaf-clip. In order to derive leaf surface reflectance, the single leaves were clamped in front of the black background of the leaf-clip. For every leaf, three leaf-clip measurements were distributed of the central part of the leaves, each averaged over 30 single measurements. These 90 spectra were averaged resulting in one spectrum per leaf representing an area of approximately 240 mm<sup>2</sup>. White reference and grating drift corrections were performed on each spectrum following Dorigo *et al.* (2006). As a result, 280 reflectance spectra were collected in the VSWIR spectral domain and used further for the statistical analysis.

### 3.4 Statistical Analysis

A Random-Forest classifier (RFC) (Breiman, 2001) was chosen for species classification. This classifier is non-parametric and is well suited to analyse high dimensional data. For statistical analysis, spectral bands dominated by water vapour from 7.8  $\mu\text{m}$  – 8.037  $\mu\text{m}$  were removed from the spectra, resulting in a spectral range of 865  $\text{cm}^{-1}$  – 1244  $\text{cm}^{-1}$  (8.038 – 11.56  $\mu\text{m}$ ) for the TIR and 400 – 2450 nm for the VSWIR.

#### 3.4.1 Comparison of Discrimination Accuracies in Different Spectral Ranges

Since the same leaves were measured in the TIR and VSWIR spectral range, a comparison of classification accuracies could be accomplished. For the VSWIR spectral range, the averaged 280 reflectance spectra were subjected to the RFC. To make the TIR dataset comparable to the VSWIR dataset, the TIR image data were reduced to one emissivity spectrum per leaf by averaging 20 random pixels from the image dataset, covering the same area as the VSWIR spectrometer's plant probe. The resulting 280 emissivity spectra were subjected to the RFC. To assess the heterogeneity of the dataset, averaging of emissivity pixels followed by RFC was performed 20 times. To select the most representative classification model from the 20 individual classification runs, quality measures like OAA and Kappa values were recorded. From these values, the probability density function was derived and the mode of this function was used to characterize the classification accuracy.

### 3.4.2 Image Classification

For image classification 100 pixels per species were randomly selected as training dataset and another set of 100 different pixels were randomly selected as validation dataset. To account for the effects of pseudoreplication on the classification accuracy, which arises from the fact that each five leaves were picked from the same plant, training data were collected from 4 of the 7 individual plants and validation data from the remaining 3 plants. The image background consisting of an Infragold® reference plate was used as an additional endmember into the discrimination analysis. For the RFC a data reduction was carried out using a principal component analysis (PCA). The number of principal components was chosen to reach a cumulative proportion of  $> 0.95$ . As in 3.4.1., 20 classification runs were performed. To select the most representative classification model, the classification model closest to the mode of the OAA density function was selected. This most representative model was applied to the image dataset.

To investigate the influence of SNR on the classification results, the methodology described above was applied on two additional datasets: Before being subjected to TES, the radiance datasets were pre-processed with (i) a 3x3 kernel filter and (ii) a 5x5 kernel filter. In order to avoid averaging of leaf and background pixel at the edges of leaves, a median filter was chosen as kernel filter.

### 3.4.3 Spectral Band Reduction

To assess the importance of certain wavebands for species discrimination, the random forest classifier's band importance was derived. Band importance is determined as the mean decrease in accuracy (MDA) during processing, *i.e.* the difference in prediction accuracy, averaged over all trees, before and after randomly permuting the predictor variable and breaking its original association with the response (Breiman, 2001; Nicodemus, 2011). Further, to investigate the predictive power of the most important bands, classification was repeated with an increasing number of input bands, selected by decreasing importance.

## 4 Results

### 4.1 Visible to Shortwave Infrared

Focusing on the spectral signatures in the VSWIR, the shapes of the spectra only show small between-species variabilities. Spectral behaviour of all species is clearly determined by common features, such as green peak, pigment absorption minima, red edge, infrared plateau with minor water absorption bands, and SWIR with major water absorption bands. In the NIR all the species present an average maximum reflectance between 44 % and 52 %, with the exception of *Acer platanoides* which shows significantly lower reflectance values (Fig. V-1). Looking into detail, the standard deviation of *Liquidambar styraciflua* and *Ginkgo biloba* is significantly larger in comparison to the remaining 6 species due to differences in leaf structure.

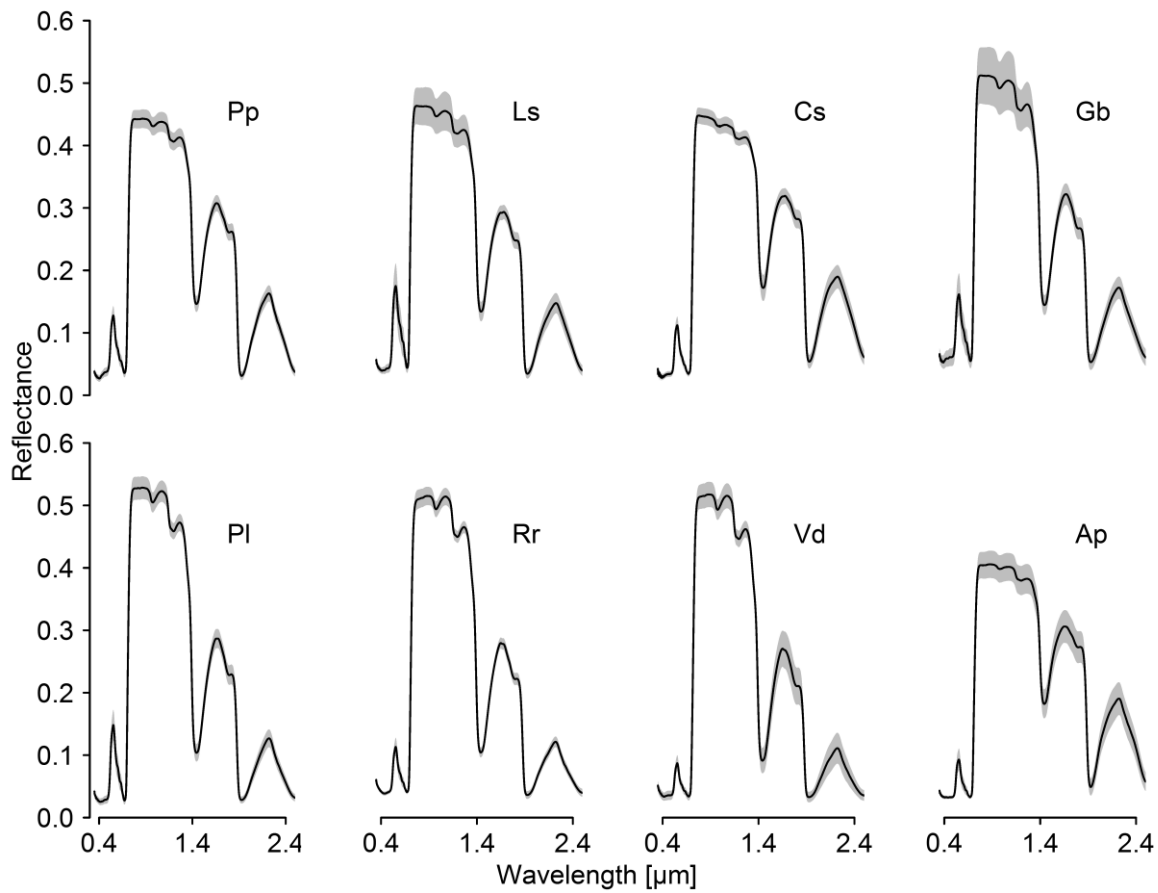


Fig. V-1: VSWIR spectra for the investigated species. Black: Mean spectra (N = 35), grey: mean +/- 1 standard deviation

## 4.2 Validation of Emissivity Spectra

A first visual evaluation of the emissivity spectra presents smooth signatures in a rational range. Fig. V-2 shows the spectral information per species. The different vegetation spectra, with a range of emissivity from 90 % to 99 % show distinctive shapes comprising mainly a low frequency component superimposed by a variety of narrow spectral features. Although an offset between *Hyper-Cam LW* and the reference spectra is present for large parts of the spectral range, the shapes of the spectra correspond relatively well to the reference spectra. The offset varies from 1 to 3 % (absolute emissivity) for different species.

To remove the offset between *Hyper-Cam LW* spectra and reference spectra for a better comparison of their shapes, vector normalization was applied. Normalization is performed by dividing the single band's values by the sum of all of the 115 band values. Fig. V-3 shows normalized spectra. In general, the overall shape of *Hyper-Cam LW* spectra fit well to the normalized reference spectra.

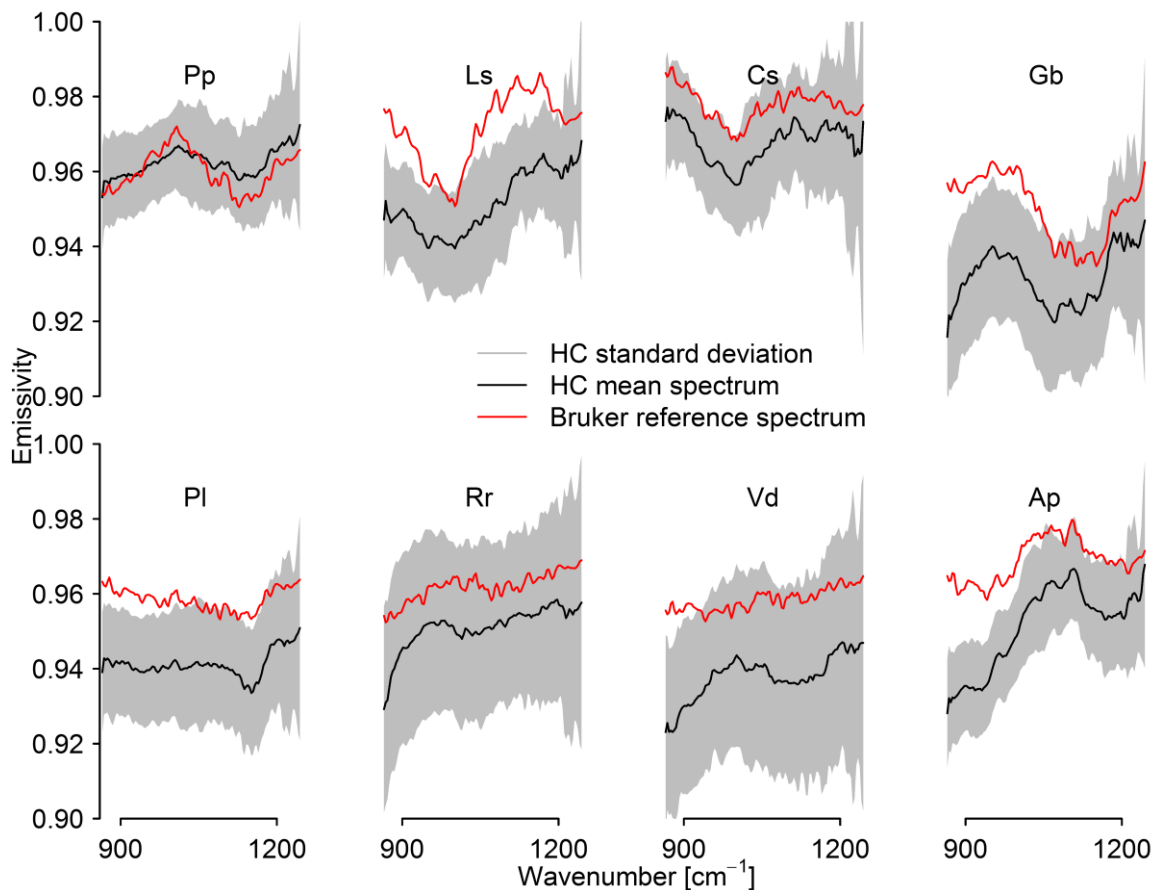


Fig. V-2: Comparison of *Hyper-Cam LW* spectra (black line: average of 100 randomly selected pixel, grey: mean  $\pm$  1 sd) with Bruker reference spectra (red line).

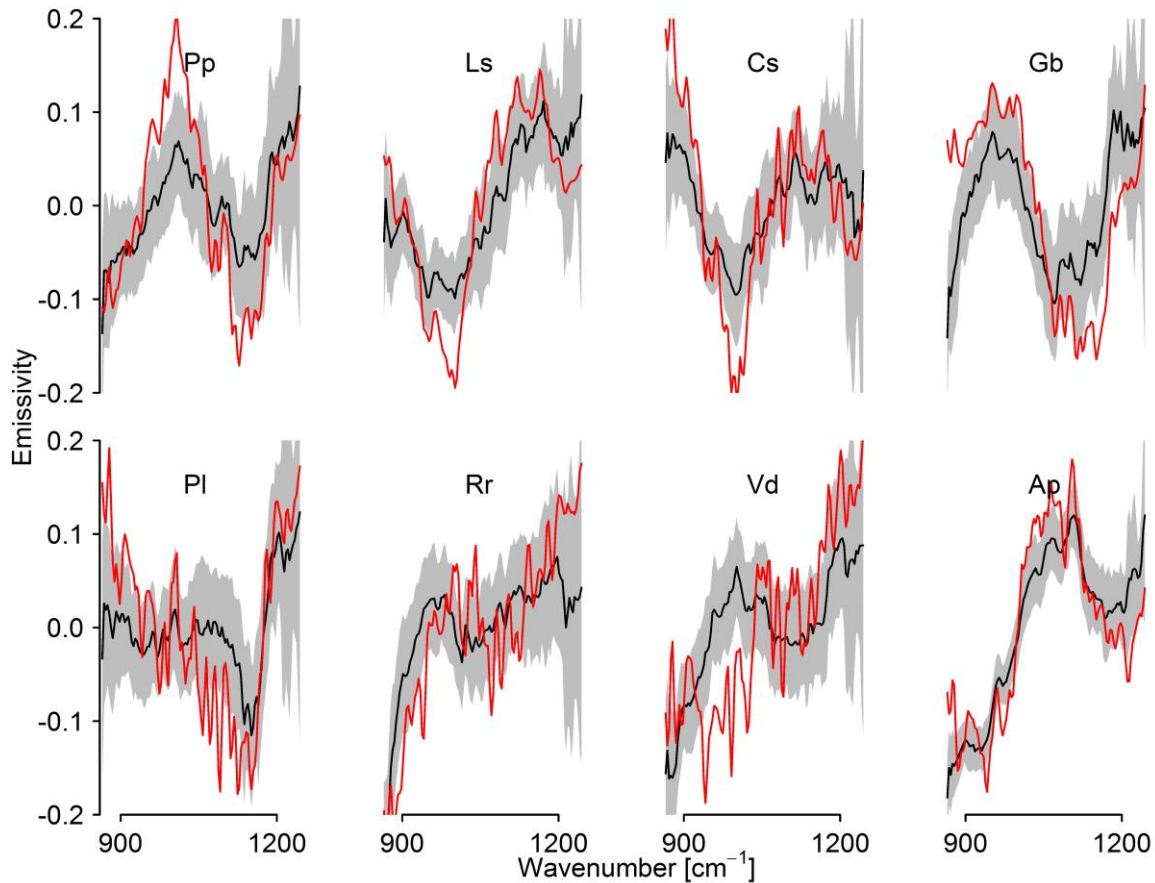


Fig. V-3: Comparison of vector normalized *Hyper-Cam LW* spectra (grey and black) and Bruker reference spectra (red).

The similarity values (NSE and  $r$ ) between normalized *Hyper-Cam LW* spectra and Bruker reference spectra are listed in Table V-2. All of the tested species have positive NSE of which five have NSE values  $> 0.60$ . While *Acer platanoides* and *Prunus persica* present the best results, *Ginkgo biloba*, *Viburnum davidii* and *Prunus lauracerasus* present the poorest. These results support the visual analysis of the image data (Fig. V-4).

Table V-2: Nash-Sutcliffe-Efficiency Index (NSE) and Pearson's correlation coefficient ( $r$ ) for the different species measured with the *Hyper-Cam LW* and Bruker Vertex 70.

Species	$r$	NSE	
<i>Prunus persica</i>	0.958	0.78	+++
<i>Liquidambar styraciflua</i>	0.943	0.73	++
<i>Cornus sericea</i>	0.913	0.63	++
<i>Ginkgo biloba</i>	0.778	0.58	++
<i>Prunus lauracerasus</i>	0.757	0.50	+
<i>Rhododendron repens</i>	0.841	0.65	++
<i>Viburnum davidii</i>	0.681	0.44	+
<i>Acer platanoides</i>	0.927	0.84	+++

### 4.3 Species Discrimination

#### 4.3.1 Comparison of Discrimination Accuracies in Different Spectral Ranges

The results shown in Table V-3 compare the classification results of TIR spectral range with respect to the reflective spectral range. While Table V-3 presents the overall accuracies for both spectral domains, Table V-4 and Table V-5 present the error matrix allowing an in-depth analysis of the results.

Classification results based on thermal infrared spectroscopy data outperform the classifications based on VSWIR data by almost 12 % in OAA.

Table V-3: Classification results (mode +/- 1 sd of 20 classification runs) for the two spectral domains.

Spectral Range	OAA	kappa
TIR	92.26 % (+/- 1.54)	0.9115 (+/- 0.0176)
VSWIR	80.28 % (+/- 0.43)	0.7746 (+/- 0.0049)

Table V-4: Representative error matrix for a single classification run based on TIR spectroscopy data.

		<i>Pp</i>	<i>Ls</i>	<i>Cs</i>	<i>Gb</i>	<i>Pl</i>	<i>Rr</i>	<i>Vd</i>	<i>Ap</i>	Total	User's Accuracy [%]
Classification Results	<i>Pp</i>	<b>31</b>	5	0	0	0	0	0	0	36	86.11
	<i>Ls</i>	3	<b>30</b>	0	0	0	0	0	0	33	90.91
	<i>Cs</i>	0	0	<b>35</b>	0	1	0	0	0	36	97.22
	<i>Gb</i>	1	0	0	<b>31</b>	4	0	0	0	36	86.11
	<i>Pl</i>	0	0	0	4	<b>30</b>	0	0	0	34	88.24
	<i>Rr</i>	0	0	0	0	0	<b>34</b>	1	0	35	97.14
	<i>Vd</i>	0	0	0	0	0	1	<b>33</b>	1	35	94.29
	<i>Ap</i>	0	0	0	0	0	0	1	<b>34</b>	35	97.14
Total		35	35	35	35	35	35	35	35	280	
Producer's Accuracy [%]		88.57	85.71	100.00	88.57	85.71	97.14	94.29	97.14	Overall Accuracy: 92.14 % Kappa statistic: 0.9102	

Table V-5: Representative error matrix for a single classification run based on VSWIR spectroscopy data.

		<i>Pp</i>	<i>Ls</i>	<i>Cs</i>	<i>Gb</i>	<i>Pl</i>	<i>Rr</i>	<i>Vd</i>	<i>Ap</i>	Total	User's Accuracy [%]
Classification Results	<i>Pp</i>	<b>29</b>	7	3	0	0	0	0	0	36	74.36
	<i>Ls</i>	2	<b>22</b>	0	2	2	0	0	0	33	78.57
	<i>Cs</i>	2	0	<b>30</b>	2	2	0	1	9	36	68.18
	<i>Gb</i>	0	3	0	<b>31</b>	2	0	0	0	36	91.18
	<i>Pl</i>	0	3	0	0	<b>30</b>	1	1	0	34	85.71
	<i>Rr</i>	0	0	0	0	1	<b>29</b>	5	0	35	82.86
	<i>Vd</i>	0	0	0	0	2	5	<b>27</b>	0	35	79.41
	<i>Ap</i>	2	0	2	0	0	0	0	<b>26</b>	35	86.67
Total		35	35	35	35	35	35	35	35	280	
Producer's Accuracy [%]		82.86	62.86	85.71	88.57	85.71	82.86	79.41	74.29	Overall Accuracy: 80.29 % Kappa statistic: 0.7747	

Table V-6: Error matrix from classification result based on native spatial resolution image data.

		Reference data								Total	User's Accuracy [%]	
		<i>Pp</i>	<i>Ls</i>	<i>Cs</i>	<i>Gb</i>	<i>Pl</i>	<i>Rr</i>	<i>Vd</i>	<i>Ap</i>	bgrd	Total	User's Accuracy [%]
Classification Results	<i>Pp</i>	<b>53</b>	1	0	12	7	0	10	5	0	88	60.2
	<i>Ls</i>	0	<b>81</b>	10	0	0	2	1	10	9	113	71.7
	<i>Cs</i>	1	5	<b>87</b>	1	7	7	5	0	5	118	73.7
	<i>Gb</i>	12	0	0	<b>68</b>	2	0	1	0	0	83	81.9
	<i>Pl</i>	7	1	1	2	<b>74</b>	4	8	0	2	99	74.7
	<i>Rr</i>	0	0	0	3	3	<b>74</b>	23	0	2	105	70.5
	<i>Vd</i>	7	1	0	5	5	7	<b>38</b>	0	1	64	59.4
	<i>Ap</i>	18	10	0	8	1	0	9	<b>82</b>	2	130	63.1
	bgrd	2	1	2	1	1	6	5	3	<b>79</b>	100	79.0
Total		100	100	100	100	100	100	100	100	100	900	
Producer's Accuracy [%]		53.0	81.0	87.0	68.0	74.0	74.0	38.0	82.0	79.0	Overall Accuracy: 70.7 % Kappa statistic: 0.67	



Table V-7: Error matrix from classification result based on spatial averaged (3x3) image data.

		Reference data									Total	User's Accuracy [%]
		<i>Pp</i>	<i>Ls</i>	<i>Cs</i>	<i>Gb</i>	<i>Pl</i>	<i>Rr</i>	<i>Vd</i>	<i>Ap</i>	bgrd		
Classification Results	<i>Pp</i>	<b>81</b>	2	0	9	3	0	3	1	0	99	81.8
	<i>Ls</i>	0	<b>91</b>	4	0	0	0	0	8	0	103	88.3
	<i>Cs</i>	0	3	<b>96</b>	0	0	0	0	0	3	102	94.1
	<i>Gb</i>	4	1	0	<b>71</b>	0	0	0	0	0	76	93.4
	<i>Pl</i>	5	0	0	1	<b>95</b>	5	1	1	1	109	87.2
	<i>Rr</i>	0	0	0	0	0	<b>85</b>	23	0	2	110	77.3
	<i>Vd</i>	2	0	0	4	2	8	<b>69</b>	3	1	89	77.5
	<i>Ap</i>	6	3	0	15	0	0	2	<b>87</b>	2	115	75.7
	bgrd	2	0	0	0	0	2	2	0	<b>91</b>	97	93.8
Total		100	100	100	100	100	100	100	100	100	900	
Producer's Accuracy [%]		81.0	91.0	96.0	71.0	95.0	85.0	69.0	87.0	91.0		Overall Accuracy: 85.11 % Kappa statistic: 0.8325

Table V-8: Error matrix from classification result based on spatially averaged (5x5) image data.

		Reference data									Total	User's Accuracy [%]
		<i>Pp</i>	<i>Ls</i>	<i>Cs</i>	<i>Gb</i>	<i>Pl</i>	<i>Rr</i>	<i>Vd</i>	<i>Ap</i>	bgrd		
Classification Results	<i>Pp</i>	<b>85</b>	1	0	11	0	0	0	2	0	121	85.9
	<i>Ls</i>	1	<b>90</b>	6	0	0	0	0	4	2	115	87.4
	<i>Cs</i>	0	2	<b>92</b>	0	0	1	0	0	2	105	94.8
	<i>Gb</i>	4	0	0	<b>79</b>	0	0	0	0	0	83	95.2
	<i>Pl</i>	0	1	0	0	<b>95</b>	4	1	0	1	114	93.1
	<i>Rr</i>	0	0	0	0	0	<b>88</b>	4	0	0	78	95.7
	<i>Vd</i>	0	0	0	1	5	5	<b>92</b>	1	0	79	88.5
	<i>Ap</i>	10	6	0	9	0	0	2	<b>93</b>	1	106	76.9
	bgrd	0	0	2	0	0	2	1	0	<b>94</b>	99	94.9
Total		100	100	100	100	100	100	100	100	100	900	
Producer's Accuracy [%]		85.0	90.0	92.0	79.0	95.0	88.0	92.0	93.0	94.0		Overall Accuracy: 89.8 % Kappa statistic: 0.8850

### 4.3.2 Image Classification

Tables V-6 to Table V-8 show the classification results of TIR image data for different spatial smoothing pre-processings (native spatial resolution (Table V-6), 3 x 3 (Table V-7) and 5 x 5 (Table V-8) averaging window).

The classification of thermal spectroscopic image data at full spatial resolution achieved an OAA of 70.7 % (Kappa = 0.67) which indicates a good overall discrimination of the investigated plant species using emissivity spectra. These accuracies rise with increasing averaging window size (3x3 averaging: OAA = 85.1 %, Kappa = 0.83; 5x5 averaging: OAA = 89.8 %, Kappa = 0.89).

Consistently, for classifications of the three image datasets, *Pp*, *Gb* and *Vd* show the poorest results. Mostly, *Pp* is confused with *Gb* and *Ap*, *Gb* is confused with *Pp* and *Ap* and *Vd* is confused with *Pp* and *Rr*. While these three species are often confused with *Ap*, the latter is classified with high accuracies.

Image classification results depicted in Fig. V-4 show a good performance in general. Most of the leave pixels were correctly assigned. Misclassifications mostly occurred on complete leaves or certain parts of leaves. The leaves of *Cornus sericea* comprise a high percentage of NA-values (black pixels), which results from a non-converging of the residual minimizing algorithm during TES. Except for the NA-values, *Cornus sericea* does not show many misclassifications. For *Acer platanoides* large parts of leaves originating from one single plant show a high percentage of misclassifications, which could be due to intraclass variability. While *Ginkgo biloba* is mostly confused with *Prunus persica* and *Acer platanoides*, *Viburnum davidii* is confused with most of the remaining classes (*i.e.*, *Prunus persica*, *Liquidambar styraciflua*, *Cornus sericea*, *Prunus laurocerasus*, *Rhododendron repens* and *Acer platanoides*). All other species mostly present random misclassifications with remaining species.

With increasing SNR (Fig. V-4 middle and bottom), the number of misclassification is strongly reduced and only coherent misclassifications remain in the resulting image. This points to the spatial heterogeneity in individual leaves.

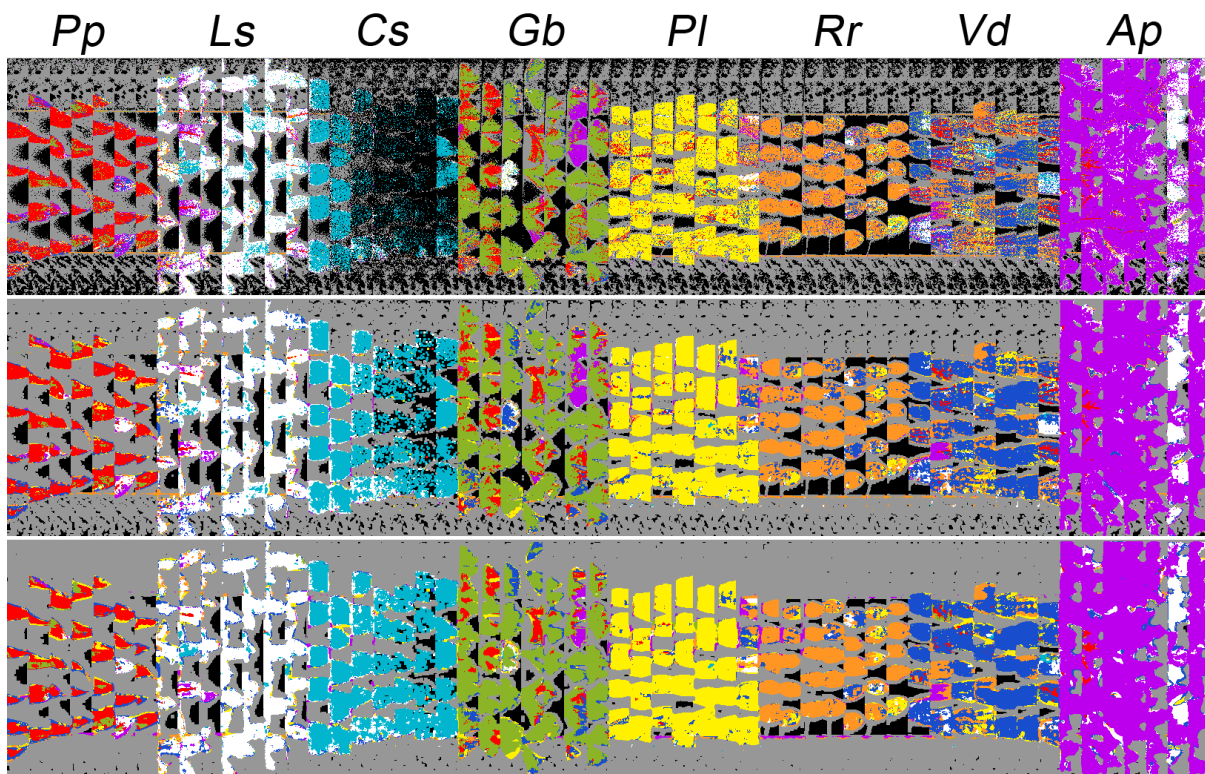


Fig. V-4: Classification result from native spatial resolution (top), 3 x 3 spatial averaging (middle) and 5 x 5 spatial averaging (bottom). Colour: species, grey: background, black: pixel with non-converging TES. The 5 leaves from one column originate from one plant. The leaves from Ap being much larger than the remaining, it seems that a lot of background pixel were misclassified, which is not the case.

### 4.3.3 Spectral Band Reduction

Fig. V-5 depicts the relative importance of spectral band for discrimination of the 8 species (left) and the accuracies achieved during classification using an increasing number of spectral bands with respect to their importance (right). Local maxima and minima ( $8.19 \mu\text{m} / 1220.90 \text{ cm}^{-1}$ ,  $8.4 \mu\text{m} / 1190.96 \text{ cm}^{-1}$ ,  $8.49 \mu\text{m} / 1177.65 \text{ cm}^{-1}$ ,  $9.7 \mu\text{m} / 1031.28 \text{ cm}^{-1}$ ,  $10.19 \mu\text{m} / 981.38 \text{ cm}^{-1}$ ,  $10.51 \mu\text{m} / 951.44 \text{ cm}^{-1}$ ,  $10.81 \mu\text{m} / 924.82 \text{ cm}^{-1}$ ) in band importance agree well with results from Ullah *et al.* (2012b). The discrimination accuracy varies with respect to the number of bands used for classification. Starting from an OAA of 66.94 % for 2 bands, the discrimination accuracy increases up to 91.79 % for 6 bands. Further increase of bands leads to a weak gain in accuracy up to 94.73 % for 44 spectral bands (Fig. V-5, right). These results fit well with the results from the comparison of classification accuracies for different spectral ranges (Tables V-4 & 5).

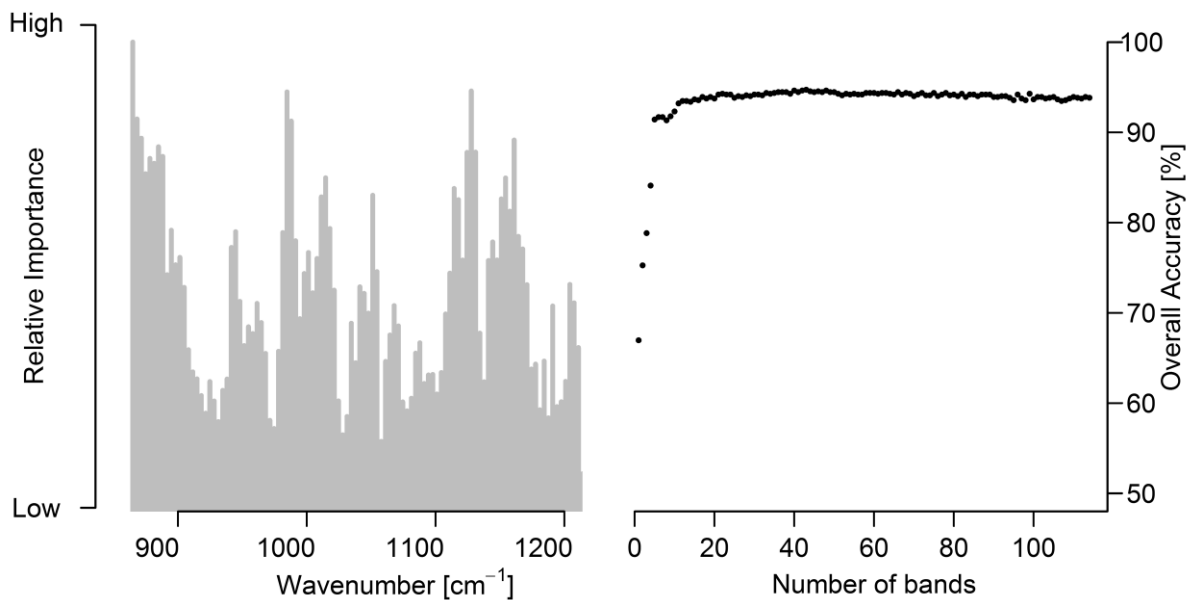


Fig. V-5: Relative importance of spectral band for RFC (left) and OAA of RFC by increasing number of spectral bands (right).

## 5 Discussion

Data acquisition using a hyperspectral thermal infrared camera (such as the Telops *Hyper-Cam LW*) is a fast and accurate way of measuring emissivity spectra of plants in a spatially continuous way. As multiple pixels can be averaged for homogeneous samples, SNR increases and derived emissivity spectra compare well to laboratory reference spectra.

When comparing the *Hyper-Cam LW* spectra with laboratory reference spectra, an offset of 1 to 3 % (absolute emissivity) was detected. This offset can have various reasons: i) errors in the temperature estimation during TES or ii) the radiometric calibration or iii) systematic spectrometer errors. Since the *Hyper-Cam LW* spectra presented smooth shapes and did not show any large atmospheric residuals, errors during TES and radiometric calibration could be excluded. Hecker *et al.* (2011) conclude that the described Bruker FTIR laboratory spectrometer tends to have marginally lower values at very low reflectance in comparison to similar spectrometers. Therefore, lower reflectance corresponding to higher emissivity values would explain the offset in vegetation spectra, usually ranging between 94 to 99 % of emissivity or 1 to 6 % of reflectance. This offset was eliminated by vector normalization in both datasets to allow the shapes of the emissivity curves to be compared.

When looking very closely at the different spectra, small divergences are still detectable between *Hyper-Cam LW* and Bruker reference spectra. The reason for these divergences is probably related to the fact that the acquisition of reference measurements could not be taken simultaneously with the *Hyper-Cam LW* measurements and leaves that were picked for both measurements were not identical.

The DRRI approach to derive emissivity from radiance data appears to be a well-suited TES method for field measurements at short distances from the sample. Minimizing an average smoothness value is affected by noise and leads to atmospheric residuals in the resulting emissivity spectrum. This is why our temperature retrieval focused on minimizing residuals of the most prominent water line, *i.e.* the line at  $1174.53 \text{ cm}^{-1}$  ( $8.514 \text{ }\mu\text{m}$ ), which is included in the spectral band with centre wavenumber  $1174.33 \text{ cm}^{-1}$  ( $8.515 \text{ }\mu\text{m}$ ). The fact that the remaining residuals in the individual spectra are compensated by averaging multiple pixels per leaf illustrates that the TES algorithm has a good performance and does not produce a systematic over- or underestimation of temperature.

Concerning intraclass heterogeneity, especially the spread of the *Rhododendron repens* and *Viburnum davidii* spectra is wider than for the remaining species (Fig. V-2). As the samples were randomly chosen within one canopy, leaves of different ages and illumination conditions, presenting different physiological and biochemical conditions, were selected, resulting in different spectral emissivities (Buitrago *et al.*, 2016).

Species discrimination using a random forest classifier led to good results and improved significantly with respect to spatial averaging. In summary, the initial dataset achieved an OAA of 70.7 %,

the 3 x 3 averaging pre-processing resulted in an OAA of 85.1 % and the 5 x 5 averaging pre-processing in an OAA of 89.8 %. On the whole, TIR spectroscopy allows for identification of objects with very subtle spectral signatures and differences. With reference to Fig. V-4, the consistent confusions of *Pp* and *Gb* spectra are related to the similarity of the species specific spectra. The misclassifications of many pixel as *Vd* are due to the wide variance within the species spectra. The lower variance and the unique spectral shape for *Ap* causes the good producer's accuracy (93.0 %) and the corresponding poorer user's accuracy (76.9 %).

Misclassifications are not distributed randomly over the complete dataset but concentrate on complete or certain parts of leaves. It appears that this is related to a spatial variation of emissivity spectra caused by inhomogeneity of biochemistry and leaf structural properties within and between leaves of the same species. Especially some leaves from *Ginkgo biloba* present misclassifications at the apexes and all the leaves from one *Acer platanoides* plant present wide misclassifications. This fact points to the assumption that the leaves and some individual plants were in different physiological states, *i.e.* showed signs of stresses. The identification of these spatial heterogeneities impressively demonstrates the advantage of imaging over non-imaging spectroscopy.

In order to provide a complete impression on the potential of the Telops *Hyper-Cam LW*, classification was also performed on single measurements. The results are poorer than those obtained from image datasets averaged over eight repeated measurements (Table V-6 to Table V-8) but, even with single measurements, OAA of 54.67 % could be achieved. With spatial averaging pre-processing OAA of 65.67 % and 76.11 % were achieved for kernel sizes of 3x3 and 5x5 respectively.

Comparing with a laboratory study from Ullah *et al.* (2012b) who achieved an OAA of 92 %, these results are completely satisfying, taking into account the argument of an in-situ experiment, the smaller spectral range and the very short duration per acquisition.

These classification results confirm the stated hypothesis, which means that TIR measurements are well suited for vegetation analysis. In addition, these results confirm that for this special experimental setup, hyperspectral thermal infrared measurements provide better classification results than measurements in the reflective domain. This can be explained by the fact that primary absorption bands of many constituents are located in the TIR spectral region.

The results of the band reduction experiment meet our expectations. Selecting single narrow bands, with respect to their importance during classification, indicated a significant improvement of OAA when selecting up to 6 bands. Adding more bands to the classification did only result in a slight improvement for classification results. Although these results are remarkable and would lead to a conclusion that a sensor comprising only 6 – 10 well-chosen bands would allow for similar results, it needs careful evaluation. Obviously, the considered plants differ more with respect to their spectral emissivity

shapes than the respective reflectance curves in the solar spectral domain. However, without further studies, this result cannot be generalized to other plant species, which might have similar spectral characteristics in the TIR but unique features in the VSWIR.

Though at near range, TIR imaging spectroscopy allows for accurate and reliable retrieval of plant emissivities and species discrimination, there are still many challenges to overcome for airborne and future spaceborne sensors: (i) atmosphere correction and TES algorithms require knowledge of the spatial distribution of atmospheric water vapour; its quantification requires radiance measurements in narrow spectral bands which are generally limited in their signal to noise ratio, (ii) increasing observation distances implies scale effects related to structural issues (*i.e.*, mixed pixels, scattering, re-radiation and cavity effects) (Kirkland *et al.*, 2002) resulting in non-linear mixtures of signatures and reduction of spectral contrast (Gillespie, 1992; Ribeiro da Luz and Crowley, 2010).

## 6 Conclusion

This study demonstrated the suitability of the TIR spectral range for species discrimination. Important aspects of the study include (i) that the suitability of the Telops *Hyper-Cam LW* for TIR data acquisition does not only account for gases, but for surfaces of low spectral contrast, too, (ii) the ability of discriminating multiple plant species using emissive imaging spectroscopy, (iii) the superiority of emissivity spectra over VSWIR reflectance data for this special experimental setup, (iv) the ability to uncover spatial heterogeneities using the TIR imaging spectrometer, and (v) the influence of SNR on the classification results.

In our experiment we demonstrated that the Telops *Hyper-Cam LW* is not only suitable for data acquisition of samples with very prominent spectral features, *e.g.* gas detection purposes or mineral detection (Schlerf *et al.*, 2012), but, in addition, is able to collect high-quality data suitable for surface analysis for materials with very subtle spectral signatures, such as vegetation.

Further, we showed that the TIR spectral range is suitable for species discrimination. Although, the spectral contrast for vegetation in the TIR only spans 4 % absolute emissivity, the spectral signatures of the selected species show substantial differences in shape, which is different from the reflective spectral domain. Therefore, TIR spectroscopy can be considered as a valuable addition to VSWIR spectroscopy for vegetation studies. As the spectral contrast is relatively low, an increase in SNR has a positive effect on classification results.

Finally, we demonstrated that emissive TIR imaging spectroscopy provides fast measurements and accurate as well as reliable results, comparable to laboratory spectrometers. In addition, TIR imaging spectroscopy offers the ability to uncover spatial distributions of surface properties, usually hidden during laboratory non-imaging studies.

## **Acknowledgement**

The authors wish to thank the Fonds National de la Recherche (FNR) of Luxembourg for funding the PhD research of Gilles Rock [AFR reference: 2011-2/SR/2962130] and the PLANTSENS research project [AFR reference: C13/SR/5894876]. In addition the authors would like to thank Trier University's department for Geobotany and the ITC (University of Twente, the Netherlands) for the use of their equipment and facilities. Finally, a special thank goes to Christian Bossung, Henning Buddenbaum, Kim Fischer, Thomas Gattung, Miriam Machwitz and Franz Kai Ronellenfitsch for their tireless support during the experiment.





# **Chapter VI**

## **Synthesis**

## 1. Main Findings

In this thesis, a comparative assessment of different remotely sensed indices for their ability to detect plant responses to water deficit stress has been conducted in experiments at ground- and airborne level. In the following pages, the main findings will be discussed.

### **Objective I: A comparative assessment of hyperspectral remote sensing indices for water deficit stress detection**

Considering the first findings of the applicability of the Telops *Hyper-Cam LW* for remote sensing (see Chapter II), two experimental studies were designed and conducted to compare the ability of different hyperspectral remotely sensed indices to detect plant responses to water stress at ground- and airborne level.

Overall, the most relevant finding of this thesis is that temperature-based measures (*i.e.*,  $T_{leaf}$ ,  $T_{leaf} - T_{air}$ , CWSI) of plant responses to water stress react faster than traditional narrowband VNIR/SWIR indices (*i.e.*, NDVI, PRI, MSI, WI) and SIF, at both ground- and airborne level. This fact could be mainly explained by the different underlying physiological processes corresponding to the plant responses to water stress. Leaf temperature is highly correlated to stomatal closure and thus is the first response to water stress. In contrast, narrowband reflectance based VIs are determined by variations in either leaf internal pigment content, leaf structure or leaf water content and normally occur only under severe or prolonged water stress conditions (see Chapter I section 2).

In particular, in the ground-based water stress experiment (see Chapter III), it was found that remotely sensed indices based on temperature and leaf water content (*i.e.*, MSI, WI) were equally sensitive to water stress. However, since the continuous measurement was interrupted by bad weather conditions, it could not be determined if temperature-based indices even react faster than VIs related leaf water content. Further, CWSI was found to be most suitable for the detection of plant responses to water stress compared to other temperature based indices (*i.e.*,  $T_{leaf}$ ,  $T_{leaf} - T_{air}$ ) due to its robustness against actual meteorological conditions. Moreover, CWSI has the advantage to be normalized to relative temperature differences of two reference surfaces in comparison to absolute measures of leaf or air temperature. CWSI should thus be transferable to various crop types, phenological stages, and climates.

In comparison to temperature-based indices and VIs related to leaf water content, indices based on variations in the content of leaf internal pigments (*i.e.*, PRI, SR) or structural changes in the leaf or canopy (*e.g.*, NDVI) did not react at all during the ground-based water stress experiment. Therefore, the common acceptance of PRI as an early indicator of water stress (*e.g.*, Panigada *et al.*, 2014; Rossini *et al.*, 2013 & 2015b; Zarco-Tejada *et al.*, 2013) could not be confirmed.

The assessment of SIF for the detection of water stress symptoms was limited to the airborne campaign and will be discussed in the following paragraph.

**Objective II: Assess the potential of hyperspectral remote sensing indices for water stress detection at airborne level**

An airborne campaign operating two state-of-the-art hyperspectral instruments was conducted in order to assess the ability of remotely sensed water stress indices at airborne level (see Chapter IV). Since *Hyper-Cam LW* and *HyPlant* sensors were only available for a limited time window, plant physiological water stress symptoms (*e.g.*, rise in plant temperature, decrease of photosynthetic efficiency) were artificially induced by two chemical agents (VG and KA) instead of measuring real water stress.

The first finding of this study was that temperatures retrieved from airborne hyperspectral TIR images agree very well compared to ground temperatures of a water filled pool as measured by thermocouples. Thus, the application of Telops *Hyper-Cam LW* for measuring spatially high-resolution surface temperatures from an airborne platform was validated.

Although no actual plant water stress occurred during the experiment, temperature-based indices were more sensitive for the detection of subtle water stress symptoms in comparison to VNIR/SWIR indices and SIF indices. The hypothesized effects of the two chemical agents were nicely reflected by changes in plant temperature. While VG partly closed the stomata and thus led to an increase in plant temperature, KA reduced the canopy temperature due to a reduction in absorbed radiation. In contrast, VIs (*i.e.*, SR, NDVI, PRI, WI, MSI, LWI) and SIF indices remained unchanged for the VG treatment in comparison to the control. However, for the KA treatment highly significant changes in both VIs and SIF were observed compared to the control, which is explained by the overall reduced *f*APAR. Furthermore, diurnal changes in temperature could be explained by plant transpiration rates and are well correlated to diurnal changes in meteorological parameters (*i.e.*, VPD, air temperature).

In summary, the most important finding of this study was that even mild effects on the stomatal conductance as induced by VG were detected by airborne TIR based indices. On the contrary, the subtle effects of VG on the assimilation of CO<sub>2</sub> and thus, photosynthetic efficiency were too small to be measured with remotely sensed SIF or VNIR/SWIR indices. Therefore, the application of temperature-based indices for the detection of even subtle changes in plant transpiration has been approved on airborne level by using a hyperspectral TIR imaging instrument, the Telops *Hyper-Cam LW*. Consequently, temperature-based indices are most suitable for the pre-visual detection of crop water stress, not only at ground- but also at airborne level. These findings offer promising prospects for future satellite missions for regional and global water stress detection in the TIR spectral domain.

### **Objective III: Examination of the advantages of hyperspectral TIR remote sensing sensors for the retrieval of temperature and emissivity**

A comparison of broadband and hyperspectral TIR imaging systems at ground level was performed in Chapter III. As already introduced in Chapter I, the neglect of the spectral information of emissivity limits the accuracy of temperatures retrieved from broadband TIR imagers to about 1 K per 1 % error in the assumed mean emissivity value (Jones, 2004a). The goals of this analysis were to examine the potential advantages of a hyperspectral over a broadband TIR camera with regards to: (i) a more precise absolute temperature retrieval by solving the TES-problem with a state-of-the-art TES-algorithm (*i.e.*, ‘spectral smoothness’), hypothesizing that a more precise absolute temperature would produce a better input for more sensitive measures of water stress by using temperature-based indices, (ii) the ability of using the spectral information of emissivity itself for the detection of plant responses to water stress.

As a result, the overall mean temperatures retrieved from two broadband approaches (*i.e.*, Fluke TiR1 as a handheld broadband camera and spectrally resampled images of the *Hyper-Cam LW*) agreed very well with the temperatures retrieved using the ‘spectral smoothness’ approach based on hyperspectral data (*i.e.*, the maximum difference in temperature was 0.4 K between the hyperspectral and broadband retrieval approaches). Furthermore, all three approaches were equally sensitive for water stress detection using temperature-based indices. Following these results, hyperspectral TIR offers no advantage over broadband TIR cameras with respect to temperature-based indices for the detection of plant responses to water stress, taking into consideration that the assumed mean emissivity for the broadband approach is equal or very close to the real averaged spectral emissivity (*e.g.*, in this study 0.97 for the examined potato plants). However, the fact that most temperature-based indices only rest on relative temperature differences, the prospective effect of inaccurately retrieved temperatures should be negligible for the detection of water stress, even if the assumed emissivity does not fit properly. For example, CWSI is calculated using the relative differences between  $T_{leaf}$ ,  $T_{wet}$  and  $T_{dry}$ . Notwithstanding, a precise absolute temperature retrieval becomes mandatory for physically-based model approaches such as STIC (Mallick *et al.*, 2015). Furthermore, only hyperspectral systems offer the ability of an appropriate atmospheric correction using images with high spectral resolution, which becomes crucial in air- or spaceborne missions.

In addition, new hyperspectral TIR sensors offer a fast and innovative opportunity to measure the spectral emissivity of vegetation. Since the spectral emissivity is a plant status-related measure, it is considered to be applicable for the detection of plant water stress. In this study, for the first time, plant responses to water stress were detected by changes in plant emissivity signatures using a hyperspectral TIR imaging device in a ground-based experiment. Furthermore, spectral emissivity could be determined as an equally sensitive measure of plant water stress in comparison to traditional temperature-based indices. The water-stressed plants showed an overall spectral increase in emissivity

in comparison to the control group. Without any further analysis of plant structural or biochemical characteristics (*e.g.*, leaf constituents, cuticle thickness) the examined overall increase in emissivity is in good agreement with the findings of Buitrago *et al.* (2016) and Buitrago Acevedo *et al.* (2017). They showed that cold and water stress induced variations in leaf traits (*i.e.*, leaf water content, lignin, cellulose and leaf area), which are correlated to changes in their emissivity spectra.

#### **Objective IV: Assess the effect of plant species on spectral emissivity**

In Chapter V a further ground-based experiment was conducted to gain deeper insights into how different plant species affect the spectral emissivity signature.

As a first finding, this study demonstrated that plant emissivity spectra as measured by Telops *Hyper-Cam LW* are of very high quality and showed a good reproducibility compared to DHR reference measurement in the laboratory (*i.e.*, Bruker Vertex 70, ITC). Concerning the application of spectral emissivity for the detection of plant water stress, the main finding of this experiment was that different plant species exhibit distinct spectral emissivity features. This offers the opportunity to use the information of spectral emissivity to discriminate plant species. It was impressively demonstrated that different species could be more accurately classified based on species-specific spectral emissivity features than on VNIR/SWIR spectral reflectance features. However, the fact that emissivity spectra of vegetation are not only affected by the actual plant status but also show species-related spectral features complicates the further understanding of how stress-related changes in leaf traits are associated with distinct spectral emissivity features, which could potentially be used to detect environmental stresses. Thus, the species-specific spectral features need to be taken into account for further stress-related research on spectral emissivity signatures.

## 2. Conclusion & Outlook

In this thesis, it has been demonstrated that both key variables from the TIR spectral domain, surface temperature and spectral emissivity, could be used for the detection of plant responses to water stress: (i) temperature-based indices (*e.g.*, CWSI) retrieved from Telops *Hyper-Cam LW* images were more suitable for the detection of plant responses to water stress than traditional VNIR/SWIR indices (*e.g.*, PRI) and SIF indices, (ii) for the first time, spectral emissivity as measured by a hyperspectral TIR imaging instrument has been used to detect plant water stress. In conclusion, evidence about the application of hyperspectral TIR remote sensing to detect plant water stress was provided at ground- and airborne level.

In comparison to VNIR/SWIR indices, temperature-based indices provide an appropriate pre-visual proxy for the detection of plant responses to water stress, which already has been demonstrated earlier by Zarco-Tejada *et al.* (2013) and Panigada *et al.* (2014). Therefore, TIR indices have an enormous potential to be applied in precision agriculture and especially in irrigation management to determine the right time, the right place and the right amount of water to apply to reduce the amount of water used per unit yield. However, it is still unclear when to irrigate the fields and how much water the crops need. CWSI is pointed out to be applicable for the detection of crop water stress in different crop types, seasonal growing stages and even various climates. Notwithstanding, further research is needed to establish generally accepted calculations of CWSI to determine thresholds for irrigation scheduling. In particular, CWSI can be estimated following various approaches from the analytical CWSI to the use of artificial reference surfaces for the calculation of  $T_{wet}$  and  $T_{dry}$ . In addition, crop-specific thresholds of CWSI are needed to consider plant-specific strategies to environmental stresses such as various leaf structural architectures (*e.g.*, hypo- or amphi-stomatous leaves, cuticle thickness, trichomes). Since the temperature differences between stressed and non-stressed plants are low in cold and humid climates due to the low VPD, further care must be taken when applying thresholds of CWSI in more temperate climate zones (Costa *et al.*, 2013; Jones, 1999a).

As a potential alternative to overcome the limitations of temperature-based indices, physically-based model approaches like STIC (Mallick *et al.*, 2015) offer the opportunity to calculate actual ET values based on remotely sensed surface temperatures. ET is a direct and absolute measure of plant-atmosphere interactions and thus, can be applied as a proxy for plant water stress detection.

Current advances in sensor technology have opened the opportunity for imaging hyperspectral remote sensing of vegetation in the TIR spectral domain and thus to use spectral emissivity for the detection of environmental stresses. However, only a few studies have been conducted that examine spectral emissivity in remote sensing of vegetation. In this thesis, it has been demonstrated that specific spectral features in the TIR signature are related to various plant species (see Chapter V). Furthermore, water

stress could be detected through changes in spectral emissivity (see Chapter III). Additional studies by Buitrago *et al.* (2016) and Buitrago Acevedo *et al.* (2017) provided promising results on the relation between leaf structural or biochemical characteristics and leaf emissivity spectra.

However, the utility of spectral emissivity for the detection of plant responses to environmental stresses is limited. For example, it is still unknown which physiological and biochemical processes cause changes in the spectral emissivity and how they are related. Although Ribeiro da Luz and Crowley (2010) were able to measure spectral emissivity features of different tree species at airborne level, scaling effects (*e.g.*, mixed pixel, cavity effects) on spectral emissivity features are still largely unknown. Furthermore, current TIR satellites do not accomplish the requirements (*i.e.*, high SNR, high spectral and spatial resolution) to measure the low spectral contrast emissivity features of vegetation from space. Therefore, further fundamental research is absolutely needed to better understand the relations between the spectral emissivity features and changes in leaf traits under environmental stress conditions at different remote sensing scales.

In fact, the large-scale application of TIR remote sensing for the detection of environmental stresses as an input for precision farming underlies several limitations. The main challenges of both the temperature- and emissivity approach for the detection of crop water stress at airborne- and satellite level are associated with sensor related technical limitations and scale effects. From the technical side, instrument SNR, atmospheric correction and TES are the most challenging tasks to be solved. Meanwhile, scale effects are dealing with constraints originating from mixed pixels and canopy structure-related factors such as scattering, re-radiation and cavity effects (Thomas Udelhoven *et al.*, 2017). For example, the disaggregation of crop temperature from the much warmer soil pixels is of great interest for the accuracy of temperature-based indices as retrieved from airborne- and satellite platforms (Zhan *et al.*, 2013). However, since the pre-processing of TIR data is essential for the retrieval of both spectral emissivity and surface temperature, the major limitation of hyperspectral TIR remote sensing from airborne- and satellite platforms persists in the lack of appropriate data processing schemes. Therefore, further research is especially needed in the development and implementation of solid atmospheric correction processing schemes and TES algorithms. Since hyperspectral remote sensing in the TIR is currently limited to ground- and airborne level and thus only available for small-scale studies, there is a demand for hyperspectral satellite TIR missions with regional or global coverage. Hence, satellite mission designs like HiTeSEM (High-resolution Temperature and Spectral Emissivity Mapping, Udelhoven *et al.*, 2017) provide very promising perspectives towards the application of hyperspectral TIR for the detection of environmental stresses from space. Furthermore, the ECOSTRESS instrument on ISS will offer first prospects for future TIR satellite missions.

With regards to precision agriculture and the ultimate goal of reducing the amount of water used per unit yield, this thesis provides a comparative assessment for the detection of plant responses to water

stress using hyperspectral imaging remote sensing. Especially temperature-based indices were found to be most suitable for remotely sensed water stress detection. Notwithstanding, the detection of the cause responsible for plant physiological or biochemical changes remains complex based on a single source of remotely sensed information, since environmental stresses occur simultaneously under natural conditions. Therefore, a multi-sensor approach provides deeper insights into the relationship between plant responses to environmental stresses and their impact on the signal as measured by hyperspectral imaging remote sensing instruments.





## References

- Acosta, M., Juszczak, R., Chojnicki, B., Pavelka, M., Havránková, K., Lesny, J., Krupková, L., Urbaniak, M., Macháčová, K., Olejnik, J., 2017. CO<sub>2</sub> Fluxes from Different Vegetation Communities on a Peatland Ecosystem. *Wetlands*. <https://doi.org/10.1007/s13157-017-0878-4>
- Alonso, L., Gomez-Chova, L., Vila-Frances, J., Amoros-Lopez, J., Guanter, L., Calpe, J., Moreno, J., 2008. Improved Fraunhofer Line Discrimination Method for Vegetation Fluorescence Quantification. *IEEE Geosci. Remote Sens. Lett.* 5, 620–624. <https://doi.org/10.1109/LGRS.2008.2001180>
- Anderson, D.B., 1936. Relative Humidity or Vapor Pressure Deficit. *Ecology* 17, 277–282. <https://doi.org/10.2307/1931468>
- Ashourloo, D., Mobasheri, M.R., Huete, A., 2014. Evaluating the effect of different wheat rust disease symptoms on vegetation indices using hyperspectral measurements. *Remote Sens.* 6, 5107–5123. <https://doi.org/10.3390/rs6065107>
- Asner, G.P., 1998. Biophysical and Biochemical Sources of Variability in Canopy Reflectance. *Remote Sens. Environ.* 64, 234–253. [https://doi.org/10.1016/S0034-4257\(98\)00014-5](https://doi.org/10.1016/S0034-4257(98)00014-5)
- Asrar, G., Fuchs, M., Kanemasu, E.T., Hatfield, J.L., 1984. Estimating Absorbed Photosynthetic Radiation and Leaf Area Index from Spectral Reflectance in Wheat. *Agron. J.* 76, 300. <https://doi.org/10.2134/agronj1984.00021962007600020029x>
- Atzberger, C., 2013. Advances in Remote Sensing of Agriculture: Context Description, Existing Operational Monitoring Systems and Major Information Needs. *Remote Sens.* 5, 949–981. <https://doi.org/10.3390/rs5020949>
- Balick, L., Gillespie, A.R., French, A., Danilina, I., Allard, J.-P., Mushkin, A., 2009. Longwave Thermal Infrared Spectral Variability in Individual Rocks. *IEEE Geosci. Remote Sens. Lett.* 6, 52–56. <https://doi.org/10.1109/LGRS.2008.2006005>
- Berk, A., Anderson, G.P., Acharya, P.K., Bernstein, L.S., Muratov, L., Lee, J., Fox, M., Adler-Golden, S.M., Chetwynd, J.H., Hoke, M.L., Lockwood, R.B., Gardner, J.A., Cooley, T.W., Borel, C.C., Lewis, P.E., 2005. MODTRAN 5: a reformulated atmospheric band model with auxiliary species and practical multiple scattering options: update, in: Shen, S.S., Lewis, P.E. (Eds.), *Remote Sensing of Clouds and the Atmosphere IX*. International Society for Optics and Photonics, p. 78–85 (5571). <https://doi.org/10.1117/12.606026>

- Berni, J., Zarco-Tejada, P.J., Suarez, L., Fereres, E., 2009. Thermal and Narrowband Multispectral Remote Sensing for Vegetation Monitoring From an Unmanned Aerial Vehicle. *IEEE Trans. Geosci. Remote Sens.* 47, 722–738. <https://doi.org/10.1109/TGRS.2008.2010457>
- Blackman, R.B., Tukey, J.W., 1958. The Measurement of Power Spectra from the Point of View of Communications Engineering, *Bell System Technical Journal*. New York: Dover. <https://doi.org/10.1002/j.1538-7305.1958.tb03874.x>
- Borel, C., 1997. Iterative Retrieval of Surface Emissivity and Temperature for a Hyperspectral Sensor.
- Borel, C.C., 2003. ARTEMISS – an Algorithm to Retrieve Temperature and Emissivity from Hyperspectral Thermal Image Data, in: 28th Annual GOMACTech Conference, Hyperspectral Imaging Session, March 31, 2003 to April 3, 2003 Tampa, Florida. pp. 3–6.
- Bradford, K.J., Hsiao, T.C., 1982. Physiological Responses to Moderate Water Stress, in: Lange, O.L., Nobel, P.S., Osmond, C.B., Ziegler, H. (Eds.), *Physiological Plant Ecology II*. Springer Berlin Heidelberg, Berlin, Heidelberg, pp. 263–324. [https://doi.org/10.1007/978-3-642-68150-9\\_10](https://doi.org/10.1007/978-3-642-68150-9_10)
- Bray, E.A., 1997. Plant responses to water deficit. *Trends Plant Sci.* 2, 48–54.
- Breiman, L., 2001. Random forests. *Mach. Learn.* 45, 5–32. <https://doi.org/10.1023/A:1010933404324>
- Buddenbaum, H., Rock, G., Hill, J., Werner, W., 2015. Measuring Stress Reactions of Beech Seedlings with PRI, Fluorescence, Temperatures and Emissivity from VNIR and Thermal Field Imaging Spectroscopy. *Eur. J. Remote Sens.* 263–282. <https://doi.org/10.5721/EuJRS20154815>
- Buitrago, M.F., Groen, T.A., Hecker, C.A., Skidmore, A.K., 2016. Changes in thermal infrared spectra of plants caused by temperature and water stress. *ISPRS J. Photogramm. Remote Sens.* 111, 22–31. <https://doi.org/10.1016/j.isprsjprs.2015.11.003>
- Buitrago Acevedo, M.F., Groen, T.A., Hecker, C.A., Skidmore, A.K., 2017. Identifying leaf traits that signal stress in TIR spectra. *ISPRS J. Photogramm. Remote Sens.* 125, 132–145. <https://doi.org/10.1016/j.isprsjprs.2017.01.014>
- Carter, A., Ramsey, M., 2010. Long-term volcanic activity at Shiveluch volcano: Nine years of ASTER spaceborne thermal infrared observations. *Remote Sens.* 2, 2571–2583. <https://doi.org/10.3390/rs2112571>
- Carvalho, S., Schlerf, M., van der Putten, W.H., Skidmore, A.K., 2013. Hyperspectral reflectance of leaves and flowers of an outbreak species discriminates season and successional stage of vegetation. *Int. J. Appl. Earth Obs. Geoinf.* 24, 32–41. <https://doi.org/10.1016/j.jag.2013.01.005>
- Chaerle, L., Van Der Straeten, D., 2000. Imaging techniques and the early detection of plant stress. *Trends Plant Sci.* 5, 495–501. [https://doi.org/10.1016/S1360-1385\(00\)01781-7](https://doi.org/10.1016/S1360-1385(00)01781-7)

- Chaves, M.M., Oliveira, M.M., 2004. Mechanisms underlying plant resilience to water deficits: prospects for water-saving agriculture. *J. Exp. Bot.* 55, 2365–84. <https://doi.org/10.1093/jxb/erh269>
- Chaves, M.M., Pereira, J.S., Maroco, J., Rodrigues, M.L., Ricardo, C.P.P., Osório, M.L., Carvalho, I., Faria, T., Pinheiro, C., 2002. How Plants Cope with Water Stress in the Field. *Photosynthesis and Growth. Ann. Bot.* 89, 907–916. <https://doi.org/10.1093/aob/mcf105>
- Chiwaki, K., Nagamori, S., Inoue, Y., 2005. Predicting bacterial wilt disease of tomato plants using remotely sensed thermal imagery. *J. Agric. Meteorol.* 61, 153–164. <https://doi.org/10.2480/agrmet.61.153>
- Chojnicki, B.H., Michalak, M., Acosta, M., Juszczak, R., Augustin, J., Drösler, M., Olejnik, J., 2010. Measurements of Carbon Dioxide Fluxes by Chamber Method at the Rzecin Wetland Ecosystem, Poland. *Polish J. Environ. Stud.* 19, 283–291.
- Christensen, P.R., Bandfield, J.L., Hamilton, V.E., Howard, D. a., Lane, M.D., Piatek, J.L., Ruff, S.W., Stefanov, W.L., 2000. A thermal emission spectral library of rock-forming minerals. *J. Geophys. Res.* 105, 9735. <https://doi.org/10.1029/1998JE000624>
- Christensen, P.R., Bandfield, J.L., Hamilton, V.E., Ruff, S.W., Kieffer, H.H., Titus, T.N., Malin, M.C., Morris, R. V., Lane, M.D., Clark, R.L., Jakosky, B.M., Mellon, M.T., Pearl, J.C., Conrath, B.J., Smith, M.D., Clancy, R.T., Kuzmin, R.O., Roush, T., Mehall, G.L., Gorelick, N., Bender, K., Murray, K., Dason, S., Greene, E., Silverman, S., Greenfield, M., 2001. Mars Global Surveyor Thermal Emission Spectrometer experiment: Investigation description and surface science results. *J. Geophys. Res. Planets* 106, 23823–23871. <https://doi.org/10.1029/2000JE001370>
- Cohen, Y., Alchanatis, V., Meron, M., Saranga, Y., Tsipris, J., 2005. Estimation of leaf water potential by thermal imagery and spatial analysis. *J. Exp. Bot.* 56, 1843–52. <https://doi.org/10.1093/jxb/eri174>
- Costa, J.M., Grant, O.M., Chaves, M.M., 2013. Thermography to explore plant-environment interactions. *J. Exp. Bot.* 64, 3937–49. <https://doi.org/10.1093/jxb/ert029>
- Dalla Costa, L., Delle Vedove, G., Gianquinto, G., Giovanardi, R., Peressotti, A., 1997. Yield, water use efficiency and nitrogen uptake in potato: influence of drought stress. *Potato Res.* 40, 19–34. <https://doi.org/10.1007/BF02407559>
- Danilina, I., Gillespie, A.R., Balick, L.K., Mushkin, A., O’Neal, M.A., 2012. Performance of a thermal-infrared radiosity and heat-diffusion model for estimating sub-pixel radiant temperatures over the course of a day. *Remote Sens. Environ.* 124, 492–501. <https://doi.org/10.1016/j.rse.2012.05.028>

- Dorigo, W., Bachmann, M., Heldens, W., 2006. AS Toolbox & Processing of field spectra, User's manual (No. Version 1.13, December 2006). German Aerospace Center (DLR), Oberpfaffenhofen, 82234 Wessling, Germany.
- Eisele, A., Lau, I., Hewson, R., Carter, D., Wheaton, B., Ong, C., Cudahy, T.J., Chabrillat, S., Kaufmann, H., 2012. Applicability of the Thermal Infrared Spectral Region for the Prediction of Soil Properties Across Semi-Arid Agricultural Landscapes. *Remote Sens.* 4, 3265–3286. <https://doi.org/10.3390/rs4113265>
- Elvidge, C.D., 1988. Thermal infrared reflectance of dry plant materials: 2.5–20.0  $\mu\text{m}$ . *Remote Sens. Environ.* 26, 265–285. [https://doi.org/10.1016/0034-4257\(88\)90082-X](https://doi.org/10.1016/0034-4257(88)90082-X)
- Fabre, S., Lesaignoux, A., Olioso, A., Briottet, X., 2011. Influence of Water Content on Spectral Reflectance of Leaves in the 3 - 15  $\mu\text{m}$  Domain. *IEEE Geosci. Remote Sens. Lett.* 8, 143–147. <https://doi.org/10.1109/LGRS.2010.2053518>
- Fereres, E., Evans, R.G., 2006. Irrigation of fruit trees and vines: an introduction. *Irrig. Sci.* 24, 55–57. <https://doi.org/10.1007/s00271-005-0019-3>
- Fluke Corporation, 2010. Ti9, Ti10, Ti25, TiRx, TiR and TiR1: Users manual.
- Francini, A., Lorenzini, G., Nali, C., 2011. The antitranspirant Di-1-p-menthene, a potential chemical protectant of ozone damage to plants. *Water. Air. Soil Pollut.* 219, 459–472. <https://doi.org/10.1007/s11270-010-0720-6>
- French, A., Schmugge, T., Ritchie, J., Hsu, A., Jacob, F., Ogawa, K., 2008. Detecting land cover change at the Jornada Experimental Range, New Mexico with ASTER emissivities. *Remote Sens. Environ.* 112, 1730–1748. <https://doi.org/10.1016/j.rse.2007.08.020>
- Frey, C.M., Parlow, E., 2012. Flux measurements in Cairo. Part 2: On the determination of the spatial radiation and energy balance using ASTER satellite data. *Remote Sens.* 4, 2635–2660. <https://doi.org/10.3390/rs4092635>
- Fuchs, M., Tanner, C.B., 1966. Infrared Thermometry of Vegetation. *Agron. J.* 58, 597. <https://doi.org/10.2134/agronj1966.00021962005800060014x>
- Gamon, J., Peñuelas, J., Field, C., 1992. A narrow-waveband spectral index that tracks diurnal changes in photosynthetic efficiency. *Remote Sens. Environ.* 41, 35–44. [https://doi.org/10.1016/0034-4257\(92\)90059-S](https://doi.org/10.1016/0034-4257(92)90059-S)
- Gao, B.C., 1996. NDWI - A normalized difference water index for remote sensing of vegetation liquid water from space. *Remote Sens. Environ.* 58, 257–266. [https://doi.org/10.1016/S0034-4257\(96\)00067-3](https://doi.org/10.1016/S0034-4257(96)00067-3)

- Gebbers, R., Adamchuk, V.I., 2010. Precision Agriculture and Food Security. *Science* (80-. ). 327, 828–831. <https://doi.org/10.1126/science.1183899>
- Gerhards, M., Rock, G., Schlerf, M., Udelhoven, T., 2016. Water stress detection in potato plants using leaf temperature, emissivity, and reflectance. *Int. J. Appl. Earth Obs. Geoinf.* 53, 27–39. <https://doi.org/10.1016/j.jag.2016.08.004>
- Gillespie, A.R., 1992. Spectral Mixture Analysis of Multispectral Thermal Infrared Images.pdf. *Remote Sens. Environ.* 42, 137–145.
- Gillespie, A.R., Rokugawa, S., Matsunaga, T., Cothorn, J.S., Hook, S., Kahle, A.B., 1998. A temperature and emissivity separation algorithm for Advanced Spaceborne Thermal Emission and Reflection Radiometer (ASTER) images. *IEEE Trans. Geosci. Remote Sens.* 36, 1113–1126. <https://doi.org/10.1109/36.700995>
- Gonzalez-Dugo, V., Durand, J.L., Gastal, F., 2010. Water deficit and nitrogen nutrition of crops. A review. *Agron. Sustain. Dev.* 30, 529–544. <https://doi.org/10.1051/agro/2009059>
- Gonzalez-Dugo, V., Zarco-Tejada, P., Nicolás, E., Nortes, P. a., Alarcón, J.J., Intrigliolo, D.S., Fereres, E., 2013. Using high resolution UAV thermal imagery to assess the variability in the water status of five fruit tree species within a commercial orchard. *Precis. Agric.* 14, 660–678. <https://doi.org/10.1007/s11119-013-9322-9>
- Govender, M., Chetty, K., Bulcock, H., 2007. A review of hyperspectral remote sensing and its application in vegetation and water resource studies 33.
- Govender, M., Dye, P., Weiersbye, I., 2009. Review of commonly used remote sensing and ground-based technologies to measure plant water stress. *Water SA* 35, 741–752. <https://doi.org/http://dx.doi.org/10.4314/wsa.v35i5.49201>
- Grant, O.M., Chaves, M.M., Jones, H.G., 2006. Optimizing thermal imaging as a technique for detecting stomatal closure induced by drought stress under greenhouse conditions. *Physiol. Plant.* 127, 507–518. <https://doi.org/10.1111/j.1399-3054.2006.00686.x>
- Grant, O.M., Davies, M.J., James, C.M., Johnson, A.W., Leinonen, I., Simpson, D.W., 2012. Thermal imaging and carbon isotope composition indicate variation amongst strawberry (*Fragaria×ananassa*) cultivars in stomatal conductance and water use efficiency. *Environ. Exp. Bot.* 76, 7–15. <https://doi.org/10.1016/j.envexpbot.2011.09.013>
- Grant, O.M., Tronina, L., Jones, H.G., Chaves, M.M., 2007. Exploring thermal imaging variables for the detection of stress responses in grapevine under different irrigation regimes. *J. Exp. Bot.* 58, 815–25. <https://doi.org/10.1093/jxb/erl153>

- Gu, D., Gillespie, A.R., Kahle, A.B., Palluconi, F.D., 2000. Autonomous atmospheric compensation (AAC) of high resolution hyperspectral thermal infrared remote-sensing imagery. *IEEE Trans. Geosci. Remote Sens.* 38, 2557–2570. <https://doi.org/10.1109/36.885203>
- Haboudane, D., Miller, J.R., Tremblay, N., Zarco-Tejada, P.J., Dextraze, L., 2002. Integrated narrow-band vegetation indices for prediction of crop chlorophyll content for application to precision agriculture. *Remote Sens. Environ.* 81, 416–426. [https://doi.org/10.1016/S0034-4257\(02\)00018-4](https://doi.org/10.1016/S0034-4257(02)00018-4)
- Hackwell, J.A., Warren, D.W., Bongiovi, R.P., Hansel, S.J., Hayhurst, T.L., Mabry, D.J., Sivjee, M.G., Skinner, J.W., 1996. LWIR/MWIR imaging hyperspectral sensor for airborne and ground-based remote sensing, in: Descour, M.R., Mooney, J.M. (Eds.), . *International Society for Optics and Photonics*, pp. 102–107. <https://doi.org/10.1117/12.258057>
- Hecker, C.A., Smith, T.E.L., da Luz, B.R., Wooster, M.J., 2013. Thermal Infrared Spectroscopy in the Laboratory and Field in Support of Land Surface Remote Sensing, in: Kuenzer, C., Dech, S. (Eds.), *Thermal Infrared Remote Sensing*. Springer Netherlands, pp. 43–67. [https://doi.org/10.1007/978-94-007-6639-6\\_3](https://doi.org/10.1007/978-94-007-6639-6_3)
- Hecker, C., Hook, S., van der Meijde, M., Bakker, W., van der Werff, H., Wilbrink, H., van Ruitenbeek, F., de Smeth, B., van der Meer, F., 2011. Thermal infrared spectrometer for Earth science remote sensing applications-instrument modifications and measurement procedures. *Sensors (Basel)*. 11, 10981–99. <https://doi.org/10.3390/s111110981>
- Hirschfeld, T., 1976. Wavenumber Scale Shift in Fourier Transform Infrared Spectrometers Due to Vignetting. *Appl. Spectrosc.* Vol. 30, Issue 5, pp. 549-550 30, 549–550.
- Hoffmann, M., Jurisch, N., Albiac Borraz, E., Hagemann, U., Drösler, M., Sommer, M., Augustin, J., 2015. Automated modeling of ecosystem CO<sub>2</sub> fluxes based on periodic closed chamber measurements: A standardized conceptual and practical approach. *Agric. For. Meteorol.* 200, 30–45. <https://doi.org/10.1016/j.agrformet.2014.09.005>
- Hook, S.J., Kahle, A.B., 1996. The Micro Fourier Transform Intefferometer ( tFTIR ) A New Field Spectrometer for Acquisition of Infrared Data of Natural Surfaces. *Remote Sens. Environ.* 56, 172–181.
- Hopkins, W.G., Hüner, N.P.A., 2009. *Introduction to Plant Physiology*, 4. ed. Hoboken, NJ : Wiley.
- Horton, K.A., Johnson, J.R., Lucey, P.G., 1998. Infrared Measurements of Pristine and Disturbed Soils 2. Environmental Effects and Field Data Reduction. *Remote Sens. Environ.* 64, 47–52. [https://doi.org/10.1016/S0034-4257\(97\)00167-3](https://doi.org/10.1016/S0034-4257(97)00167-3)
- Hsiao, T.C., 1973. Plant Responses to Water Stress. *Annu. Rev. Plant Physiol.* 24, 519–570.

- Hsiao, T.C., Fereres, E., Acevedo, E., Henderson, D.W., 1976. Water Stress and Dynamics of Growth and Yield of Crop Plants, in: Lange, O.L., Kappen, L., Schulze, E.-D. (Eds.), *Water and Plant Life* SE - 18, Ecological Studies. Springer Berlin Heidelberg, pp. 281–305. [https://doi.org/10.1007/978-3-642-66429-8\\_18](https://doi.org/10.1007/978-3-642-66429-8_18)
- Hunt Jr., E., Rock, B., 1989. Detection of changes in leaf water content using Near- and Middle-Infrared reflectances. *Remote Sens. Environ.* 30, 43–54. [https://doi.org/10.1016/0034-4257\(89\)90046-1](https://doi.org/10.1016/0034-4257(89)90046-1)
- Idso, S.B., Jackson, R.D., Pinter, P.J., Reginato, R.J., Hatfield, J.L., 1981. Normalizing the stress-degree-day parameter for environmental variability. *Agric. Meteorol.* 24, 45–55. [https://doi.org/10.1016/0002-1571\(81\)90032-7](https://doi.org/10.1016/0002-1571(81)90032-7)
- Idso, S.B., Jackson, R.D., Reginato, R.J., 1977a. Remote sensing for agricultural water management and crop yield prediction. *Agric. Water Manag.* 1, 299–310. [https://doi.org/10.1016/0378-3774\(77\)90021-X](https://doi.org/10.1016/0378-3774(77)90021-X)
- Idso, S.B., Jackson, R.D., Reginato, R.J., 1977b. Remote-Sensing of Crop Yields. *Science* (80-. ). 196, 19–25. <https://doi.org/10.1126/science.196.4285.19>
- Inoue, Y., Kimball, B.A., Jackson, R.D., Pinter, P.J., Reginato, R.J., 1990. Remote estimation of leaf transpiration rate and stomatal resistance based on infrared thermometry. *Agric. For. Meteorol.* 51, 21–33. [https://doi.org/10.1016/0168-1923\(90\)90039-9](https://doi.org/10.1016/0168-1923(90)90039-9)
- IPCC, 2007. *Climate Change 2007: The Physical Science Basis. Contribution of Working Group I to the Fourth Assessment Report of the Intergovernmental Panel on Climate Change, Climate Change 2013 - The Physical Science Basis.* Cambridge University Press, Cambridge. <https://doi.org/10.1017/CBO9781107415324.004>
- Jackson, R.D., Idso, S.B., Reginato, R.J., Pinter, P.J., 1981. Canopy temperature as a crop water stress indicator. *Water Resour. Res.* 17, 1133–1138. <https://doi.org/10.1029/WR017i004p01133>
- Jackson, R.D., Reginato, R.J., Idso, S.B., 1977. Wheat canopy temperature: A practical tool for evaluating water requirements. *Water Resour. Res.* 13, 651–656. <https://doi.org/10.1029/WR013i003p00651>
- Jacquemoud, S., Verhoef, W., Baret, F., Bacour, C., Zarco-Tejada, P.J., Asner, G.P., François, C., Ustin, S.L., 2009. PROSPECT+SAIL models: A review of use for vegetation characterization. *Remote Sens. Environ.* 113, S56–S66. <https://doi.org/10.1016/j.rse.2008.01.026>
- Jensen, J.R., 2007. *Remote Sensing of the Environment : An Earth Resource Perspective.* Pearson Prentice Hall: Upper Saddle River.



- Jiménez-Muñoz, J.C., Sobrino, J.A., Gillespie, A.R., 2012. Surface Emissivity Retrieval From Airborne Hyperspectral Scanner Data: Insights on Atmospheric Correction and Noise Removal 9. <https://doi.org/10.1109/LGRS.2011.2163699>
- Jones, H.G., 2004a. Application of Thermal Imaging and Infrared Sensing in Plant Physiology and Ecophysiology, in: *Advances in Botanical Research*. pp. 107–163. [https://doi.org/10.1016/S0065-2296\(04\)41003-9](https://doi.org/10.1016/S0065-2296(04)41003-9)
- Jones, H.G., 2004b. Irrigation scheduling: advantages and pitfalls of plant-based methods. *J. Exp. Bot.* 55, 2427–2436. <https://doi.org/10.1093/jxb/erh213>
- Jones, H.G., 1999a. Use of infrared thermometry for estimation of stomatal conductance as a possible aid to irrigation scheduling. *Agric. For. Meteorol.* 95, 139–149. [https://doi.org/10.1016/S0168-1923\(99\)00030-1](https://doi.org/10.1016/S0168-1923(99)00030-1)
- Jones, H.G., 1999b. Use of thermography for quantitative studies of spatial and temporal variation of stomatal conductance over leaf surfaces. *Plant, Cell Environ.* 22, 1043–1055.
- Jones, H.G., Schofield, P., 2008. Thermal and other remote sensing of plant stress. *Gen. Appl. Plant Physiol.* 34, 19–32.
- Jones, H.G., Serraj, R., Loveys, B.R., Xiong, L., Wheaton, A., Price, A.H., 2009a. Thermal infrared imaging of crop canopies for the remote diagnosis and quantification of plant responses to water stress in the field. *Funct. Plant Biol.* <https://doi.org/10.1071/FP09123>
- Jones, H.G., Serraj, R., Loveys, B.R., Xiong, L., Wheaton, A., Price, A.H., 2009b. Thermal infrared imaging of crop canopies for the remote diagnosis and quantification of plant responses to water stress in the field. *Funct. Plant Biol.* 36, 978. <https://doi.org/10.1071/FP09123>
- Jones, H.G., Vaughan, R.A., 2010. *Remote sensing of vegetation: principles, techniques, and applications*. Oxford University Press.
- Jordan, C.F., 1969. Derivation of Leaf-Area Index from Quality of Light on the Forest Floor. *Ecology* 50, 663–666. <https://doi.org/10.2307/1936256>
- Juszczak, R., Humphreys, E., Acosta, M., Michalak-Galczevska, M., Kayzer, D., Olejnik, J., 2013. Ecosystem respiration in a heterogeneous temperate peatland and its sensitivity to peat temperature and water table depth. *Plant Soil* 366, 505–520. <https://doi.org/10.1007/s11104-012-1441-y>
- Kahle, A.B., Alley, R.E., 1992. Separation of temperature and emittance in remotely sensed radiance measurements. *Remote Sens. Environ.* 42, 107–111. [https://doi.org/10.1016/0034-4257\(92\)90093-Y](https://doi.org/10.1016/0034-4257(92)90093-Y)

- Kealy, P.S., Hook, S.J., 1993. Separating Temperature and Emissivity in Thermal Infrared Multispectral Scanner Data: Implications. *IEEE Trans. Geosci. Remote Sens.* 31, 1155–1164.
- Khanal, S., Fulton, J., Shearer, S., 2017. An overview of current and potential applications of thermal remote sensing in precision agriculture. *Comput. Electron. Agric.* 139, 22–32. <https://doi.org/10.1016/j.compag.2017.05.001>
- King, P.L., Ramsey, M.S., McMillan, P.F., Swayze, G.A., 2004. Laboratory Fourier transform infrared spectroscopy methods for geologic samples, in: King, P.L., Ramsey, M.S., McMillan, P.F., Swayze, G.A. (Eds.), *Infrared Spectroscopy in Geochemistry, Exploration Geochemistry and Remote Sensing*. Mineralogical Association of Canada, Quebec, QC, Canada.
- Kirkland, L., Herr, K., Keim, E., Adams, P., Salisbury, J., Hackwell, J., Treiman, A., 2002. First use of an airborne thermal infrared hyperspectral scanner for compositional mapping. *Remote Sens. Environ.* 80, 447–459. [https://doi.org/10.1016/S0034-4257\(01\)00323-6](https://doi.org/10.1016/S0034-4257(01)00323-6)
- Korb, A.R., Dybwad, P., Wadsworth, W., Salisbury, J.W., 1996. Portable Fourier transform infrared spectroradiometer for field measurements of radiance and emissivity. *Appl. Opt.* 35, 1679. <https://doi.org/10.1364/AO.35.001679>
- Lagueux, P., Farley, V., Rolland, M., Chamberland, M., Puckrin, E., Turcotte, C.S., Lahaie, P., Dube, D., 2009. Airborne measurements in the infrared using FTIR-based imaging hyperspectral sensors, in: *2009 First Workshop on Hyperspectral Image and Signal Processing: Evolution in Remote Sensing*. IEEE, pp. 1–4. <https://doi.org/10.1109/WHISPERS.2009.5289060>
- Lang, M., Lichtenthaler, H.K., Sowinska, M., Heisel, F., Miehe, J.A., 1996. Fluorescence Imaging of Water and Temperature Stress in Plant Leaves. *J. Plant Physiol.* 148, 613–621. [https://doi.org/10.1016/S0176-1617\(96\)80082-4](https://doi.org/10.1016/S0176-1617(96)80082-4)
- Langley, S.K., Cheshire, H.M., Humes, K.S., 2001. A comparison of single date and multitemporal satellite image classifications in a semi-arid grassland. *J. Arid Environ.* 49, 401–411. <https://doi.org/10.1006/jare.2000.0771>
- Lee, C.M., Cable, M.L., Hook, S.J., Green, R.O., Ustin, S.L., Mandl, D.J., Middleton, E.M., 2015. An introduction to the NASA Hyperspectral InfraRed Imager (HyspIRI) mission and preparatory activities. *Remote Sens. Environ.* 167, 6–19. <https://doi.org/10.1016/j.rse.2015.06.012>
- Lee, W.S., Alchanatis, V., Yang, C., Hirafuji, M., Moshou, D., Li, C., 2010. Sensing technologies for precision specialty crop production. *Comput. Electron. Agric.* 74, 2–33. <https://doi.org/10.1016/j.compag.2010.08.005>
- Lenth, R. V., 2016. Least-Squares Means: The {R} Package {lsmeans}. *J. Stat. Softw.* 69, 1–33. <https://doi.org/10.18637/jss.v069.i01>

- Li, Z.-L., Tang, B.-H., Wu, H., Ren, H., Yan, G., Wan, Z., Trigo, I.F., Sobrino, J. a., 2013. Satellite-derived land surface temperature: Current status and perspectives. *Remote Sens. Environ.* 131, 14–37. <https://doi.org/10.1016/j.rse.2012.12.008>
- Lourakis, M.I.A., 2005. A Brief Description of the Levenberg-Marquardt Algorithm Implemented by levmar [WWW Document]. <http://users.ics.forth.gr/lourakis/levmar/levmar.pdf>. URL <http://users.ics.forth.gr/lourakis/levmar/levmar.pdf> (accessed 3.20.17).
- Lucey, P.G., Williams, T.J., Hinrichs, J.L., Winter, M.E., Steutel, D., Winter, E.M., 2001. Three years of operation of AHI: the University of Hawaii’s Airborne Hyperspectral Imager, in: Andresen, B.F., Fulop, G.F., Strojnik, M. (Eds.), . *International Society for Optics and Photonics*, p. 112. <https://doi.org/10.1117/12.445281>
- Maes, W.H., Baert, A., Huete, A.R., Minchin, P.E.H., Snelgar, W.P., Steppe, K., 2016. A new wet reference target method for continuous infrared thermography of vegetations. *Agric. For. Meteorol.* 226–227, 119–131. <https://doi.org/10.1016/j.agrformet.2016.05.021>
- Maes, W.H., Steppe, K., 2012. Estimating evapotranspiration and drought stress with ground-based thermal remote sensing in agriculture: a review. *J. Exp. Bot.* 63, 4671–712. <https://doi.org/10.1093/jxb/ers165>
- Mahajan, S., Tuteja, N., 2005. Cold, salinity and drought stresses: an overview. *Arch. Biochem. Biophys.* 444, 139–58. <https://doi.org/10.1016/j.abb.2005.10.018>
- Mahlein, A.-K., 2016. Present and Future Trends in Plant Disease Detection. *Plant Dis.* 100, 1–11. <https://doi.org/10.1007/s13398-014-0173-7.2>
- Maier, S.W., Günther, K.P., Stellmes, M., 2003. Sun-Induced Fluorescence: A New Tool for Precision Farming, in: Schepers, J., VanToai, T. (Eds.), *Digital Imaging and Spectral Techniques: Applications to Precision Agriculture and Crop Physiology*. American Society of Agronomy, Crop Science Society of America, and Soil Science Society of America, Madison, WI, pp. 209–222. <https://doi.org/10.2134/asaspecpub66.c16>
- Mallick, K., Boegh, E., Trebs, I., Alfieri, J.G., Kustas, W.P., Prueger, J.H., Niyogi, D., Das, N., Drewry, D.T., Hoffmann, L., Jarvis, A.J., 2015. Reintroducing radiometric surface temperature into the Penman-Monteith formulation. *Water Resour. Res.* 51, 6214–6243. <https://doi.org/10.1002/2014WR016106>
- Meron, M., Tsipris, J., Charitt, D., 2003. Remote mapping of crop water status to assess spatial variability of crop stress, in: Stafford, J., Werner, A. (Eds.), *Precision Agriculture*. Wageningen Academic Publishers. <https://doi.org/https://doi.org/10.3920/978-90-8686-514-7>

- Meroni, M., Rossini, M., Guanter, L., Alonso, L., Rascher, U., Colombo, R., Moreno, J., 2009. Remote sensing of solar-induced chlorophyll fluorescence: Review of methods and applications. *Remote Sens. Environ.* 113, 2037–2051. <https://doi.org/10.1016/j.rse.2009.05.003>
- Mikiciuk, G., Mikiciuk, M., Ptak, P., 2015. The Effects of Anitranspirant Di-1-P-Menthene on Some Physiological Traits of Strawberry. *J. Ecol. Eng.* 16, 161–167. <https://doi.org/10.12911/22998993/59366>
- Möller, M., Alchanatis, V., Cohen, Y., Meron, M., Tsipris, J., Naor, A., Ostrovsky, V., Sprintsin, M., Cohen, S., 2007. Use of thermal and visible imagery for estimating crop water status of irrigated grapevine. *J. Exp. Bot.* 58, 827–838. <https://doi.org/10.1093/jxb/erl115>
- Moran, M.S., 1994. Irrigation management in Arizona using satellites and airplanes. *Irrig. Sci.* 15, 35–44. <https://doi.org/10.1007/BF00187793>
- Morison, J.I.L., Baker, N.R., Mullineaux, P.M., Davies, W.J., 2008. Improving water use in crop production. *Philos. Trans. R. Soc. Lond. B. Biol. Sci.* 363, 639–658. <https://doi.org/10.1098/rstb.2007.2175>
- Mulla, D.J., 2013. Twenty five years of remote sensing in precision agriculture: Key advances and remaining knowledge gaps. *Biosyst. Eng.* 114, 358–371. <https://doi.org/10.1016/j.biosystemseng.2012.08.009>
- Nash, J., Sutcliffe, J., 1970. River flow forecasting through conceptual models part I — A discussion of principles. *J. Hydrol.* 10, 282–290. [https://doi.org/10.1016/0022-1694\(70\)90255-6](https://doi.org/10.1016/0022-1694(70)90255-6)
- Nicodemus, K.K., 2011. Letter to the editor: on the stability and ranking of predictors from random forest variable importance measures. *Brief. Bioinform.* 12, 369–373. <https://doi.org/10.1093/bib/bbr016>
- Nilsson, H.E., 1991. Hand-held radiometry and IR-thermography of plant diseases in field plot experiments. *Int. J. Remote Sens.* 12, 545–557. <https://doi.org/10.1080/01431169108929671>
- Ogashawara, I., Bastos, V., 2012. A Quantitative Approach for Analyzing the Relationship between Urban Heat Islands and Land Cover. *Remote Sens.* 4, 3596–3618. <https://doi.org/10.3390/rs4113596>
- Ouerghi, F., Ben-Hammouda, M., Teixeira Da Silva, J.A., Albouchi, A., Bouzaien, G., Aloui, S., Cheikh-M'hamed, H., Nasraoui, B., 2015. The Effects of Vapor Gard on some Physiological Traits of Durum Wheat and Barley Leaves under Water Stress. *Agric. Conspec. Sci.* 79, 261–267.

- OuYang, X., Wang, N., Wu, H., Li, Z., 2010. Errors analysis on temperature and emissivity determination from hyperspectral thermal infrared data. *Opt. Express* 18, 544. <https://doi.org/10.1364/OE.18.000544>
- Panigada, C., Rossini, M., Meroni, M., Cilia, C., Busetto, L., Amaducci, S., Boschetti, M., Cogliati, S., Picchi, V., Pinto, F., Marchesi, a., Colombo, R., 2014. Fluorescence, PRI and canopy temperature for water stress detection in cereal crops. *Int. J. Appl. Earth Obs. Geoinf.* 30, 167–178. <https://doi.org/10.1016/j.jag.2014.02.002>
- Pearcy, R.W., Schulze, E.-D., Zimmermann, R., 1989. Measurement of transpiration and leaf conductance, in: Robert, W.P., Ehleringer, J.R., Mooney, H.A., Rundel, P.W. (Eds.), *Plant Physiological Ecology*. Springer Netherlands, Dordrecht, pp. 137–160. [https://doi.org/10.1007/978-94-009-2221-1\\_8](https://doi.org/10.1007/978-94-009-2221-1_8)
- Peñuelas, J., Filella, I., Biel, C., Serrano, L., Savé, R., 1993. The reflectance at the 950–970 nm region as an indicator of plant water status. *Int. J. Remote Sens.* <https://doi.org/10.1080/01431169308954010>
- Peñuelas, J., Gamon, J. a, Fredeen, a L., Merino, J., Field, C.B., 1994. Reflectance indices associated with physiological changes in Nitrogen - and water - limited sunflower leaves. *Remote Sens. Environ.* 48, 135–146.
- Peñuelas, J., Pinol, J., Ogaya, R., Filella, I., 1997. Estimation of plant water concentration by the reflectance Water Index WI ( R900/R970). *Int. J. Remote Sens.* 18, 2869–2875. <https://doi.org/10.1080/014311697217396>
- Pinheiro, J., Bates, D., DebRoy, S., Sarkar, D., Team, R.C., 2017. *nlme: Linear and Nonlinear Mixed Effects Models*.
- Pinter Jr., P.J., Hatfield, J.L., Schepers, J.S., Barnes, E.M., Susan Moran, M., Jr, P.J., Susan, M., T, C.S., Paul Pinter Jr, A.J., T Daughtry, C.S., Upchurch, D.R., Pinter, P.J., Daughtry, C.S., 2003. Remote Sensing for Crop Management. *Photogramm. Eng. Remote Sens.* 69, 647–664.
- Plaut, Z., Magril, Y., Kedem, U., 2004. A new film forming material, which reduces water vapour conductance more than CO<sub>2</sub> fixation in several horticultural crops. *J. Hortic. Sci. Biotechnol.* 79, 528–532. <https://doi.org/10.1080/14620316.2004.11511800>
- Pleijel, H., Danielsson, H., Emberson, L., Ashmore, M.R., Mills, G., 2007. Ozone risk assessment for agricultural crops in Europe: Further development of stomatal flux and flux–response relationships for European wheat and potato. *Atmos. Environ.* 41, 3022–3040. <https://doi.org/10.1016/j.atmosenv.2006.12.002>

- Porcar-Castell, A., Tyystjarvi, E., Atherton, J., van der Tol, C., Flexas, J., Pfundel, E.E., Moreno, J., Frankenberg, C., Berry, J.A., 2014. Linking chlorophyll a fluorescence to photosynthesis for remote sensing applications: mechanisms and challenges. *J. Exp. Bot.* 65, 4065–4095. <https://doi.org/10.1093/jxb/eru191>
- Porporato, A., Laio, F., 2001. Plants in water-controlled ecosystems: active role in hydrologic processes and response to water stress: III. Vegetation water stress. *Adv. Water Resour.* 24, 725–744.
- Puckrin, E., Turcotte, C.S., Gagnon, M., Bastedo, J., Farley, V., Chamberland, M., 2012. Airborne infrared-hyperspectral mapping for detection of gaseous and solid targets, in: Fountain III, A.W., Gardner, P.J. (Eds.), *Proceedings of Global Geospatial Conference.* p. 766516. <https://doi.org/10.1117/12.850304>
- R Core Team, 2017. R: A language and environment for statistical computing. [WWW Document]. *R Found. Stat. Comput.* Vienna, Austria. URL <https://www.r-project.org/>
- Rascher, U., Alonso, L., Burkart, A., Cilia, C., Cogliati, S., Colombo, R., Damm, A., Drusch, M., Guanter, L., Hanus, J., Hyvärinen, T., Julitta, T., Jussila, J., Kataja, K., Kokkalis, P., Kraft, S., Kraska, T., Matveeva, M., Moreno, J., Muller, O., Panigada, C., Píkl, M., Pinto, F., Prey, L., Pude, R., Rossini, M., Schickling, A., Schurr, U., Schüttemeyer, D., Verrelst, J., Zemek, F., 2015. Sun-induced fluorescence - a new probe of photosynthesis: First maps from the imaging spectrometer HyPlant. *Glob. Chang. Biol.* 21, 4673–4684. <https://doi.org/10.1111/gcb.13017>
- Ribeiro da Luz, B., 2006. Attenuated total reflectance spectroscopy of plant leaves: a tool for ecological and botanical studies. *New Phytol.* 172, 305–18. <https://doi.org/10.1111/j.1469-8137.2006.01823.x>
- Ribeiro da Luz, B., Crowley, J.K., 2010. Identification of plant species by using high spatial and spectral resolution thermal infrared (8.0–13.5 $\mu$ m) imagery. *Remote Sens. Environ.* 114, 404–413. <https://doi.org/10.1016/j.rse.2009.09.019>
- Ribeiro da Luz, B., Crowley, J.K., 2007. Spectral reflectance and emissivity features of broad leaf plants: Prospects for remote sensing in the thermal infrared (8.0–14.0  $\mu$ m). *Remote Sens. Environ.* 109, 393–405. <https://doi.org/10.1016/j.rse.2007.01.008>
- Riederer, M., Muller, C., 2006. Biology of the plant cuticle, *Statewide Agricultural Land Use Baseline 2015.* <https://doi.org/10.1017/CBO9781107415324.004>
- Roberts, D.A., Quattrochi, D.A., Hulley, G.C., Hook, S.J., Green, R.O., 2012. Synergies between VSWIR and TIR data for the urban environment: An evaluation of the potential for the Hyperspectral Infrared Imager (HyspIRI) Decadal Survey mission. *Remote Sens. Environ.* 117, 83–101. <https://doi.org/10.1016/j.rse.2011.07.021>

- Rock, G., Gerhards, M., Schlerf, M., Hecker, C., Udelhoven, T., 2016. Plant species discrimination using emissive thermal infrared imaging spectroscopy. *Int. J. Appl. Earth Obs. Geoinf.* 53, 16–26. <https://doi.org/10.1016/j.jag.2016.08.005>
- Rockwell, B.W., Hofstra, A.H., 2008. Identification of quartz and carbonate minerals across northern Nevada using ASTER thermal infrared emissivity data - Implications for geologic mapping and mineral resource investigations in well-studied and frontier areas. *Geosphere* 4, 218. <https://doi.org/10.1130/GES00126.1>
- Rossini, M., Fava, F., Cogliati, S., Meroni, M., Marchesi, A., Panigada, C., Giardino, C., Busetto, L., Migliavacca, M., Amaducci, S., Colombo, R., 2013. Assessing canopy PRI from airborne imagery to map water stress in maize. *ISPRS J. Photogramm. Remote Sens.* 86, 168–177. <https://doi.org/10.1016/j.isprsjprs.2013.10.002>
- Rossini, M., Nedbal, L., Guanter, L., Ač, A., Alonso, L., Burkart, A., Cogliati, S., Colombo, R., Damm, A., Drusch, M., Hanus, J., Janoutova, R., Julitta, T., Kokkalis, P., Moreno, J., Novotny, J., Panigada, C., Pinto, F., Schickling, A., Schüttemeyer, D., Zemek, F., Rascher, U., 2015a. Red and far red Sun-induced chlorophyll fluorescence as a measure of plant photosynthesis. *Geophys. Res. Lett.* 42, 1632–1639. <https://doi.org/10.1002/2014GL062943>
- Rossini, M., Panigada, C., Cilia, C., Meroni, M., Busetto, L., Cogliati, S., Amaducci, S., Colombo, R., 2015b. Discriminating Irrigated and Rainfed Maize with Diurnal Fluorescence and Canopy Temperature Airborne Maps. *ISPRS Int. J. Geo-Information* 4, 626–646. <https://doi.org/10.3390/ijgi4020626>
- Roujean, J.L., Breon, F.M., 1995. Estimating PAR absorbed by vegetation from bidirectional reflectance measurements. *Remote Sens. Environ.* 51, 375–384. [https://doi.org/10.1016/0034-4257\(94\)00114-3](https://doi.org/10.1016/0034-4257(94)00114-3)
- Rouse, J.W., Haas, R.H., Deering, D.W., Schell, J.A., 1974. Monitoring the vernal advancements and retro gradation of natural vegetation, NASA/GSFC Final Report.
- Salisbury, J., D’Aria, D., 1992. Emissivity of terrestrial materials in the 8–14  $\mu\text{m}$  atmospheric window. *Remote Sens. Environ.* 106, 83–106.
- Salisbury, J.W., 1986. Preliminary measurements of leaf spectral reflectance in the 8-14  $\mu\text{m}$  region. *Int. J. Remote Sens.* 7, 1879–1886. <https://doi.org/10.1080/01431168608948981>
- Salisbury, J.W., D’Aria, D.M., 1994. Emissivity of terrestrial materials in the 3–5  $\mu\text{m}$  atmospheric window. *Remote Sens. Environ.* 47, 345–361. [https://doi.org/10.1016/0034-4257\(94\)90102-3](https://doi.org/10.1016/0034-4257(94)90102-3)

- Salisbury, J.W., Wald, A., D'Aria, D.M., 1994. Thermal-infrared remote sensing and Kirchhoff's law: 1. Laboratory measurements. *J. Geophys. Res. Solid Earth* 99, 11897–11911. <https://doi.org/10.1029/93JB03600>
- Salisbury, J.W., Walter, L.S., Vergo, N., D'Aria, D.M., 1992. Infrared (2.1-25 um) spectra of minerals. John Hopkins University Press 1991-1992, Baltimore.
- Schlerf, M., Rock, G., Lagueux, P., Ronellenfisch, F., Gerhards, M., Hoffmann, L., Udelhoven, T., 2012. A Hyperspectral Thermal Infrared Imaging Instrument for Natural Resources Applications. *Remote Sens.* 4, 3995–4009. <https://doi.org/10.3390/rs4123995>
- Schmugge, T., French, A., Ritchie, J.C., Rango, A., Pelgrum, H., 2002. Temperature and emissivity separation from multispectral thermal infrared observations. *Remote Sens. Environ.* 79, 189–198. [https://doi.org/10.1016/S0034-4257\(01\)00272-3](https://doi.org/10.1016/S0034-4257(01)00272-3)
- Schott, J., Gerace, A., Brown, S., Gartley, M., Montanaro, M., Reuter, D.C., 2012. Simulation of image performance characteristics of the landsat data continuity mission (LDCM) thermal infrared sensor (TIRS). *Remote Sens.* 4, 2477–2491. <https://doi.org/10.3390/rs4082477>
- Schulze, E., 1986. Carbon Dioxide and Water Vapor Exchange in Response to Drought in the Atmosphere and in the Soil. *Annu. Rev. Plant Physiol.* 37, 247–74.
- Seelig, H.-D., Hoehn, A., Stodieck, L.S., Klaus, D.M., Adams, W.W., Emery, W.J., 2008. Relations of remote sensing leaf water indices to leaf water thickness in cowpea, bean, and sugarbeet plants. *Remote Sens. Environ.* 112, 445–455. <https://doi.org/10.1016/j.rse.2007.05.002>
- Silverstein, M.R., Webster, F.X., Kiemle, D.J., 2005. Spectrometric identification of organic compounds, 7th ed. John Wiley & Sons, Inc., Hoboken, NJ. [https://doi.org/10.1016/0022-2860\(76\)87024-X](https://doi.org/10.1016/0022-2860(76)87024-X)
- Sobrino, J.A., Jiménez-Muñoz, J.C., Sòria, G., Romaguera, M., Guanter, L., Moreno, J., Plaza, A., Martínez, P., 2008. Land surface emissivity retrieval from different VNIR and TIR sensors. *IEEE Trans. Geosci. Remote Sens.* 46, 316–327. <https://doi.org/10.1109/TGRS.2007.904834>
- Sobrino, J.A., Jiménez-Muñoz, J.C., Zarco-Tejada, P.J., Sepulcre-Cantó, G., de Miguel, E., 2006. Land surface temperature derived from airborne hyperspectral scanner thermal infrared data. *Remote Sens. Environ.* 102, 99–115. <https://doi.org/10.1016/j.rse.2006.02.001>
- Stavros, E.N., Schimel, D., Pavlick, R., Serbin, S., Swann, A., Duncanson, L., Fisher, J.B., Fassnacht, F., Ustin, S., Dubayah, R., Schweiger, A., Wennberg, P., 2017. ISS observations offer insights into plant function. *Nat. Publ. Gr.* 1, 1–4. <https://doi.org/10.1038/s41559-017-0194>



- Struthers, R., Ivanova, A., Tits, L., Swennen, R., Coppin, P., 2015. Thermal infrared imaging of the temporal variability in stomatal conductance for fruit trees. *Int. J. Appl. Earth Obs. Geoinf.* 39, 9–17. <https://doi.org/10.1016/j.jag.2015.02.006>
- Suárez, L., Zarco-Tejada, P.J., Berni, J. a. J., González-Dugo, V., Fereres, E., 2009. Modelling PRI for water stress detection using radiative transfer models. *Remote Sens. Environ.* 113, 730–744. <https://doi.org/10.1016/j.rse.2008.12.001>
- Suárez, L., Zarco-Tejada, P.J., González-Dugo, V., Berni, J.A.J., Sagardoy, R., Morales, F., Fereres, E., 2010. Detecting water stress effects on fruit quality in orchards with time-series PRI airborne imagery. *Remote Sens. Environ.* 114, 286–298. <https://doi.org/10.1016/j.rse.2009.09.006>
- Suárez, L., Zarco-Tejada, P.J., Sepulcre-Cantó, G., Pérez-Priego, O., Miller, J.R., Jiménez-Muñoz, J.C., Sobrino, J., 2008. Assessing canopy PRI for water stress detection with diurnal airborne imagery. *Remote Sens. Environ.* 112, 560–575. <https://doi.org/10.1016/j.rse.2007.05.009>
- Tanner, C.B., 1963. Plant Temperatures. *Agron. J.* 55, 210. <https://doi.org/10.2134/agronj1963.00021962005500020043x>
- Tilman, D., Balzer, C., Hill, J., Befort, B.L., 2011. Global food demand and the sustainable intensification of agriculture. *Proc. Natl. Acad. Sci. U. S. A.* 108, 20260–4. <https://doi.org/10.1073/pnas.1116437108>
- Tucker, C.J., 1980. Remote sensing of leaf water content in the near infrared. *Remote Sens. Environ.* 10, 23–32. [https://doi.org/10.1016/0034-4257\(80\)90096-6](https://doi.org/10.1016/0034-4257(80)90096-6)
- Udelhoven, T., Schlerf, M., Segl, K., Mallick, K., Bossung, C., Retzlaff, R., Rock, G., Fischer, P., Müller, A., Storch, T., Eisele, A., Weise, D., Hupfer, W., Knigge, T., 2017. A Satellite-Based Imaging Instrumentation Concept for Hyperspectral Thermal Remote Sensing. *Sensors* 17, 1542. <https://doi.org/10.3390/s17071542>
- Ullah, S., Groen, T. a, Schlerf, M., Skidmore, A.K., Nieuwenhuis, W., Vaiphasa, C., 2012a. Using a genetic algorithm as an optimal band selector in the mid and thermal infrared (2.5–14  $\mu\text{m}$ ) to discriminate vegetation species. *Sensors (Basel)*. 12, 8755–69. <https://doi.org/10.3390/s120708755>
- Ullah, S., Schlerf, M., Skidmore, A.K., Hecker, C., 2012b. Identifying plant species using mid-wave infrared (2.5–6 $\mu\text{m}$ ) and thermal infrared (8–14 $\mu\text{m}$ ) emissivity spectra. *Remote Sens. Environ.* 118, 95–102. <https://doi.org/10.1016/j.rse.2011.11.008>
- United Nations, 2015a. World Population Prospects: The 2015 Revision, Key Findings and Advance Tables (No. No. ESA/P/WP.241), United Nations Department of Economic and Social Affairs, Population Division. Working Paper No. ESA/P/WP.241. New York, NY.

- United Nations, 2015b. *Transforming our World: The 2030 Agenda for Sustainable Development*. New York, NY.
- Ustin, S.L., Gamon, J.A., 2010. Remote sensing of plant functional types. *New Phytol.* 186, 795–816. <https://doi.org/10.1111/j.1469-8137.2010.03284.x>
- van der Meer, F.D., van der Werff, H.M. a., van Ruitenbeek, F.J. a., Hecker, C. a., Bakker, W.H., Noomen, M.F., van der Meijde, M., Carranza, E.J.M., Smeth, J.B. De, Woldai, T., 2012. Multi- and hyperspectral geologic remote sensing: A review. *Int. J. Appl. Earth Obs. Geoinf.* 14, 112–128. <https://doi.org/10.1016/j.jag.2011.08.002>
- Vaughan, R.G., Calvin, W.M., Taranik, J. V., 2003. SEBASS hyperspectral thermal infrared data: surface emissivity measurement and mineral mapping. *Remote Sens. Environ.* 85, 48–63. [https://doi.org/10.1016/S0034-4257\(02\)00186-4](https://doi.org/10.1016/S0034-4257(02)00186-4)
- Verhoef, W., Bach, H., 2003. Simulation of hyperspectral and directional radiance images using coupled biophysical and atmospheric radiative transfer models. *Remote Sens. Environ.* 87, 23–41. [https://doi.org/10.1016/S0034-4257\(03\)00143-3](https://doi.org/10.1016/S0034-4257(03)00143-3)
- Verrelst, J., van der Tol, C., Magnani, F., Sabater, N., Rivera, J.P., Mohammed, G., Moreno, J., 2016. Evaluating the predictive power of sun-induced chlorophyll fluorescence to estimate net photosynthesis of vegetation canopies: A SCOPE modeling study. *Remote Sens. Environ.* 176, 139–151. <https://doi.org/10.1016/j.rse.2016.01.018>
- Vollmer, M., Möllmann, K.-P., 2010. *Infrared thermal imaging: fundamentals, research and applications*. Wiley-VCH; Wiley InterScience (Online service).
- Wang, X., Ouyang, X., Tang, B., Li, Z., Zhang, R., Ensps, L., Brant, B.S., 2008. a New Method for Temperature / Emissivity Separation From Hyperspectral Thermal Infrared Data. *Sci. York* 286–289.
- White, M.A., Hoffman, F., Hargrove, W.W., Nemani, R.R., 2005. A global framework for monitoring phenological responses to climate change. *Geophys. Res. Lett.* 32, n/a-n/a. <https://doi.org/10.1029/2004GL021961>
- Wieneke, S., Ahrends, H., Damm, A., Pinto, F., Stadler, A., Rossini, M., Rascher, U., 2016. Airborne based spectroscopy of red and far-red sun-induced chlorophyll fluorescence : Implications for improved estimates of gross primary productivity. *Remote Sens. Environ.* 184, 654–667. <https://doi.org/10.1016/j.rse.2016.07.025>
- Wilson, E.B., Decius, J.C., Cross, P.C., Sundheim, B.R., 1955. *Molecular Vibrations: The Theory of Infrared and Raman Vibrational Spectra*. *J. Electrochem. Soc.* 102, 235C. <https://doi.org/10.1149/1.2430134>

- Yordanov, I., Velikova, V., Tsonev, T., 2003. Plant Responses To Drought and Stress Tolerance. *Bulg. J. Plant Physiol* 187–206. <https://doi.org/10.1023/A:1007201411474>
- Young, S.J., 2002. An in-scene method for atmospheric compensation of thermal hyperspectral data. *J. Geophys. Res.* 107, 4774. <https://doi.org/10.1029/2001JD001266>
- Zarco-Tejada, P.J., González-Dugo, V., Berni, J. a. J., 2012. Fluorescence, temperature and narrow-band indices acquired from a UAV platform for water stress detection using a micro-hyperspectral imager and a thermal camera. *Remote Sens. Environ.* 117, 322–337. <https://doi.org/10.1016/j.rse.2011.10.007>
- Zarco-Tejada, P.J., González-Dugo, V., Williams, L.E., Suárez, L., Berni, J. a. J., Goldhamer, D., Fereres, E., 2013. A PRI-based water stress index combining structural and chlorophyll effects: Assessment using diurnal narrow-band airborne imagery and the CWSI thermal index. *Remote Sens. Environ.* 138, 38–50. <https://doi.org/10.1016/j.rse.2013.07.024>
- Zhan, W., Chen, Y., Zhou, J., Wang, J., Liu, W., Voogt, J., Zhu, X., Quan, J., Li, J., 2013. Disaggregation of remotely sensed land surface temperature: Literature survey, taxonomy, issues, and caveats. *Remote Sens. Environ.* 131, 119–139. <https://doi.org/10.1016/j.rse.2012.12.014>



## Curriculum Vitae

**Max Gerhards**

Address                      Dietrichstraße 4  
   D-54290 Trier  
   Germany

Contact                      max.gerhards@yahoo.de  
   +49 160 9388 3686

Date of Birth                      01.12.1985

Place of Birth                      Wied (Westerwald), Germany

### Professional Experience

---

01/2018 – present	<b>University of Trier, Faculty VI</b> Trier, Germany Department of Environmental Remote Sensing & Geoinformatics <i>Post-doc, research assistant</i>
07/2013 – 07/2017	<b>LIST (Luxembourg Institute of Science and Technology)</b> Belvaux, Luxembourg Department of Environmental Research and Innovation (ERIN) <i>Ph.D. candidate (PLANTSSENS project)</i>
07/2010 – 09/2010	<b>GAF AG</b> , Munich, Germany <i>Internship</i>

---

### Academic Career

---

07/2013 – present	<b>University of Trier, Faculty VI</b> , Trier, Germany Department of Environmental Remote Sensing & Geoinformatics <i>Ph.D. candidate, research assistant</i>
04/2016 – 03/2013	<b>University of Trier, Faculty VI</b> , Trier, Germany <i>Diploma in Applied Physical Geography</i> minor subjects: Remote Sensing and Cartography overall grade: 1.0 - ‘with distinction’ Diploma thesis: ‘Grundlagen und erste Anwendungen hyperspektraler Thermalfernerkundung auf Laborebene und am Beispiel des Trierer Doms’ Supervisors: Prof. Dr. Thomas Udelhoven, Prof. Dr.-Ing. Markus Casper
08/1996—03/2005	<b>Secondary School</b> (Priv. Gymnasium), Marienstatt, Germany
08/1992 – 07/1996	<b>Primary school</b> , Müschenbach, Germany

---

### **Publications (peer-reviewed)**

---

- 2017 (submitted)      **Gerhards, M.**, Schlerf, M., Rascher, U., Udelhoven, T., Juszczak, R., Alberti, G., Miglietta, F., and A., Inoue, Y. (2017, *submitted*): A Comparative Analysis for Remote Sensing of Plant Water Stress Symptoms Based on Airborne Optical and Thermal Hyperspectral Images. Submitted to *International Journal of Applied Earth Observation and Geoinformation*.
- 
- 2016      **Gerhards, M.**, Rock, G., Schlerf, M., Udelhoven, T. (2016): Water Stress Detection in Potato Plants using Leaf Temperature, Emissivity, and Reflectance. *International Journal of Applied Earth Observation and Geoinformation*, 53, 27–39.
- Rock, G., **Gerhards, M.**, Schlerf, M., Hecker, C., Udelhoven, T. (2016): Plant species discrimination using emissive thermal infrared imaging spectroscopy. *International Journal of Applied Earth Observation and Geoinformation*, 53, 16–26.
- 
- 2012      Schlerf, M., Rock, G., Lagueux, P., Ronellenfitsch, F., **Gerhards, M.**, Hoffmann, L., Udelhoven, T. (2012): A Hyperspectral Thermal Infrared Imaging Instrument for Natural Resources Applications. *Remote Sensing*, 4, 3995–4009.
-

